

SCANNING PROBE MICROSCOPY OF SEMICONDUCTOR QUANTUM DOTS

By

Richard Everson

**A thesis submitted in requirement for the degree of
M.Phil in Physics**

Cardiff University

January 2012

ABSTRACT

The purpose of this study was to design and construct a microscope combining scanning probe and optical microscopy techniques. The microscope is intended for the study of the fluorescence intermittency effect in quantum dots. This microscope has been realised, using quartz tuning forks as the force sensor. Two different techniques for preparing these tuning fork sensors for scanning probe microscopy have been developed, with a quality factor of roughly 10^4 . The microscope operates in high vacuum. Various components have been designed and constructed for this microscope, including positioning devices allowing for the positioning of scanning probe and optical microscopes on the same region of a sample. A time-correlated single photon counting technique has been employed for the optical microscopy part of the microscope.

ACKNOWLEDGMENTS

I would like to dedicate this work to my wife, Rebecca. Without her support this work would not have been possible. I would also like to thank my parents, my family, and Nigel and Karen for their continued support during this project.

I owe my deepest gratitude to my supervisors, Martin and Wolfgang. This would have been impossible without your support and guidance. I am also indebted to Rob Tucker, Dave, Scott, and the rest of the workshop staff at the Physics department of Cardiff University.

Finally I would like to thank my grandfather, Ron, who on more than one occasion made components for this project.

ABBREVIATIONS

| | |
|-------------|---|
| 1-D | 1 dimensional |
| 2-D | 2 dimensional |
| 2DEG | 2 dimensional electron gas |
| 3-D | 3 dimensional |
| ADC | analogue to digital converter |
| AFM | atomic force microscopy |
| AGC | automatic gain control |
| ADC | analogue to digital converter |
| BME | β -mercaptoethanol |
| CFD | contrast fraction discriminator |
| DAC | digital to analogue converter |
| DCET | diffusion controlled electron transfer |
| DOS | density of states |
| DSP | digital signal processor |
| EFM | electrostatic force microscopy |
| FFT | fast Fourier transform |
| FM | frequency modulation |
| FWHM | full width half maximum |
| GXSM | Gnome X scanning microscopy |
| HOPG | highly ordered pyrolytic graphite |
| KF | klein flange |
| LED | light emitting diode |
| MBE | molecular beam epitaxy |
| KPM | Kelvin probe microscopy |
| MFM | magnetic force microscopy |
| NC | noncontact |
| OM | optical microscopy |
| PLL | phase locked loop |
| PMT | photo multiplier tube |
| PFE | photoinduced fluorescence enhancement |
| PSD | phase sensitive detector |
| PC | phase comparator |
| QD | quantum dot |
| QTF | quartz tuning fork |
| RICM | reflection interference contrast microscopy |
| SEM | scanning electron microscopy |
| SFM | scanning force microscopy |
| S-K | Stranski-Krastinov |
| SPC | single photon counting |
| SPM | scanning probe microscopy |
| SR | Signal Ranger |
| STM | scanning tunnelling microscopy |
| TCSPC | time-correlated single photon counting |
| TIRFM | total internal reflection fluorescence microscopy |
| USB | universal serial bus |
| UHV | ultra high vacuum |
| VCO | voltage controlled oscillator |
| V-W | Volmer-Weber |

CONTENTS

| | |
|---|-----------|
| Abstract | 2 |
| Acknowledgements | 3 |
| Abbreviations | 4 |
| Contents | 5 |
| | |
| 1. Introduction | 7 |
| 2. Properties of quantum dots | 9 |
| 2.1. Introduction | 9 |
| 2.2. Quantised confinement | 10 |
| 2.2.1. 3D density of states | 10 |
| 2.2.2. 2D density of states | 12 |
| 2.2.3. 1D density of states | 13 |
| 2.2.4. 0D density of states | 13 |
| 2.3. Fabrication methods | 15 |
| 2.3.1. Epitaxy | 15 |
| 2.3.2. Colloidal synthesis | 17 |
| 2.4. Fluorescence intermittency | 18 |
| 2.4.1. Introduction | 18 |
| 2.4.2. Fluorescence intermittency in epitaxial quantum dots | 20 |
| 2.4.3. Fluorescence intermittency in single colloidal quantum dots | 21 |
| 2.4.4. Colloidal quantum dot arrays | 29 |
| 2.4.5. Suppression of intermittency in colloidal quantum dots | 31 |
| 2.5. Summary | 32 |
| 2.6. References | 34 |
| 3. An instrument combining scanning probe and optical microscopy | 39 |
| 3.1. Introduction | 39 |
| 3.2. Microscope cryostat | 45 |
| 3.3. Vibration Isolation | 47 |
| 3.4. Positioning devices | 50 |
| 3.4.1. Piezoelectric motors | 50 |
| 3.4.2. Inertial slider | 51 |

| | | |
|-------------|---|------------|
| 3.4.3. | Coarse positioning devices | 54 |
| 3.5. | Quartz tuning forks | 56 |
| 3.5.1. | Overview | 56 |
| 3.5.2. | Mechanical model | 57 |
| 3.5.3. | Electrically equivalent model | 60 |
| 3.5.4. | Tip production and arrangement | 62 |
| 3.6. | Atomic force microscopy control | 68 |
| 3.6.1. | Overview of the AFM system | 68 |
| 3.6.2. | The GXSM software and DSP | 68 |
| 3.6.3. | Tuning fork control circuit | 70 |
| 3.6.4. | The phase locked loop | 74 |
| 3.6.5. | Imaging | 79 |
| 3.6.6. | Aligning the optical/scanning probe parts of the microscope | 85 |
| 3.7. | Optical Microscopy | 86 |
| 3.8. | Conclusion | 89 |
| 3.9. | References | 91 |
| 4. | Planned Experiments | 96 |
| 4.1. | References | 100 |
| 5. | Conclusion | 101 |

1. Introduction

A semiconductor material whose dimensions are small enough to confine excitons in all three spatial dimensions is known as a quantum dot. These particles have an emission spectrum that is not only narrow (typically a peak with 50nm FWHM), but is also dependent on the size of the particle; it is tuneable.

Quantum dots can be prepared in such a way that they are less susceptible to photobleaching/damage than organic dyes. They can be functionalised with organic groups and can be solubilised. These properties have seen significant interest in these nano particles for biological imaging and labelling. It is hoped that quantum dots could also be a source for controlled single photons, a property that makes them promising candidates for quantum cryptography and quantum computing applications. There is a problem in utilising quantum dots for these technologies though; the fluorescence intermittency effect.

Fluorescence intermittency, or "blinking" renders the quantum dot in a dark, non-emitting state for durations that can be anywhere in length between microseconds and hours. Several models have been put forward in an attempt to explain this phenomenon, based on experiments utilising either optical microscopy techniques or scanning probe microscopy techniques. Current theories on the origin of the intermittency suggest that the optical properties of quantum dots are closely tied to their charge and that of their environment, but very few experiments have been performed that combine optical and scanning probe microscopy techniques on quantum dots; techniques that performed simultaneously could reveal how a dots charge and optical emission are related. The primary aim of this project has been to design and construct such a microscope. Currently atomic force microscopy is the principle mode of operation for the scanning probe microscope, though it is intended to adapt the system for electrostatic force microscopy also.

Alignment of two separate microscope systems on a single particle that is only a few nanometres in diameter is a considerable challenge; many of the microscope components have been homebuilt specifically for this purpose.

Chapter 2 of this thesis is a review of quantum dots, specifically the fluorescence intermittency effect, as observed in single quantum dots and quantum dot arrays, as well as methods for suppressing this property of dots. Chapter 2 discusses the design and operation of the combined optical and scanning probe microscope. Data obtained via this microscope is also contained in chapter 3.

2. PROPERTIES OF QUANTUM DOTS

2.1. Introduction

This chapter outlines the key optical and electronic properties of semiconductor quantum dots, focusing particularly on the intermittency effect; how it is manifested, models for its explanation and briefly some recent developments leading to its suppression.

If the size of a semiconductor crystal is reduced below its exciton Bohr radius (the average distance between electron and hole) then only a set of discrete electron states exist, similar to the case of individual atoms. This is the case for quantum dots. The broad absorption spectrum and narrow, tuneable emission spectrum are just some of the attractive characteristics that have stimulated interest in a range of fields from photovoltaic's to quantum computing.

Colloidal quantum dots can be coated in a protective capping layer that makes them far less susceptible to photobleaching than organic dyes. This coupled with the fact that these structures can be functionalised with organic groups and solubilised [1] has yielded encouraging results in biological labelling [2, 3].

For quantum computing and cryptography applications it is essential that a controlled source of single photons can be realised. To this extent quantum dots are a promising candidate [4-6].

The narrow emission spectrum of quantum dots (typically 50nm FWHM) can be tuned to any part of the visible spectrum just by altering their size. This, as well as temperature insensitivity has led to the development of laser devices with low lasing thresholds [7, 8] organic light emitting diodes [9] and quantum dot based solar cells [10].

The fluorescence intermittency effect of quantum dots, whereby the emission intensity switches on and off, or more generally between different levels with time is a limiting factor for their use in almost any application. Since its discovery by Nirmal *et al* [11] in 1996 a significant body of research has been dedicated to elucidating the mechanism behind the effect. Several complex models have since been put forward to explain intermittency, yet despite this it remains an effect that is still not fully understood.

2.2. Quantised confinement

2.2.1. 3D density of states

The density of states (DOS) $\rho(E)$ is the number of allowed states an electron can occupy per unit energy and volume [52]:

$$\rho(E) = \frac{dN}{dE} = \frac{dN}{dk} \frac{dk}{dE} \quad (\text{Eq.1})$$

for a bulk 3D crystal the number of available states dN in k-space is given by the volume of radius k, divided by the volume occupied by a single state and the volume in real space, a factor of 2 has been introduced to account for the spin degeneracy of electron states:

$$\begin{aligned} N_{3D} &= 2 \left(\frac{4}{3} \pi k^3 \right) \left(\frac{L}{2\pi} \right)^3 \left(\frac{1}{L^3} \right) \\ N_{3D} &= \frac{8\pi k^3}{3(2\pi)^3} \\ \frac{dN_{3D}}{dk} &= \frac{k^2}{\pi^2} \end{aligned} \quad (\text{Eq.2})$$

manipulation of the characteristic equation governing an electron in a vacuum yields an expression for k ; the effective mass is used to account for its motion in a crystal lattice:

$$k = \left(\frac{2m^*}{\hbar^2} \right)^{\frac{1}{2}} E^{\frac{1}{2}}$$

$$\frac{dk}{dE} = \frac{1}{2} \left(\frac{2m^*}{\hbar^2} \right)^{\frac{1}{2}} E^{-\frac{1}{2}} \quad (\text{Eq.3})$$

substitution of Eq.2+3 into Eq.1 gives the density of states in 3 dimensions:

$$\rho_{3D}(E) = \frac{1}{2\pi^2} \left(\frac{2m^*}{\hbar^2} \right)^{\frac{3}{2}} E^{\frac{1}{2}} \quad (\text{Eq.4})$$

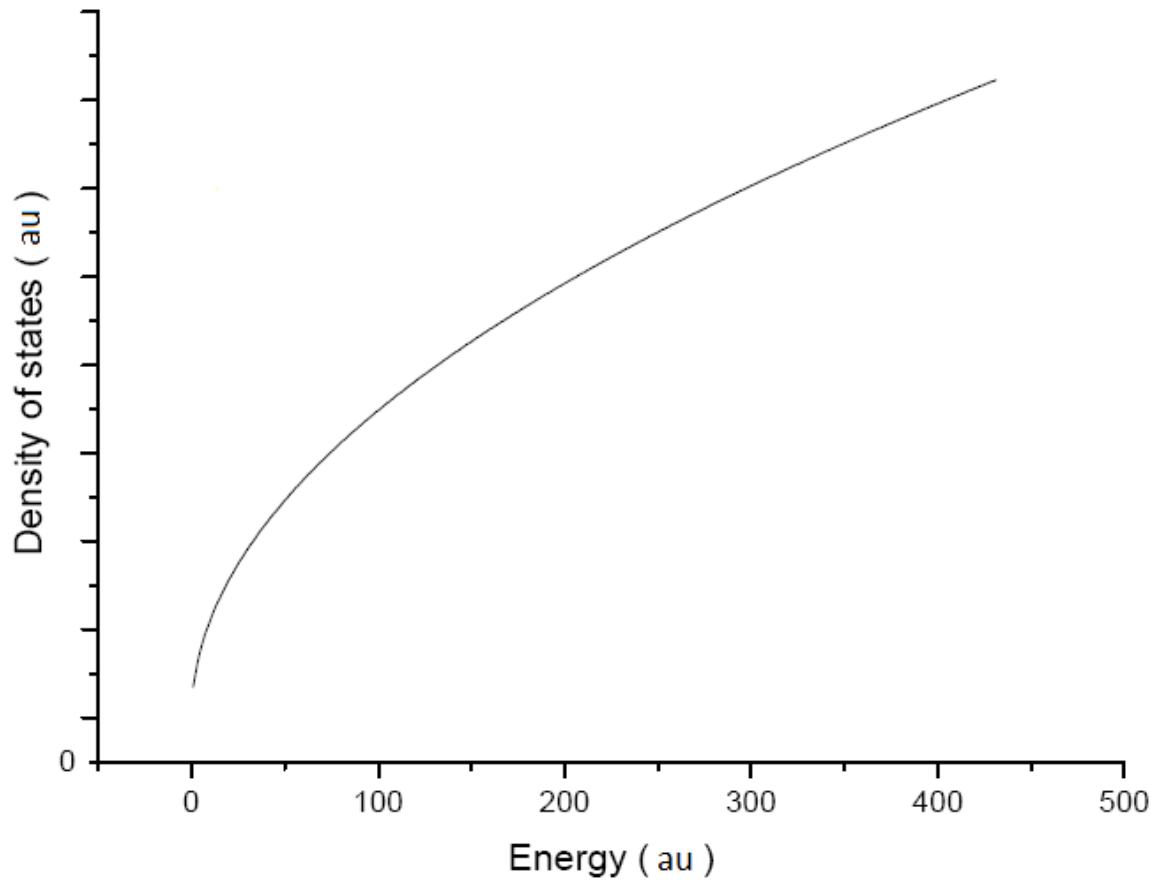


Figure 1. Typical density of states for a bulk semiconductor.

2.2.2. 2D density of states

If one dimension of the bulk 3D crystal is made to be smaller than the exciton Bohr radius of the material then electrons are confined in this dimension. With only 2 degrees of freedom electrons occupy a circle in k-space with radius k . This type of confinement is commonly referred to as a quantum well or 2 dimensional electron gas (2DEG). The electron density in a 2DEG is still given by Eq.10, but the number of states N_{2D} now considers the area of k-space in 2D as opposed to a volume:

$$\begin{aligned} N_{2D} &= 2 \left(4\pi k^2 \right) \left(\frac{L}{2\pi} \right)^2 \left(\frac{1}{L^2} \right) \\ N_{2D} &= \frac{2\pi k^2}{(2\pi)^2} \\ \frac{dN_{2D}}{dk} &= \frac{k}{\pi} \end{aligned} \tag{Eq.5}$$

dk/dE is still given by Eq.12, giving a 2 dimensional density of states of:

$$\rho_{2D}(E) = \frac{m^*}{\pi \hbar^2} \tag{Eq.6}$$

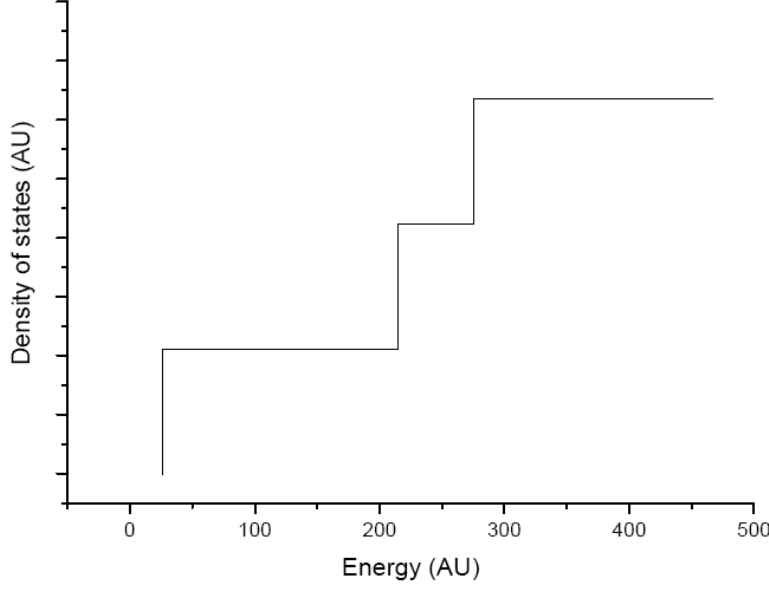


Figure 2. Typical DOS for a 2DEG.

2.2.3. 1D density of states

If another dimension is removed then electrons are restricted to a 1 dimensional quantum wire. In a similar manner to the 2D density of states we further restrict the number of states N , this time to a line in k -space of length $2k$:

$$\begin{aligned}
 N_{1D} &= 2(2k) \left(\frac{L}{2\pi} \right) \left(\frac{1}{L} \right) \\
 N_{1D} &= \frac{2k}{\pi} \\
 \frac{dN_{1D}}{dk} &= \frac{2}{\pi}
 \end{aligned} \tag{Eq.7}$$

when this result is combined with Eq.1 we obtain the density of states for a quantum wire:

$$\rho_{1D}(E) = \frac{1}{\pi E^{\frac{1}{2}}} \left(\frac{2m^*}{\hbar^2} \right)^{\frac{1}{2}} \tag{Eq.8}$$

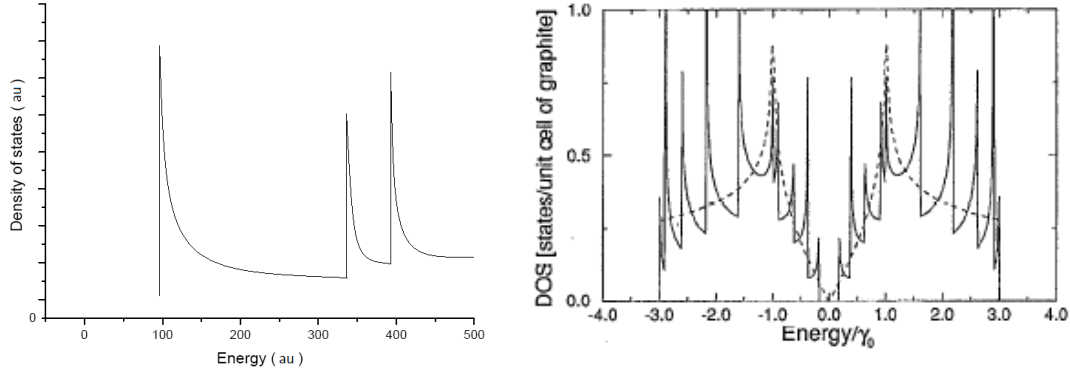


Figure 3. [12]. Left – typical DOS for a 1D nanowire. Right – DOS for a carbon nanotube.

2.2.4. 0D density of states

When electrons in a semiconductor are confined in all three spatial dimensions only degenerate electron states exist, materials fulfilling this condition are known as quantum dots or nanocrystals. Consider a box of dimensions L_x , L_y , and L_z , where an infinite potential separates the inside of the box from the outside, the 3-dimensional Schrodinger equation within the box is given by:

$$-\frac{\hbar^2}{2m^*} \left(\frac{\partial^2}{\partial x^2} + \frac{\partial^2}{\partial y^2} + \frac{\partial^2}{\partial z^2} \right) \psi(x, y, z) = E_{x,y,z} \psi(x, y, z) \quad (\text{Eq.9})$$

this equation can be decoupled into 3 one-dimensional equations E_x , E_y , and E_z that contribute to the total energy $E_{x,y,z}$:

$$\begin{aligned} -\frac{\hbar^2}{2m^*} \frac{\partial^2}{\partial x^2} \psi(x) &= E_x \psi(x) \\ -\frac{\hbar^2}{2m^*} \frac{\partial^2}{\partial y^2} \psi(y) &= E_y \psi(y) \\ -\frac{\hbar^2}{2m^*} \frac{\partial^2}{\partial z^2} \psi(z) &= E_z \psi(z) \end{aligned} \quad (\text{Eq.10})$$

solutions to Schrodingers equation are of the form:

$$\begin{aligned}\psi(x) &= A \sin(kx) + B \cos(kx) \\ k &= \frac{\pi n}{L_\omega}\end{aligned}\tag{Eq.11}$$

where y or z could also be used in place of x . If the origin of the three dimensional box is set at one corner, only sinusoidal solutions exist and Eq.3 is simplified:

$$\psi(\omega) = A \sin\left(\frac{\pi n \omega}{L_\omega}\right)\tag{Eq.12}$$

the constant A can then be obtained by normalisation of Eq.4:

$$\int_0^{L_\omega} \psi^*(z) \psi(z) dz = 1\tag{Eq.13}$$

giving $A = \sqrt{2/L_\omega}$, and:

$$\psi(\omega) = \sqrt{\frac{2}{L_\omega}} \sin\left(\frac{\pi n \omega}{L_\omega}\right)\tag{Eq.14}$$

eq.6 can then be used to solve Eq.2 and find the energy components in each dimension:

$$E_{x,y,z} = \frac{\hbar^2 \pi^2 n_{x,y,z}^2}{2m * L_{x,y,z}^2}\tag{Eq.15}$$

$$E_{x,y,z} = \frac{\hbar^2 \pi^2}{2m *} \left(\frac{n_x^2}{L_x^2} + \frac{n_y^2}{L_y^2} + \frac{n_z^2}{L_z^2} \right)\tag{Eq.16}$$

each state in the 0D box is defined by the three quantum numbers n_x , n_y and n_z . Consequently the DOS for a 0D crystal is simply a set of delta functions at energies governed by these quantum numbers and the dimensions of the box; $L_{x,y,z}$. As the energy is inversely proportional to the dimensions of the dot the emission spectrum

can be tuned simply by altering the size of the dot. For a spherical quantum dot a similar approach can be taken, but using spherical polar coordinates [52].

2.3. Fabrication methods

2.3.1. Epitaxy

Molecular beam epitaxy (MBE) or metal organic chemical vapour deposition provides three different growth modes for epitaxial quantum dot formation, depending mainly on the strain of the epitaxy. These are the Frank-Van der Merwe (F-VdM), Volmer-Weber (V-W) and Stranski-Krastinov (S-K) methods, as shown in figure 4.

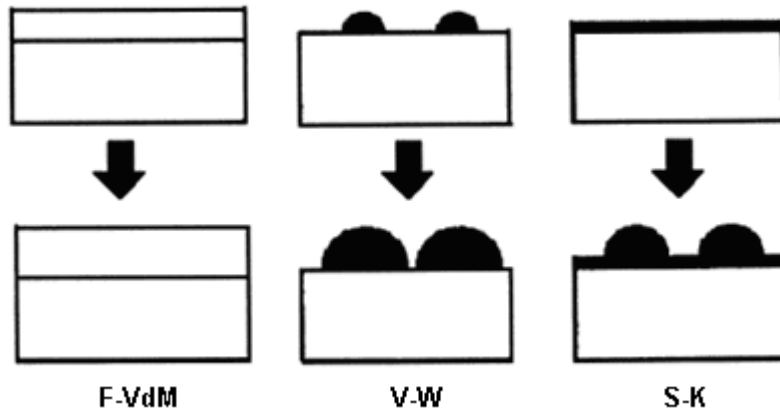


Figure 4. [13]. Schematic diagram of the Frank-Van der Merwe, Volmer-Weber and Stranski-Krastinov growth modes.

The F-VdM mode corresponds to a 2D layer by layer growth, the V-W mode represents 3D or island growth [14]. Another regime is the S-K mode; this growth mode is a strain induced process for self assembly of quantum dots. Material is first deposited in a 2D monolayer that is lattice mismatched with the substrate. As the wetting layer thickness increases so too does the strain induced elastic energy. At a critical thickness there is 3D growth which allows an elastic relaxation driven by the reduction in strain energy. The transition from 2D-3D growth is a first order phase transition [15], and is discussed in [16, 17].

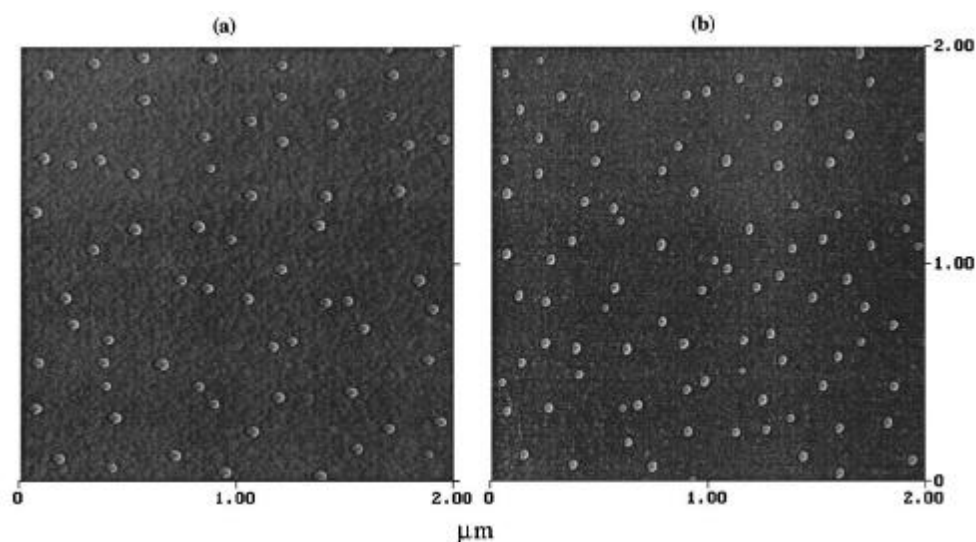


Figure 5. [18]. AFM images of CdSe dots grown by MBE on a) ZnSe, b) ZnMnSe.

2.3.2. Colloidal Synthesis



Figure 6. [19]. Photoluminescence of colloidal quantum dots under UV illumination. The emission spectrum is dependent on the QD size.

Colloidal quantum dots can be produced by synthetic techniques [20] where the size, shape, composition and internal structure of the nanocrystal can be controlled. The reagents are added at defined times to a hot coordinating solvent, in which they decompose and nucleation sites are formed. On formation of nucleation sites the concentration of reactants drops below a critical level so that no new nucleation sites are formed, but addition to existing nucleation sites still occurs.

A variation of this technique is to add the reagents at a cooler temperature and to control the concentration of nucleation sites by increasing the temperature for a short period of time. When the desired concentration of nucleation sites is reached the temperature is reduced so that only addition to existing nucleation sites occurs.

Depending on their environment and composition, quantum dots produced by colloidal synthesis can be chemically unstable. A capping layer of a higher band gap material is typically used to increase this stability; a ZnS shell is commonly used as a capping layer for CdSe cores. The core/shell can also be functionalised to alter properties such as susceptibility to photobleaching and solubility [1].

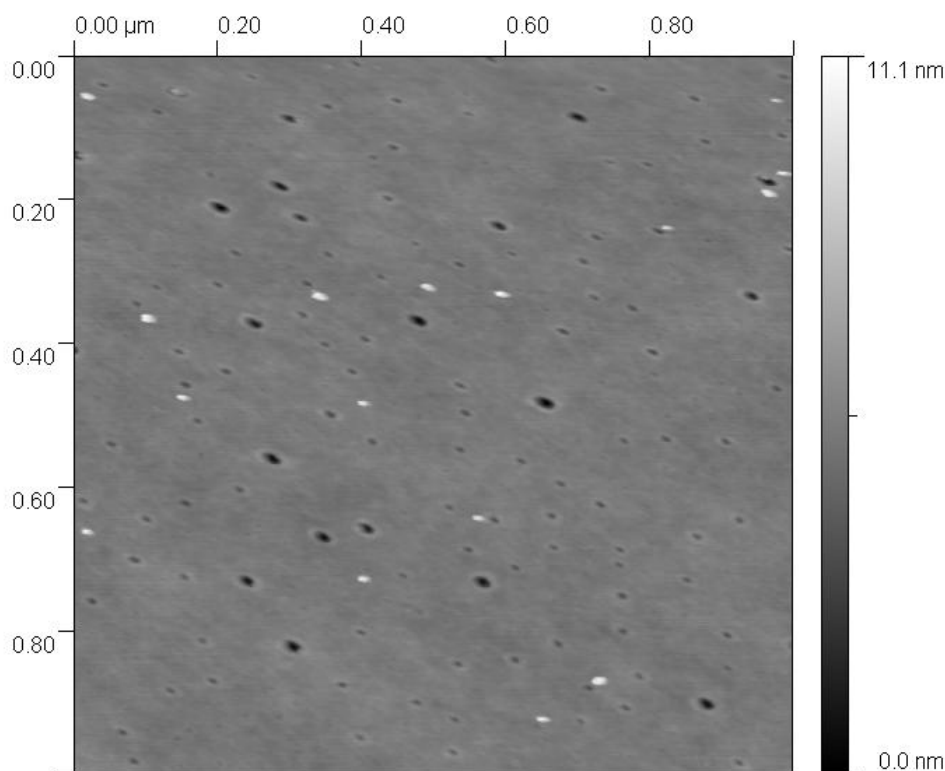


Figure 7. AFM tapping mode image of CdSe/ZnS QDs in toluene spun cast onto a glass coverslip.

2.4. Fluorescence intermittency

2.4.1. Introduction

A limitation of quantum dots is the fluorescence intermittency effect, commonly referred to as blinking. The effect is manifested as a switching of the emission intensity between two or more levels, a bright/on state where stable emission is observed and a dark/off state where there is weak optical emission. This effect is by no means limited to quantum dots alone; single ions, organic molecules, fluorescent proteins, dye molecules and single light harvesting complexes have all been shown to exhibit fluorescence intermittency, albeit as a result of different mechanisms.

One such mechanism predicting fluorescence intermittency was proposed by Bohr in 1913, though it wasn't until the 1980's that experimental observation was realized by Nagourney *et al* [21]. The barium ion has two excited states coupled to the same ground state. There is a large difference in transition rate between the ground state and the two excited states, shown in figure 8a. Both excited states can decay to a triplet state, from which decay back to the ground state is by spontaneous emission. Nagourney *et al* isolated a single, laser cooled Ba⁺ ion in a radio frequency trap in ultra high vacuum (UHV). They use a 493.4nm laser to drive the transition between the ground state and the excited state ($6^2P_{1/2}$) whilst monitoring the emission of the ion. A second 649.9nm laser is used to prevent trapping of the electron in the $5^2D_{3/2}$ triplet state. A filtered cathode lamp is used to drive the transition from the ground state to the $6^2P_{3/2}$, from this state an electron can decay to the $5^2D_{5/2}$ triplet state, the radiative lifetime of which is ~30 seconds. With the electron trapped in this state the emission of the ion is suppressed. Figure 8b shows the blinking behavior of the Ba⁺ ion, the probability distribution of on times was shown to exponentially decrease with increasing on time.

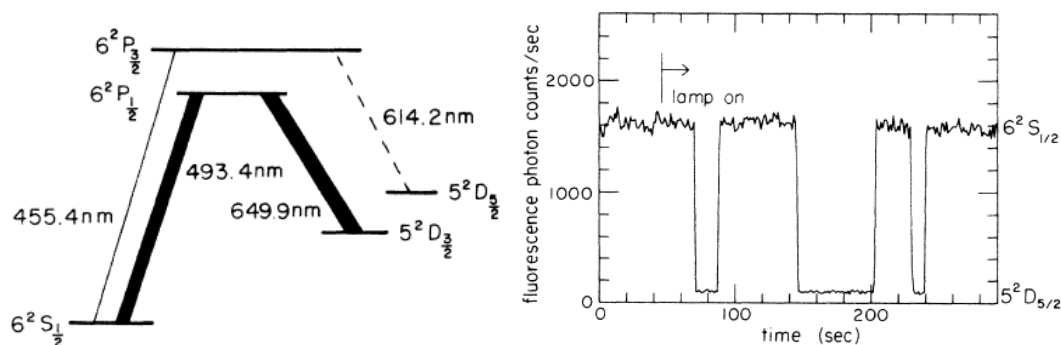


Figure 8. [21] A) energy level diagram of the Ba⁺ ion. Bold lines show laser driven transitions, the narrow line is the lamp driven transition, and the dotted line is the transition to the trap state. B) Emission intensity with time for a Ba⁺ ion. The time at which the cathode lamp was turned on is indicated.

Whilst the emission intensity of Ba⁺ ions fluctuates simply between dark and light states, some systems have been shown to exhibit a more complicated blinking behaviour. The emission intensity of individual light-harvesting complexes has been shown to fluctuate between numerous levels, even more so with increased excitation intensities, if the excitation intensity is increased further the molecules inevitably became photobleached and no further emission was observed. Oxidation of these molecules [22, 23] or vibronic relaxation processes [24] have both been considered in an effort to explain these fluctuations.

2.4.2. Fluorescence intermittency in epitaxial quantum dots

The blinking behaviour is different even between quantum dots produced by different processes. Pistol *et al* [25] observed intermittency in self assembled InP QDs grown by the Stranksi-Krastinov mode, typically at a temperature of ~7K. Only a very small fraction (about one in a thousand) of the dots exhibited blinking behaviour and the blinking was shown to become increasingly frequent with increasing excitation intensity, supporting a light induced process. Most of the blinking dots switched between only two emission intensities. Because the probability density of on and off times were both exponential, the emission intensity of epitaxial dots was shown to be a random telegraph signal. Only a very small percentage of the blinking dots switched between more than two levels.

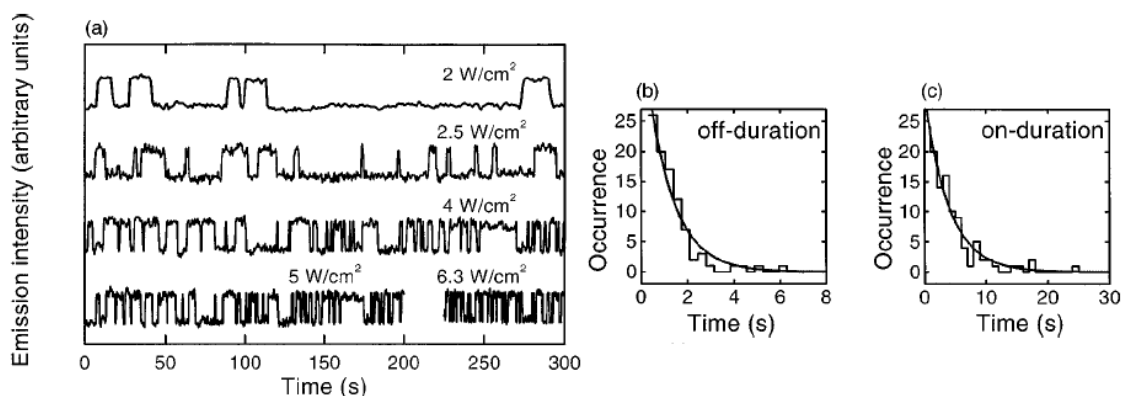


Figure 9. [25] (a) Emission intensity with time for epitaxial quantum dots showing blinking behaviour. A decrease in both on and off lifetimes is observed at higher excitation intensities. (b+c) Probability distribution histograms of both the off and on lifetimes with exponential fitting curves.

An interesting observation, and one that is in stark contrast to the case of single organic molecules, is that with further increase in excitation intensity ($>50\text{Wcm}^{-2}$) blinking was suppressed irreversibly and the dots emitted continuously even after the excitation intensity was reduced. This is further evidence for the broad range of mechanisms governing the intermittency effect in nanoscale systems. Increasing the temperature of the dots stimulated a similar increase in the frequency of switching with dots becoming unstable at temperatures greater than $\sim 50\text{K}$.

Because only a very small percentage of epitaxial dots exhibited blinking behaviour, Pistol et al could not attribute the switching to an intrinsic effect of the dots. Instead they suggest photoactivated nonradiative defects as the cause for intermittency in epitaxial dots. The defects would be mobile, giving rise to the blinking suppression after high intensity excitation. Defects of this nature have been observed in quantum wells [26], leading to photodegradation.

2.4.3. Fluorescence intermittency in single colloidal quantum dots

Nirmal *et al* [11] were the first to observe blinking in colloidal quantum dots. Their study focussed on CdSe quantum dots embedded in a thin polyvinyl butyral film, with and without a capping layer of ZnS. The emission intensity with time of a typical uncapped CdSe dot is shown in figure 10.

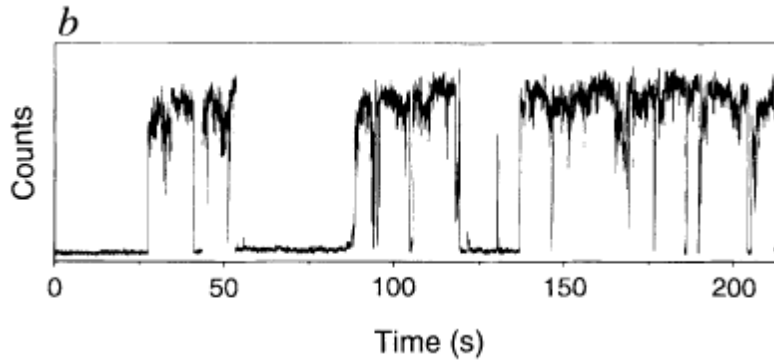


Figure 10. [11] Fluorescence intensity versus time trace of a single $\sim 21\text{-}\text{\AA}$ -radius CdSe nanocrystal. Excitation intensity $\sim 0.52\text{kWcm}^{-2}$.

To determine whether the phenomenon was a light induced effect, or a spontaneous effect, the excitation intensity was varied and observations made on the on/off period lifetimes. If the effect was due to spontaneous transitions between emitting and non-emitting states, the intermittency would be independent of the excitation intensity. Their results revealed that the on times were significantly reduced at higher excitation intensities whilst the off times were unaffected. This suggested that the dark state was due to a spontaneous, radiationless transition and that the excitation rate to this state was intensity dependent. As a means to explain the effect they proposed an Auger ionisation process; a low probability event where two excitons are produced and the energy released from recombination of one electron/hole pair is absorbed by the second electron/hole ejecting it from the core of the dot to the surrounding matrix. Whilst ionised, subsequent excitons recombine by Auger quenching - a faster non-radiative recombination [8]. An ionised QD is therefore in the dark state. QDs with a 7 monolayer ZnS capping layer displayed longer on times than uncapped dots. The energy gap of the capping layer is 2eV larger than the CdSe core, acting as a barrier to ionization and passivating many of the dots surface trap states.

Krauss *et al* [27] used electrostatic force microscopy to image the photoionization of CdSe quantum dots, supporting further the notion that the blinking mechanism was a result of charge transfer. 5nm QDs were spun-cast onto 1nm insulator layers on various metallic substrates. A small percentage of QDs were ionised before laser excitation, suggesting a thermal contribution to charging. A positive charge due to ionisation of up to 2 electrons was observed under laser excitation at wavelengths above the CdSe bandgap. Excitation at wavelengths less than the QD bandgap did not

cause ionisation, implying that photoexcitation in the QD rather than the metallic substrate causes the observed charging.

Efros *et al* [28] and later Banin *et al* [29], suggested a thermal contribution to the ionisation and recombination processes. They showed that if ejected to the surrounding matrix by either direct ionisation (higher energy excitation) or thermal/Auger processes (lower energy excitation); the time taken for the electron/hole to recombine with the QD is given by:

$$\tau = \tau_{ph}^m \exp\left(\frac{\Delta E}{kT}\right) \quad (\text{Eq.17})$$

where τ_{ph}^m is the typical phonon scattering time in the matrix, ΔE is the depth of the trap state in the surrounding matrix, and T is the temperature. The rate of ionization by Auger (Eq.10) and thermal processes (Eq.11) are given by:

$$\frac{1}{\tau_i} = \left(\frac{W_1 W_2 \tau_1}{1 + (W_1 \tau_1)} \right) \left(\frac{\tau_2}{\tau_2 + \tau_a} \right) \quad (\text{Eq.18})$$

$$\frac{1}{\tau_i} = \left(\frac{W_1 \tau_1}{1 + (W_1 \tau_1)} \right) \left(-\frac{T}{\tau_T} \right) \quad (\text{Eq.19})$$

where $W_{1,2} = \sigma_{1,2} I / \hbar \omega$, where $\sigma_{1,2}$ are the 1 and 2 electron-hole pair exciton cross sections, respectively, for a QD for light of frequency ω , and intensity I. $\tau_{1,2}$ are the radiative lifetimes of QDs with one and two electron hole pairs, and $1/\tau_a$ is the rate of auger ionisation of a QD with two electron/hole pairs. The probability densities of the on and off times (T) are found to be exponential:

$$W_{off} = \left(\frac{1}{\tau} \right) \exp\left(-\frac{T}{\tau}\right), \quad W_{on} = \left(\frac{1}{\tau_i} \right) \exp\left(-\frac{T}{\tau_i}\right) \quad (\text{Eq.20})$$

in their original observations of fluorescence intermittency Nirmal *et al* had shown the on/off times to be strongly non-exponential. The mechanism behind the blinking effect was therefore quite different to the Auger ionisation mechanism, specifically for the off times.

Kuno *et al* [30] observed fluorescence intermittency in CdTe QDs, showing that the blinking behaviour wasn't restricted to only CdSe dots. Their more important contribution to the study of intermittency was to show that the off period lifetimes could be characterized by a simple power law expression:

$$P(\tau_{off}) \propto \frac{1}{\tau_{off}^{(1+\alpha)}} \quad (\text{Eq. 21})$$

where $P(\tau_{off})$ is the probability density of off times of length τ_{off} (in seconds) per second. α is a constant with a value shown to be ~ 0.5 , this value has also been observed in numerous more recent studies. The power law was shown to follow experimental data over 5 decades in time for many QDs (Fig. 2).

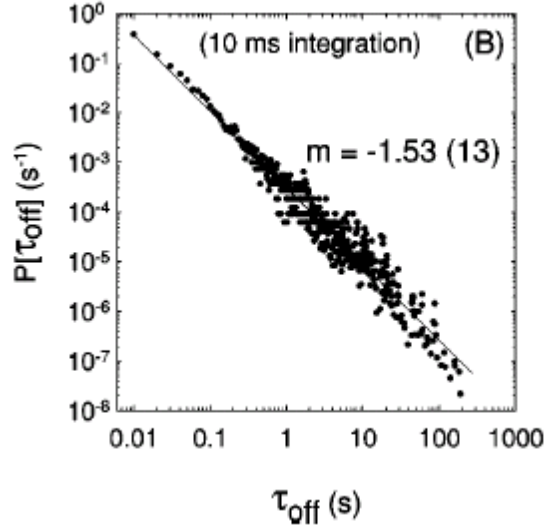


Figure 11. Normalized probability density for off times for 29Å CdSe QDs with a 5 monolayer ZnS capping layer, excited at 2.4kWcm⁻².

To explain the inverse power law statistics Kuno *et al* proposed a distribution of trap states, rather than the three level systems suggested previously. The group were

unable to experimentally determine the method by which electron transfer occurs between trap states but suggested one of two processes. An Arrhenius model (Eq. 14) where the recovery rate (k) depends on the energy depth of the trap state (ϵ_{trap}) below (above) the conduction (valence) band:

$$k = A \exp\left(\frac{\epsilon_{\text{trap}}}{kT}\right) \quad (\text{Eq. 22})$$

or a tunnelling model (Eq. 15), where the recovery rate is dependent upon the separation distance between initial and final states (r) and the degree of localisation of the carrier (R_0):

$$k = A \exp\left(\frac{r}{R_0}\right) \quad (\text{Eq. 23})$$

in both cases A is a pre-factor corresponding to the frequency of escape attempts (by the electron from the trap). It is important to notice that both models predict an exponential rate of detrapping for transitions from 1 state to another.

In a subsequent paper [31] the group also observed the same power law behaviour in the on time probability density. The before-mentioned Arrhenius and hopping recombination models both treat the distribution of traps as a set of static states, thus predicting an exponential distribution of “on” times, and are therefore inconsistent with observations. They produced a new model where the trap state is separated from the QD core by a potential barrier of fluctuating height and width, caused by conductivity changes (due to capping ligands) and availability of trap sites respectively. The transmission probability of an electron with energy E and mass m , across a square potential barrier of length L and height V_0 is given by [32]:

$$T \approx 16 \frac{E}{V_0} \left(1 - \frac{E}{V_0}\right) e^{-2kL} \quad (\text{Eq. 24})$$

where the attenuation constant k is given by:

$$k = \frac{\sqrt{2m(E - V_0)}}{\hbar} \quad (\text{Eq. 25})$$

Altering the values of either the barrier height (V_0) or width (L) by as much as only 25% can cause as much as a 10^7 -fold change in the transmission probability, easily encompassing the range of blinking times experimentally observed.

Neuhauser *et al* have shown at low temperature that after a long off period the subsequent luminescence displays spectral shifting [33]. A redistribution of charge when an electron combines with an ionised QD is suggested as the cause of the spectral shift and intensity change. This supports the idea that QDs emission behaviour is strongly dependent on changes in its immediate electronic environment, as proposed by Kuno *et al*. The broad range of spectral shifts (of up to 14nm) are further evidence against a simple 3 or 4 level system. Following this research Schlegal *et al* showed that the fluorescence decay time of colloidal dots is non-uniform and strongly dependent on the fluorescence intensity fluctuations [34]. Van Sark *et al* observed a blue shift of up to 40nm prior to photo bleaching due to oxidation and therefore shrinking of the QD core [35].

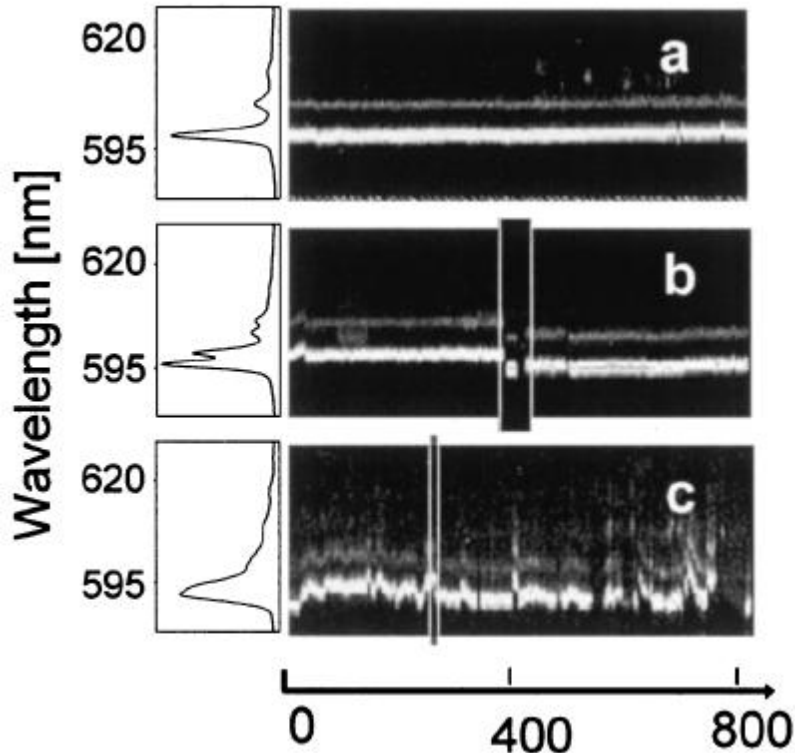


Figure 12. [33]. Low temperature emission frequencies of three CdSe/ZnS quantum dots displaying spectral shifting after switching back to the on state.

Studying fluorescence intermittency with a wide range of variables, Shimizu *et al* [36] proposed a theoretical framework that for the first time led naturally to a power law distribution with exponent ~ 1.5 . They found that the off time statistics are independent of temperature, excitation intensity, surface morphology and size, consistent with previous studies. However, the on time behaviour was affected by these parameters, manifested as a truncation of the power law behaviour (Fig. 13.) indicating a secondary blinking mechanism that becomes dominant at the truncation point. Since the on statistics are shown to be both temperature and excitation intensity independent the process coupling a dark state to a bright state is a tunnelling mechanism as opposed to a photo-assisted process.

Based on these results and the observation of spectral shifting by Neuhauser, Shimizu *et al* proposed a random-walk first-passage-time model. In its simplest form the off state arises due to tunnelling of an electron to a trap state in the vicinity of the QD core. The energy of both the trap state and the excited state of the dot move on a random walk where transitions between the states can only occur when they are in resonance. If a dot experiences a long off time it can be assumed that the two states are far from resonance and crossover back to the emitting state is unlikely. Rapid blinking of a QD is observed when the excited and trap states are close to resonance. Knappenberger et al [17] also observed a truncation of the “on” times with increased excitation power, and have recently proposed models to explain the observation.)

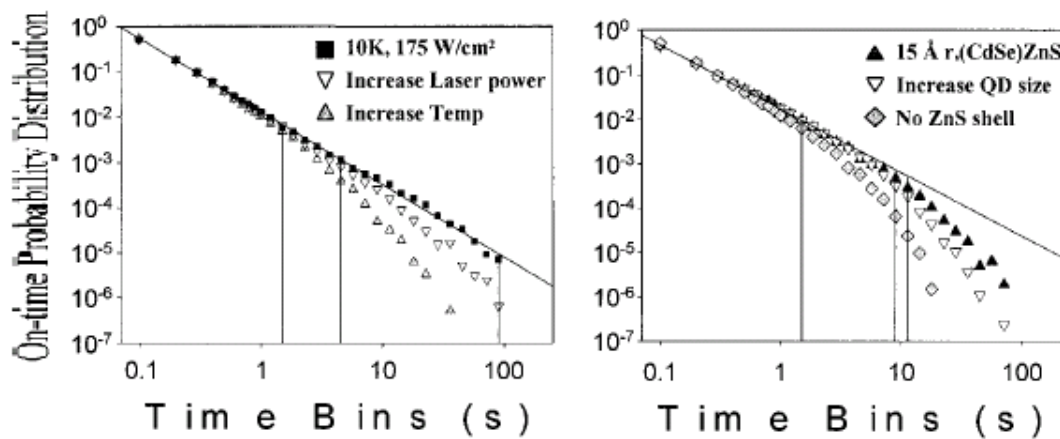


Figure 13. (a) Average on-time distribution for 25Å CdSe (ZnS) QDs at 300K + 175Wcm⁻² (▼), 10K + 700Wcm⁻² (Δ), and 10K + 175Wcm⁻² (■). (b) Average on-time distribution for 15Å CdSe (ZnS) QDs (▲), 25Å CdSe (ZnS) QDs (Δ), and 25Å CdSe QDs (◇). All 3 results in (b) are at room temp. with 100Wcm⁻² excitation power.

The most detailed study of QDs by EFM has been performed by Cherniavskaya *et al* [37-39]. They observed charging effects of QDs on both n-doped and p-doped silicon with different oxide layer thickness' and consider both s and p orbital transitions. They observe a positive charging effect on the quantum dots whilst under illumination and attribute this to electrons tunnelling from the dot to the silicon through the oxide layer. Due to band bending there is an accumulation of electrons (holes) at the silicon/oxide interface for p-type (n-type) silicon. As a result dots on P-type silicon were shown to exhibit less charging and to have quicker recombination times than on the n-type substrate. They found that the effects of oxide thickness were negligible. Though they suggest that several of their results exhibit behaviour expected from fluorescence intermittency; with no means to measure the optical output there is no way of confirming these findings. The group have also performed similar experiments on 12nm PbSe dots [40]. These nanocrystals have a Bohr exciton radius of 46nm – much larger than typical II-VI or III-V QDs. Consequently quantum confinement is observed in much larger dots of this composition.

Tang *et al* [41, 42] have constructed a diffusion controlled electron transfer (DCET) model based on the principles of Shimizu et al, who suggested that the trap state energy undergoes a random-walk, with charge transferred between the QD states and the trap only when their energy levels are aligned. This is shown in figure 14. The DCET model naturally leads to intermittency governed by power law statistics with the observed exponent of 1.5, and offers an explanation to the observed truncation at longer “on” periods and its temperature dependence. In the “on” state, excitation and recombination between states $|G\rangle$ and $|L^*\rangle$ causes emission of photons of wavelength γ_f . The trap state $|D\rangle$ wanders in energy as a result of phonon interactions, and electron crossover between the $|L^*\rangle$ and $|D\rangle$ states can occur when their energy levels are aligned (in resonance). When the electron is excited from the dark state $|D\rangle$ to the dark excited state $|D^*\rangle$ recombinations are by a radiationless Auger process. The QD remains in the dark state until the energy of the $|L^*\rangle$ and $|D\rangle$ states re-align and

electron crossover back to the excited light state occurs. This model predicts power law statistics with two exponents, 0.5 for blinking times much less than $t_{c,k}=0.1\text{ms}$, and the commonly observed 1.5 value for blinking times greater than $t_{c,k}=0.1\text{ms}$. The distribution of the blinking statistics P is given by:

$$P_k(T) \approx \frac{1}{\sqrt{\pi t_{c,k}}} t^{-\frac{1}{2}} \quad \text{If } t \ll t_{c,k} \quad (\text{Eq. 26})$$

$$P_k(T) \approx \frac{\sqrt{t_{c,k}}}{2\sqrt{\pi}} t^{-\frac{3}{2}} \quad \text{If } t \gg t_{c,k} \quad (\text{Eq. 27})$$

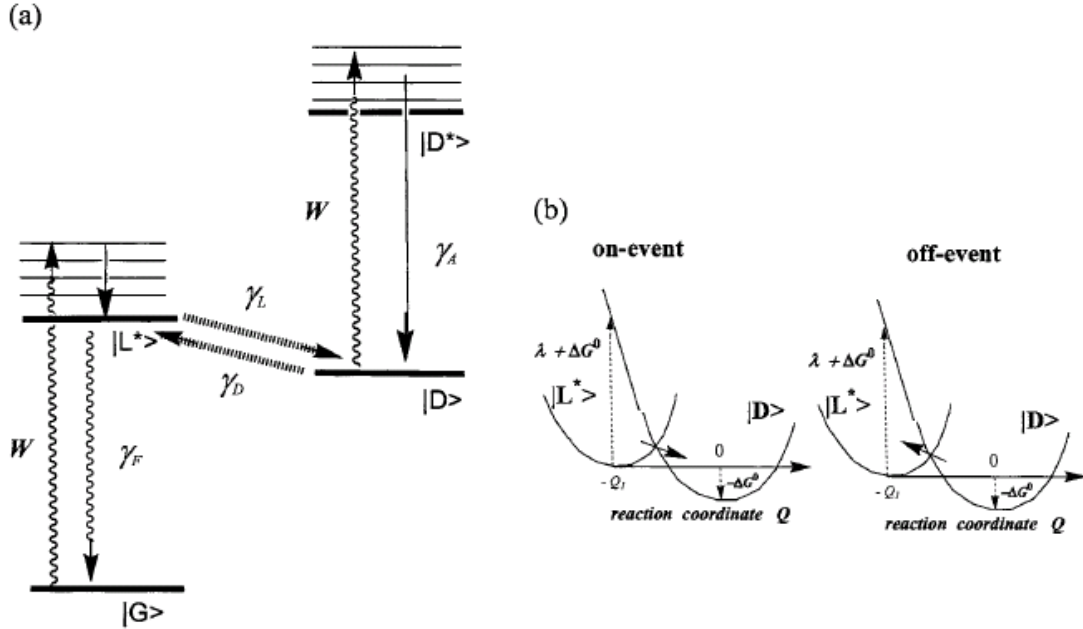


Figure 14. [41, 42]. (a) Schematic diagram of the energy levels in the DCET model, $|G\rangle$ and $|L^*\rangle$ are the ground and excited light state respectively. $|D\rangle$ and $|D^*\rangle$ are the charge separated state and excited charge separated state. (b) DCET shown on parabolic potential surfaces, the system enters a dark state on cross-over from the $|L^*\rangle$ to the $|D\rangle$ state.

More recent experiments extended to shorter timescales have shown the crossover of the power law exponent at time scales shorter than $5\text{-}35\mu\text{s}$ [43]. Pelton *et al* suggest that the size and composition of the QD and its environment may contribute to the critical time, $t_{c,k}$ at which the crossover occurs. These measurements agree with the DCET model, although the exponent of the power law was found to differ from those proposed by Tang *et al*.

2.4.4. Colloidal quantum dot arrays

Krauss *et al* [27] also studied arrays of quantum dots on HOPG by EFM. Individual QDs are extremely mobile on HOPG but in higher concentrations QDs form rafts, typically 100nm in size. The TOPO coating of the QDs forms an insulating barrier between the CdSe core and the HOPG of roughly 0.7nm thickness. Upon excitation a steady increase in frequency shift of the EFM probe was measured which reached saturation after ~300 seconds. Interestingly they found that the charge signal did not remain constant between consecutive scans, instead the charge of different regions increased and decreased in magnitude with a rate similar to measurements of individual dots. The observed behaviour is thought to be due to charge transfer between the QDs and the HOPG.

Quantum dot arrays are formed when the dot separation is small enough that there is coupling between the particles. Photoinduced fluorescence enhancement (PFE) has been observed in optical experiments on QD arrays by several groups [44-47]. This is an effect characterised by a steady increase in emission intensity when a QD array is optically excited. Maenosono *et al* offer two explanations for PFE. The first is the physisorption of water molecules by the QDs that passivate surface trap states. The second possibility is a decrease in “off” times rather than an increase in emission intensity from individual dots. Photoelectrification is suggested as the cause of this effect, whereby ionisation of a minority of QDs fills available trap states throughout the matrix, rendering the majority of dots in the neutral/on state.

Kimura *et al* extend these measurements and observe the effect of QD film thickness on PFE. They find that the emission intensity increases more rapidly with increasing film thickness until ~3.2 monolayers of dots are present, after this thickness the rate of PFE decreases, as shown in figure 15b. When the QD coverage is very low a negative intensity change is observed, an effect also observed by Tang *et al* [41] in QD ensembles where the QD spacing is large enough that there is no coupling between dots. With these lower densities the emission intensity decays as a stretched exponential with time, as a result of either photobleaching of dots or an increasing amount of dots falling into very long off periods.

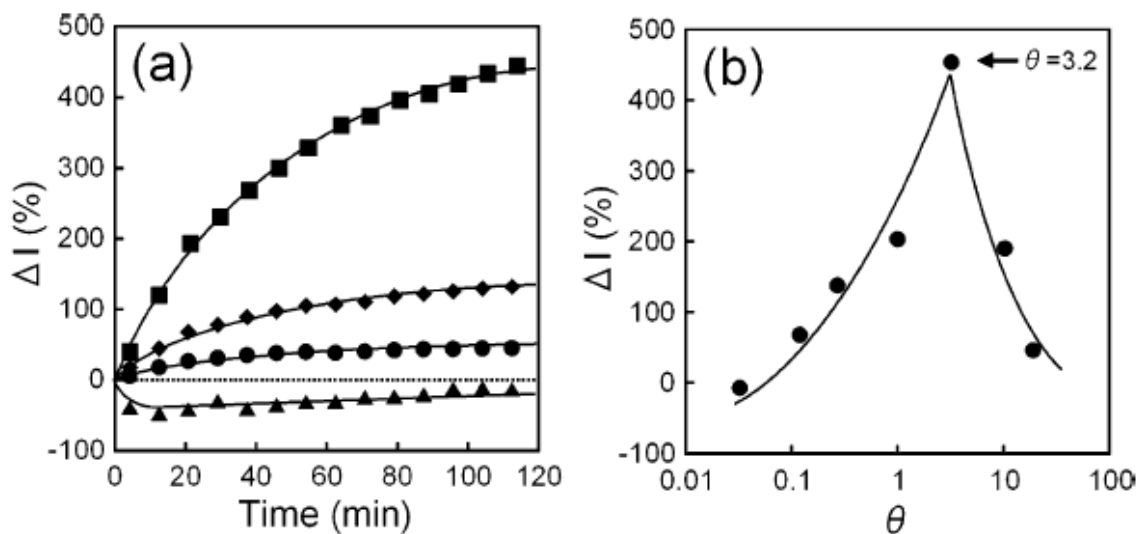


Figure 15. (a) time variation of the change in emission intensity (ΔI) with time for four different QD film thicknesses θ , the triangles, diamonds, squares and circles correspond to θ values of 0.032, 0.27, 3.2 and 19 respectively. (b) Change in emission intensity after 120 minutes of illumination for various film thicknesses.

2.4.5. Suppression of intermittency in colloidal quantum dots

In recent years considerable effort has been made to reduce the intermittency of colloidal quantum dots. Spinicelli *et al* offer an excellent review of the methods used to obtain non-blinking dots [48].

Hohng *et al* were able to achieve almost 100% reduction in blinking by passivation of the dots with thiol moieties [49]. In their experiments QDs showed severe blinking whilst in a buffer solution that was almost entirely quenched when β -mercaptoethanol was added. No permanent changes to the quantum dots are believed to occur, since the blinking behaviour reappeared immediately after removal of the BME solution. Jeong *et al* [50] extended the study to test the effect of BME concentration on quantum yield of QDs. Favourable results were only found for lower concentrations and at higher concentration the quantum yield was lower than ambient levels. Thiol exposure time and pH level also affected the blinking behaviour.

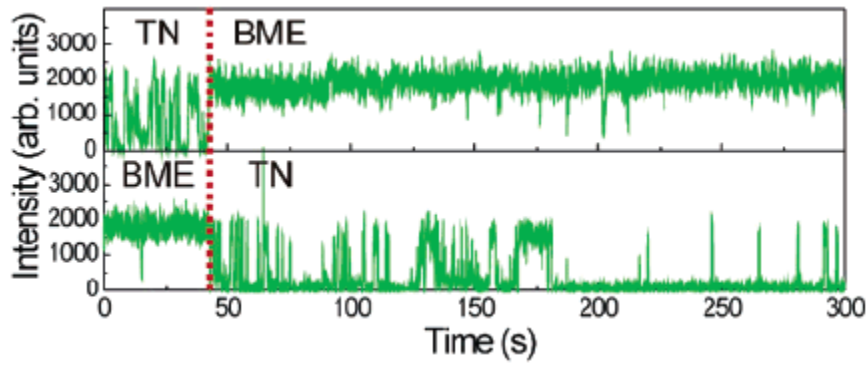


Figure 16. Intensity time trace for quantum dots passivated with buffer solution (TN) and BME. Blinking is almost entirely suppressed by passivation with thiol moieties, but reappears if replaced with buffer.

A second method to significantly suppress blinking is to surround the QD core with a thick shell of higher band gap material, confining carriers to the core of the QD. Chen et al [51] reported encouraging results for CdSe dots with a ZnS shell of 18-19 monolayers thickness. Because of the large lattice mismatch between ZnS and CdSe it's not possible to produce very thick shells without defects which in turn increase the susceptibility of a dot to blinking.

2.5. Summary

Numerous nanoscale systems have been found to exhibit some form of photoluminescence intermittency, although the mechanisms behind these processes is thought to differ. The blinking observed in quantum dots has been shown to obey a power law for both on and off times, over a range of times from microseconds up to many hours.

A significant body of research has been performed in order to understand the mechanism behind QD blinking, ultimately with the aim of controlling this phenomenon. The leading theories on blinking are those which predict the power law behaviour of the on/off times observed in the photoluminescence of quantum dots, such as that first proposed by Shimizu et al [36] and expanded on later by Tang et al [41, 42] with the DCET model.

The DCET model is a random-walk first-passage-time model. In its simplest form the off state arises due to tunnelling of an electron to a trap state in the vicinity of the QD core. The energy of both the trap state and the excited state of the dot move on a random walk where transitions between the states can only occur when they are in resonance. If a dot experiences a long off time it can be assumed that the two states are far from resonance and crossover back to the emitting state is unlikely. Rapid blinking of a QD is observed when the excited and trap states are close to resonance.

The electrostatic force microscopy measurements of Kraus et al [27] and Cherniavskaya et al [37-39] report a charging effect in QDs that, on a longer time scale looks similar to the optical blinking behaviour (measurements of the QD charge is not possible on timescales that are orders of magnitude lower than 1 second). A microscope combining both forms of microscopy; optical and scanning probe, could help to determine if there is in fact a relationship between the charging and photoluminescence intermittency of QDs.

2.6. References

1. Larson, D.R., et al., *Water-soluble quantum dots for multiphoton fluorescence imaging in vivo*. Science, 2003. **300**(5624): p. 1434-1436.
2. Alivisatos, A.P., W.W. Gu, and C. Larabell, *Quantum dots as cellular probes*. Annual Review of Biomedical Engineering, 2005. **7**: p. 55-76.
3. Michalet, X., et al., *Quantum dots for live cells, in vivo imaging, and diagnostics*. Science, 2005. **307**(5709): p. 538-544.
4. Brokmann, X., et al., *Highly efficient triggered emission of single photons by colloidal CdSe/ZnS nanocrystals*. Applied Physics Letters, 2004. **85**(5): p. 712-714.
5. Lounis, B., et al., *Photon antibunching in single CdSe/ZnS quantum dot fluorescence*. Chemical Physics Letters, 2000. **329**(5-6): p. 399-404.
6. Michler, P., et al., *Quantum correlation among photons from a single quantum dot at room temperature*. Nature, 2000. **406**(6799): p. 968-970.
7. Eisler, H.J., et al., *Color-selective semiconductor nanocrystal laser*. Applied Physics Letters, 2002. **80**(24): p. 4614-4616.
8. Malko, A.V., et al., *From amplified spontaneous emission to microring lasing using nanocrystal quantum dot solids*. Applied Physics Letters, 2002. **81**(7): p. 1303-1305.
9. Coe, S., et al., *Electroluminescence from single monolayers of nanocrystals in molecular organic devices*. Nature, 2002. **420**(6917): p. 800-803.
10. Robel, I., et al., *Quantum dot solar cells. Harvesting light energy with CdSe nanocrystals molecularly linked to mesoscopic TiO₂ films*. Journal of the American Chemical Society, 2006. **128**(7): p. 2385-2393.
11. Nirmal, M., et al., *Fluorescence intermittency in single cadmium selenide nanocrystals*. Nature, 1996. **383**(6603): p. 802-804.
12. Saito, R., et al., *Electronic structure of chiral graphene tubules*. Applied Physics Letters, 1992. **60**(18): p. 2204-2206.
13. Borovitskaya, E.S., M.S., *Quantum dots*. 2002: World Scientific.
14. Liao, M.C.H., et al., *Fabrication of ZnSe quantum dots under Volmer-Weber mode by metalorganic chemical vapor deposition*. Applied Physics Letters, 1997. **70**(17): p. 2256-2258.

15. Ledentsov, N.N., et al., *Reversibility of the island shape, volume and density in Stranski-Krastanow growth*. Proceedings of the 25th International Conference on the Physics of Semiconductors, Pts I and II, 2001. **87**: p. 375-376.
16. Damilano, B., et al., *GaN and GaInN quantum dots: an efficient way to get luminescence in the visible spectrum range*. Applied Surface Science, 2000. **164**: p. 241-245.
17. Li, J.W., Z.Z. Ye, and N.M. Nasser, *GaN-based quantum dots*. Physica E-Low-Dimensional Systems & Nanostructures, 2003. **16**(2): p. 244-252.
18. Xin, S.H., et al., *Formation of self-assembling CdSe quantum dots on ZnSe by molecular beam epitaxy*. Applied Physics Letters, 1996. **69**(25): p. 3884-3886.
19. Technologies, E. www.evidenttech.com. 2010 2010].
20. Murray, C.B., et al., *Colloidal synthesis of nanocrystals and nanocrystal superlattices*. Ibm Journal of Research and Development, 2001. **45**(1): p. 47-56.
21. Nagourney, W., J. Sandberg, and H. Dehmelt, *Shelved Optical Electron Amplifier - Observation of Quantum Jumps*. Physical Review Letters, 1986. **56**(26): p. 2797-2799.
22. Bopp, M.A., et al., *Fluorescence and photobleaching dynamics of single light-harvesting complexes*. Proceedings of the National Academy of Sciences of the United States of America, 1997. **94**(20): p. 10630-10635.
23. Bopp, M.A., et al., *The dynamics of structural deformations of immobilized single light-harvesting complexes*. Proceedings of the National Academy of Sciences of the United States of America, 1999. **96**(20): p. 11271-11276.
24. van Oijen, A.M., et al., *Spectroscopy of individual light-harvesting 2 complexes of Rhodospseudomonas acidophila: Diagonal disorder, intercomplex heterogeneity, spectral diffusion, and energy transfer in the B800 band*. Biophysical Journal, 2000. **78**(3): p. 1570-1577.
25. Pistol, M.E., et al., *Random telegraph noise in photoluminescence from individual self-assembled quantum dots*. Physical Review B, 1999. **59**(16): p. 10725-10729.
26. Haugen, G.M., et al., *PHOTODEGRADATION OF CDXZN1-XSE QUANTUM-WELLS*. Applied Physics Letters, 1995. **66**(3): p. 358-360.

27. Krauss, T.D., S. O'Brien, and L.E. Brus, *Charge and photoionization properties of single semiconductor nanocrystals*. Journal of Physical Chemistry B, 2001. **105**(9): p. 1725-1733.
28. Efros, A.L. and M. Rosen, *Random telegraph signal in the photoluminescence intensity of a single quantum dot*. Physical Review Letters, 1997. **78**(6): p. 1110-1113.
29. Banin, U., et al., *Evidence for a thermal contribution to emission intermittency in single CdSe/CdS core/shell nanocrystals*. Journal of Chemical Physics, 1999. **110**(2): p. 1195-1201.
30. Kuno, M., et al., *Nonexponential "blinking" kinetics of single CdSe quantum dots: A universal power law behavior*. Journal of Chemical Physics, 2000. **112**(7): p. 3117-3120.
31. Kuno, M., et al., *"On"/"off" fluorescence intermittency of single semiconductor quantum dots*. Journal of Chemical Physics, 2001. **115**(2): p. 1028-1040.
32. Eisberg, R. and R. Resnick, *Quantum physics of atoms, molecules, solids, nuclei and particles*. Quantum physics of atoms, molecules, solids, nuclei and particles, 1974: p. xci+713.
33. Neuhauser, R.G., et al., *Correlation between fluorescence intermittency and spectral diffusion in single semiconductor quantum dots*. Physical Review Letters, 2000. **85**(15): p. 3301-3304.
34. Schlegel, G., et al., *Fluorescence decay time of single semiconductor nanocrystals*. Physical Review Letters, 2002. **88**(13).
35. van Sark, W., et al., *Time-resolved fluorescence spectroscopy study on the photophysical behavior of quantum dots*. Journal of Fluorescence, 2002. **12**(1): p. 69-76.
36. Shimizu, K.T., et al., *Blinking statistics in single semiconductor nanocrystal quantum dots*. Physical Review B, 2001. **63**20(20).
37. Cherniavskaya, O., L.W. Chen, and L. Brus, *Imaging the photoionization of individual CdSe/CdS core-shell nanocrystals on n- and p-type silicon substrates with thin oxides*. Journal of Physical Chemistry B, 2004. **108**(16): p. 4946-4961.

38. Cherniavskaya, O., et al., *Photoionization of individual CdSe/CdS core/shell nanocrystals on silicon with 2-nm oxide depends on surface band bending*. Nano Letters, 2003. **3**(4): p. 497-501.
39. Cherniavskaya, O., et al., *Quantitative noncontact electrostatic force Imaging of nanocrystal polarizability*. Journal of Physical Chemistry B, 2003. **107**(7): p. 1525-1531.
40. Ben-Porat, C.H., et al., *Electric fields on oxidized silicon surfaces: Static polarization of PbSe nanocrystals*. Journal of Physical Chemistry A, 2004. **108**(39): p. 7814-7819.
41. Tang, J. and R.A. Marcus, *Single particle versus ensemble average: From power-law intermittency of a single quantum dot to quasistretched exponential fluorescence decay of an ensemble*. Journal of Chemical Physics, 2005. **123**(20).
42. Tang, J. and R.A. Marcus. *Determination of energetics and kinetics from single-particle intermittency and ensemble-averaged fluorescence intensity decay of quantum dots*. Journal of Chemical Physics 2006 Jul [cited 125 4]; Available from: <Go to ISI>://000239423600043
43. Pelton, M., et al., *Evidence for a diffusion-controlled mechanism for fluorescence blinking of colloidal quantum dots*. Proceedings of the National Academy of Sciences of the United States of America, 2007. **104**(36): p. 14249-14254.
44. Cordero, S.R., et al., *Photo-activated luminescence of CdSe quantum dot monolayers*. Journal of Physical Chemistry B, 2000. **104**(51): p. 12137-12142.
45. Maenosono, S., *Modeling photoinduced fluorescence enhancement in semiconductor nanocrystal arrays*. Chemical Physics Letters|Chemical Physics Letters, 2003. **367**(5-6): p. 666-70.
46. Maenosono, S., *Monte-Carlo simulations of photoinduced fluorescence enhancement in semiconductor quantum dot arrays*. Chemical Physics Letters, 2005. **405**(1-3): p. 182-186.
47. Maenosono, S., et al., *Optical memory media based on excitation-time dependent luminescence from a thin film of semiconductor nanocrystals*. Japanese Journal of Applied Physics Part 1-Regular Papers Short Notes & Review Papers, 2000. **39**(7A): p. 4006-4012.

48. Spinicelli, P., et al., *Non-Blinking Semiconductor Colloidal Quantum Dots for Biology, Optoelectronics and Quantum Optics*. Chemphyschem, 2009. **10**(6): p. 879-882.
49. Hohng, S. and T. Ha, *Near-complete suppression of quantum dot blinking in ambient conditions*. Journal of the American Chemical Society, 2004. **126**(5): p. 1324-1325.
50. Jeong, S., et al., *Effect of the thiol-thiolate equilibrium on the photophysical properties of aqueous CdSe/ZnS nanocrystal quantum dots*. Journal of the American Chemical Society, 2005. **127**(29): p. 10126-10127.
51. Chen, Y., et al., *"Giant" multishell CdSe nanocrystal quantum dots with suppressed blinking*. Journal of the American Chemical Society, 2008. **130**(15): p. 5026-+.
52. Harrison, P. *Quantum wells, wires and dots*. Wiley Interscience, 2006.

3. AN INSTRUMENT COMBINING SCANNING PROBE AND OPTICAL MICROSCOPY

3.1 Introduction

Scanning probe microscopy is the name given to a set of techniques initially developed to resolve features smaller than the diffraction limit of optical microscopes. These techniques have since been adapted to measure magnetic, electronic and numerous other properties of a sample. Scanning tunneling microscopy was the first of these techniques to be developed.

The invention of the scanning tunneling microscope allowed physicists to explore and manipulate the world on an unprecedented scale; to this day it remains a cornerstone of the scanning probe microscopy (SPM) field. Shortly after its invention the STM yielded the discovery of fullerenes, the structural composition of carbon nanotubes and important advances were made with semiconductor nanocrystals, eventually contributing to the realisation of the semiconductor nanoparticles known as quantum dots (QD). The scanning tunneling microscope (STM) won its inventors Gerd Binnig and Heinrich Rohrer the 1986 Nobel Prize for physics[1].

In STM the high spatial resolution is achieved by piezoelectric transducers controlling the distance between a tip of small radius of curvature (nm range) and the sample surface with picometer accuracy. An applied bias between tip and sample causes a tunneling current to flow when the tip-sample distance is in the nanometer range, comparable to the size of a few atomic orbitals. By adjusting the piezo extension by the applied voltage the tunneling current (and therefor tip/sample distance) is kept constant as the tip sweeps laterally over the sample, and a topographical map of the sample surface is constructed. With suitable noise isolation an STM is capable of atomic resolution even in ambient conditions. Its main drawback however is that only conductive samples can be imaged.

Developed by Binnig, Quate, and Gerber in 1986, the atomic force microscope (AFM) reconciled this problem[2]. In an AFM a sharp tip at the end of a flexible cantilever is employed to detect the forces felt at an atomic scale. To sense these forces, the cantilever is typically oscillating at or close to its resonant frequency and forces are measured as a deviation in the oscillation amplitude [2] or frequency [3], from which a topographical image is constructed. Interactions with the cantilever are commonly detected optically via a laser, deflected from the cantilever onto a position sensitive detector (PSD). Through careful selection of tip/sample conditions a wide variety of forces can be probed via the AFM technique. Electrostatic force microscopy (EFM) [4, 5] and magnetic force microscopy (MFM) [6] amongst others were developed in the years following the invention of the AFM. Because of its versatility AFM has become an invaluable tool for nanoscience.

Despite its numerous advantages, AFM, like the STM, also has its drawbacks. The resolution in AFM is typically lower than that achievable by STM. This is due to the exponential dependence of the tunnelling current with sub-nanometre decay in STM, compared to the Van-der Waals force decay that high resolution AFM relies upon. Secondly, the feedback loop employed to maintain constant cantilever frequency (or amplitude) necessitates a complex optical detection mechanism. The laser used in this process is incident close to the sample which can interfere with optically sensitive samples.

Some of these drawbacks can be overcome by replacing the AFM cantilever with a quartz tuning fork (QTF), identical to those used in most modern time keeping devices. A sharp tip is attached to one tine of the tuning fork to probe the sample. Electrochemical etching is the most popular method of tip production [7] although modified cantilever tips have also been used [8-10] .

The spring constant of a quartz tuning fork is several orders of magnitude higher than that of a silicon cantilever and the QTFs symmetry gives rise to a very low dissipative power. The amplitude of oscillation is much smaller than for a cantilever and has a resonance with a far greater quality factor, typically 10^4 in ambient conditions and 10^5 in vacuum. Consequently the minimum detectable force is significantly lower for a QTF probe. Quartz's piezoelectric nature allows for self sensing devices, negating the

need for an optical detection scheme and promoting the tuning fork as a force sensor for homebuilt AFM systems.

QTFs were first introduced to SPM by Gunther, Fisher and Dransfeld for use in acoustic near field microscopy [11] and as a distance control for optical microscopy by Karrai et al [12]. The latter also used tuning forks to study interfacial shear forces [13] and evaluated the QTF as a possible AFM force sensor [14]. Rychen et al also contributed to this area, observing the behaviour of QTFs at temperatures down to 1.5K [15, 16].

Because of the high Q-factor of a QTF there is a large time delay for the tuning fork amplitude to settle after experiencing a sudden change in force. Scan speed is therefore severely limited when operating in amplitude modulation (AM) mode; where the tip/sample distance is altered to achieve a set point oscillation amplitude. A frequency modulation (FM) technique incorporating a phase locked loop (PLL) was introduced for QTFs by Edwards et al [17], and shortly afterwards by Ihn et al [18] and Vorburger [19]. In this mode the tip/sample distance is altered in order to achieve a certain frequency shift of the oscillator. The time delay for the tuning fork frequency to change as a result of a force gradient is inversely proportional to the Q-factor of the tuning fork. In contrast to AM-AFM, in the FM-AFM mode the scan speed can be increased by using high-Q sensors.

Adding a tip to a QTF causes an asymmetry in its configuration; this will cause a decrease in the quality factor of the sensor. Balancing the other tine of the prong with additional mass can improve but not completely resolve the symmetry of the tuning fork. In addition to this, scanning forces are experienced at only one tine of the tuning fork and can not be compensated for. Accurately determining the response of a QTF sensor becomes quite complex under this regime, a problem that can be overcome by firmly fixing one of the tuning fork beams; reducing the system to a single piezoelectric cantilever. This “Qplus” arrangement was developed by Giessibl et al [20] and was used to observe not only the first AFM atomic resolution images on Si(111)-(7x7) [21] but has also achieved sub-atomic resolution [22].

QTF AFMs have only been capable of atomic resolution in ultra high vacuum and at liquid helium temperatures. An exception to this is Seo et al [23] who use a trident shaped tuning fork and an excitation mode whereby the central prong of the trident extends and retracts. Atomic resolution on cleaved mica was observed in ambient conditions by this method.

Electrical measurements of a sample can be obtained by employing a conductive tip in the AFM mode. These include tunnelling AFM, resistivity measurements and capacitive measurements. Introduced by Nonnenmacher et al[4], Kelvin probe microscopy is another of these techniques, it provides a measurement of the surface potential directly, a technique based on the classical vibrating Kelvin capacitor. If an external potential difference is applied between the tip and sample there will be an electrostatic force experienced by the tip. If the tip and sample are two different materials with different work functions then there is an electrostatic force between the two even in the absence of an externally applied potential difference. In Kelvin probe microscopy this force is nullified by the application of an external potential difference, the magnitude of which is a direct measure of the difference in work functions of the tip/sample materials.

Initially KPM was performed by a 2-pass technique, this remains the most common method of KPM; first the topography of the sample is measured, then the tip is withdrawn and is moved over the sample at a fixed height using the topographical data, during this second pass electronic measurements are performed. Subsequently techniques have been realised to allow for simultaneous AFM and KPM measurements to be made[24, 25].

The optical and electronic properties of semiconductor nanocrystals are interdependent, so a microscope capable of both scanning probe and optical techniques is advantageous for their study. Complications arise because both the SPM and optical microscope must be aligned on the same region of the sample. Putman et al [26, 27] were one of the first groups to combine these two forms of microscopy; using the optical microscope to locate low concentration biological samples before scanning with AFM. Stuart and Hlady [28, 29] used a commercial “stand alone” SPM head combined with an inverted optical microscope. They use

reflection interference contrast microscopy (RICM) to measure tip sample separation distances and cantilever deformations due to biotin ligand adhesion whilst performing AFM.

Nishida et al [30] amongst others [31, 32] have combined SPM and optical microscopy techniques using stand alone SPMs and inverted optical microscopes similar to that described by Stuart and Hlady.

Total internal reflection fluorescence microscopy (TIRFM) is an optical microscopy technique whereby the sample is illuminated only by the evanescent field (the field perpendicular to the direction of propagation) of the laser beam. The advantage of this technique is that the evanescent field decays at a distance greater than about 100nm above the sample, so contributions to the optical output are restricted to the sample alone. Mathur et al have combined AFM with TIRFM [33]; using it to examine the transmission of force from the apical membrane to the basal membrane in endothelial cells. They used a prism to direct a laser into an optical waveguide on which the sample is mounted.

Commercially available scanning probe/optical microscopes have recently become available, as demonstrated by Trach et al [34], and Owen et al [35]. It is important to note that a large proportion of microscopes combining SPM and optical microscopy have been developed to study biological samples, only very few studies on QDs utilising both forms of microscopy have been performed[35, 36].

For our microscope we choose to arrange the SPM, sample and optical microscope horizontally as opposed to the more common vertical arrangement. For our application the microscope will be positioned on an optical bench; a horizontal arrangement allows for easier alignment of the optical equipment on the sample. The SPM and sample are mounted on separate xyz translation stages (Attocube piezos and home-built positioners) whilst the microscope objective remains fixed. There are several advantages to this arrangement. Most importantly is that both the sample and SPM tip can be scanned, which is advantageous for different forms of microscopy. Very few microscopes have been constructed in this way; Larcheri et al [37] have

used a horizontal arrangement, but use an etched optical fiber as both the SPM tip and optical input to their microscope.

Both scanning force microscopy (SFM) and optical microscopy (OM) are well established methods of probing materials. Despite both techniques offering different information regarding the sample under scrutiny, these two forms of microscopy have rarely been combined into one simultaneously operating microscope. In numerous microscopic materials their optical and electronic properties are thought to be intimately related. The ability to simultaneously measure both of these characteristics offers real time evidence of their partnership. This section describes the design and operation of our combined scanning force and optical microscope.

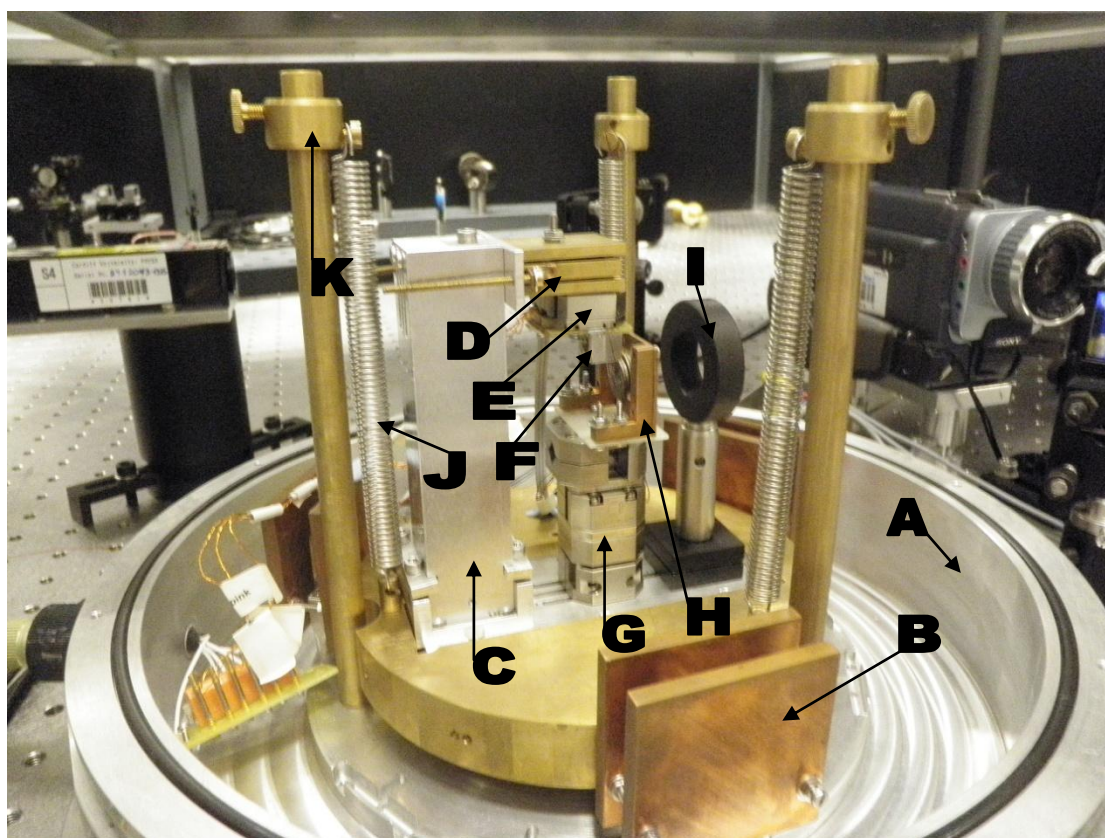


Figure 1. Overview of the microscope. A) Bottom section of cryostat chamber, B) Magnetic damping, C) Homebuilt vertical and lateral mechanical positioning stage, D) Homebuilt piezo stepper, E) Scanning Attocube, F) Tuning fork holder, G) Coarse Attocube stack, H) Sample holder, I) Optical objective mount, J) Vibration isolation springs, K) Clamps for spring height adjustment.

With its extreme sensitivity to the forces on the nanometre scale, efficient vibration isolation and damping are an essential component of SFM. It is important that the

SFM components are as rigid as possible and that they are anchored securely. The microscope head is suspended on springs and eddy current damping is employed to damp the resonant modes of the system and further improve the vibration isolation.

A laser beam enters the vacuum chamber and cryostat through a quartz window and is incident on a fixed objective held in the objective holder (component I in Fig.1). The fluorescence from the sample can be monitored by either a spectrometer & a CCD camera, by a Photomultiplier or an avalanche photodiode using photon counting.

3.2 The microscope cryostat

Our microscope chamber is a cylinder cut from a single piece of aluminium rod. The chamber has an external height of 0.28m and diameter 0.3m, with an internal volume of roughly 0.06m^3 . The electrical feed-throughs and the vacuum pump connection are located around the base of the chamber; first, in an effort to reduce the coupling of vibrations to the microscope head and secondly so that the upper part of the chamber can be removed completely without having to disconnect any of the instrument electronics. The electronic feed-throughs are Oxford Instruments 10pin feed-throughs for piezo connections, and single BNC feed-throughs for tuning fork and tip/sample voltages for KPM measurements. All are suitable for high vacuum and cryogenic applications.

Because the volume of the chamber is relatively small a KF25 flange is sufficient for the vacuum pump connection. A membrane pump and turbo pump are used to achieve a pressure of 10^{-5}mbar within several minutes of pumping. The quality of the vacuum needs only be sufficient to remove the surface layer of water that inevitably covers any material under ambient conditions. With the surface layer of water removed the quartz tuning forks are sensitive to the attractive forces (Van-der Waals and electrostatic forces) of the sample, allowing for non-contact (NC) AFM.

The optical feed through for the laser line is a 25mm diameter fused silica cylinder with Vis0 coating (Edmund optics). The window is positioned 0.12m from the

chambers base, centred at the beam line height; it has a thickness of 3mm. The reflectance against wavelength behaviour of the window is shown in Fig. 2.

Though not utilised yet there is an additional feed through for cooling the sample mounted inside the chamber. This feed through would consist of a pipe that enters and terminates within the chamber, with a copper braid connecting it to the copper sample mount. Liquid nitrogen fed into the pipe could then be used to cool the sample.

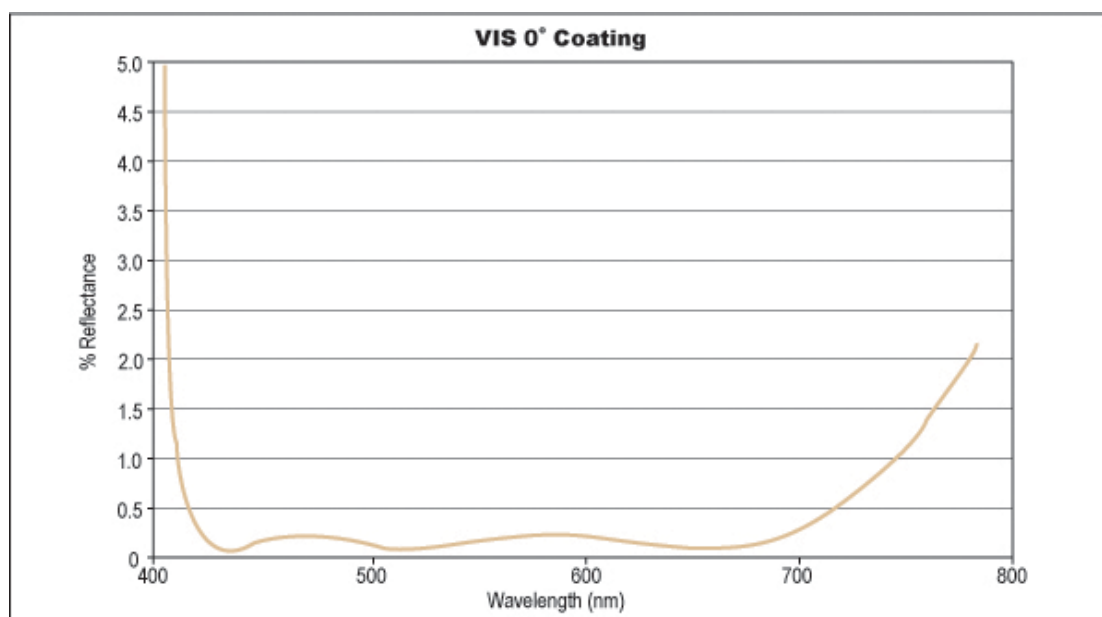


Figure 2. Optical characteristic of the fused silica optical feed-through.

The upper lid of the chamber houses a larger 100mm diameter borosilicate observation window of 6.5mm thickness. This window allows the user to quickly position the tuning fork close to the sample surface using the coarse positioning piezos. The 3 chamber sections and all of the feed-throughs are sealed by nitrile o-rings to which pressure is applied via tightening screws around the flanges.

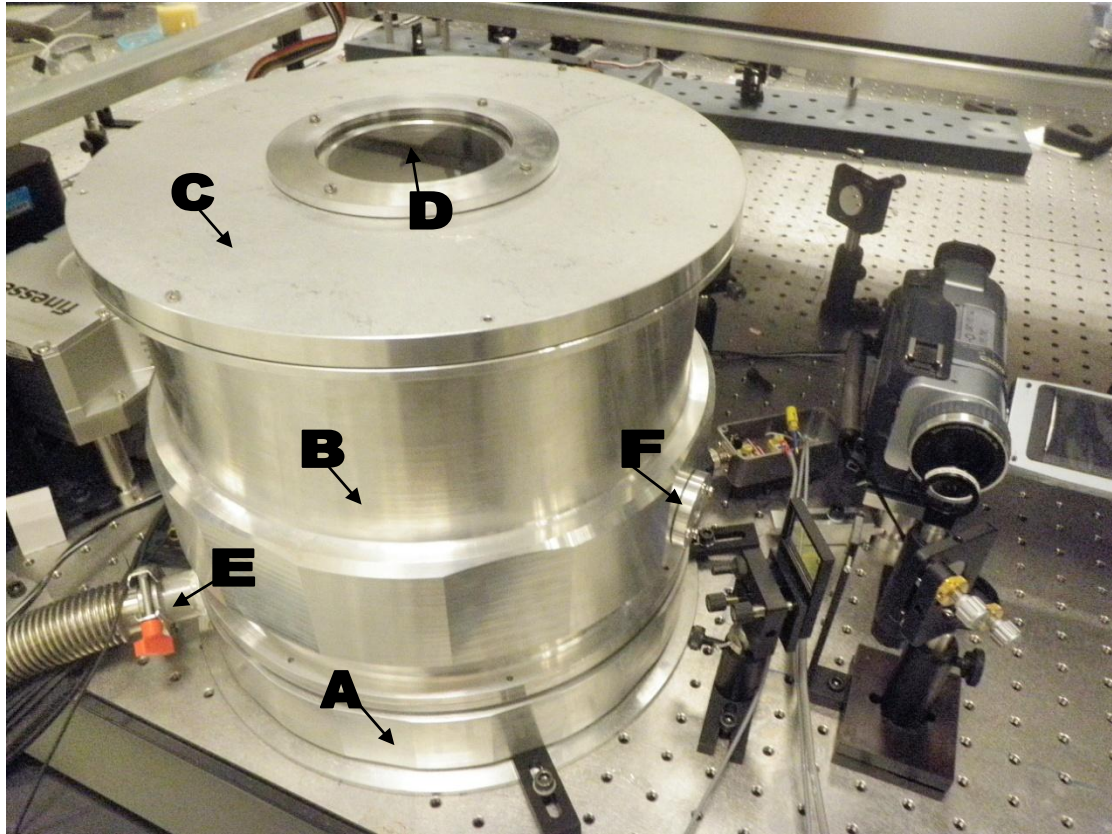


Figure 3. Photo of the cryostat chamber. A) Lower section of cryostat chamber, B) Middle section of cryostat chamber, C) Cryostat lid, D) Viewing window, E) Vacuum pump connection, F) Quartz window for optical microscope input/output.

3.3. Vibration isolation

Effective vibration isolation is paramount in achieving stability in any SPM application. Our vibration isolation stage combines spring suspension and magnetic damping.

For the magnetic damping we use 25x25x5mm neodymium magnets (with poles on the 25x25mm faces) sandwiched between two 50x50x5mm copper plates. The magnets are mounted at the base of the vacuum chamber using vacuum compatible adhesive and the copper plates are mounted to the spring suspended brass disc upon which the microscope is mounted. The plates are copper - C10100, with a resistivity of $1.71 \times 10^{-8} \Omega \text{m}$. There is a roughly 3mm space between the copper sheets and the magnets poles, located on the 25x25mm faces of the magnets. The magnets produce a

field strength of roughly 0.27T at the pole faces. Our setup can facilitate either three or six magnets arranged symmetrically around the base plate of the microscope.

If the system is under-damped the vibration isolation is more efficient at higher frequencies but there are large oscillations at the resonant frequency of the spring system. If over-damped, then the opposite is true; the resonance oscillation is damped but higher frequency oscillations are coupled more strongly to the microscope. Park et al[38] state that the latter is true even with critical damping and suggest using a damping coefficient of $\gamma = 0.1\omega_0$, where ω_0 is the resonance frequency of the spring system, given by:

$$\omega_0 = \sqrt{\frac{g}{\Delta L}} \quad [\text{Eq. 1}]$$

where g is the acceleration due to gravity and ΔL is the spring extension length as a result of the weight of the attached microscope. The mass of the vibration isolation stage increases with increasing number of magnets, giving resonant frequencies of 2.35Hz, 2.09Hz and 2.56Hz for zero, three and six magnets respectively. A different set of springs were applied when six magnets were used giving rise to the increased resonance frequency for this arrangement.

To test the effectiveness of our magnetic damping, displacement/time data was recorded with the various magnetic arrangements. A video recorder capturing 25 frames per second was used to record data.

The oscillation amplitude of a damped system is given by:

$$A = A_0 e^{(-\gamma t)} \quad [\text{Eq. 2}]$$

where A is the displacement after a time t , given an initial displacement A_0 . The displacement/time data is fitted with Eq. 2 to find the damping coefficient for the different magnetic arrangements, this is shown in Fig. 4. γ was found to be 0.15, 1

and 1.75 for zero, three and six magnets respectively. Comparison to the suggested value from *Park et al* can be found in table 1. The arrangement using six magnets satisfies the required damping conditions slightly better than using 3 magnets, however, the extra mass of the 6 sets of copper plates requires a stiffer spring suspension with a higher resonant frequency. For this reason the chosen vibration isolation features 3 damping magnets and the springs giving the lowest resonant frequency. These springs are stainless steel extension springs with a spring constant of 160Nm^{-1} .

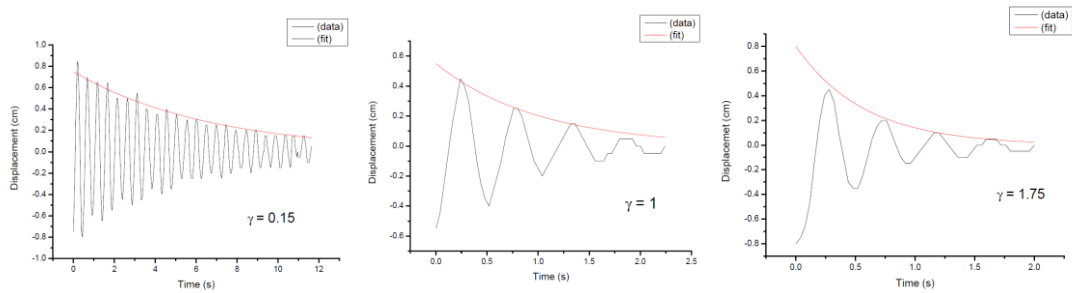


Figure 4. Displacement versus time data for the magnetic damping and vibration isolation of the microscope (black), fitted using Eq2 (red) to obtain the damping coefficients (γ) with zero, 3, and 6 magnets in the left, middle, and right graphs respectively.

Table 1. Comparison of the measured damping coefficients and those suggested by *Park et al*.

| # of magnets | γ (from experiment) | $0.1\omega_0$ |
|--------------|----------------------------|---------------|
| 0 | 0.15 | 1.48 |
| 3 | 1.00 | 1.32 |
| 6 | 1.75 | 1.61 |

3.4. Positioning Devices

For a standalone SPM system two sets of positioning devices are typically employed. First is the scanning piezos controlling the tip motion in three dimensions while measuring the surface topography. The scanning piezos will normally have a limited range in the order of 10 microns to have sufficient resolution - but have a movement that can be controlled on the picometre scale. A second set of positioning devices is usually used for coarse movement of either the tip or sample, so that the tip can be brought quickly to a point close to the sample surface and for changing the area of the sample to be imaged. It's common to find piezos being used as coarse positioning motors, but micrometers are also used.

Our system requires that both the optical microscope and SPM be focused on the same region of the sample. For this a second set of coarse positioning devices is required. The following section details the combination of commercially available and home built positioning devices used to align the optical and scanning probe microscopes.

3.4.1. Piezos

An Attocube ANSxyz100 is used for the high resolution scanning part of the AFM. This piezo can operate over a temperature range of 1-300K, under high vacuum and in magnetic fields of up to 20T. The scan range of the ANSxyz100 is 40x40x24 μ m with a control voltage of 0-60V in all three directions. With our orientation of the scanning Attocube, our tip/sample range is 40 μ m and our scan area is 40x24 μ m. The voltage amplifier for this piezo is an ANC200, also by Attocube. This amplifier has external inputs for connections to the SPM software. It is to this piezo that the QTF is mounted.

A set of Attocube piezo motors are used to control the position of the sample relative to the microscope objective. An ANPxyz100 coarse positioning stack consisting of two ANPx100 piezos for lateral positioning and one ANPz100 piezo for vertical positioning give three degrees of freedom for the sample. The lateral piezos have a

travel range of 7mm and the vertical piezo has a 6mm travel range. These piezos are inertial motors, driven by a saw tooth voltage supplied by an ANC150 voltage amplifier also from Attocube. The advantage of this is that once positioned there is no voltage applied to these positioners, therefore a high degree of stability and precision is achievable. The smallest reproducible step size of these piezos is about 100nm. The ANPxyz100 piezos will function in the same environment as the scan Attocube, and are also compatible with the ANC200 scan controller, allowing these piezos to also be used as scanning piezos if necessary.

3.4.2. Inertial slider

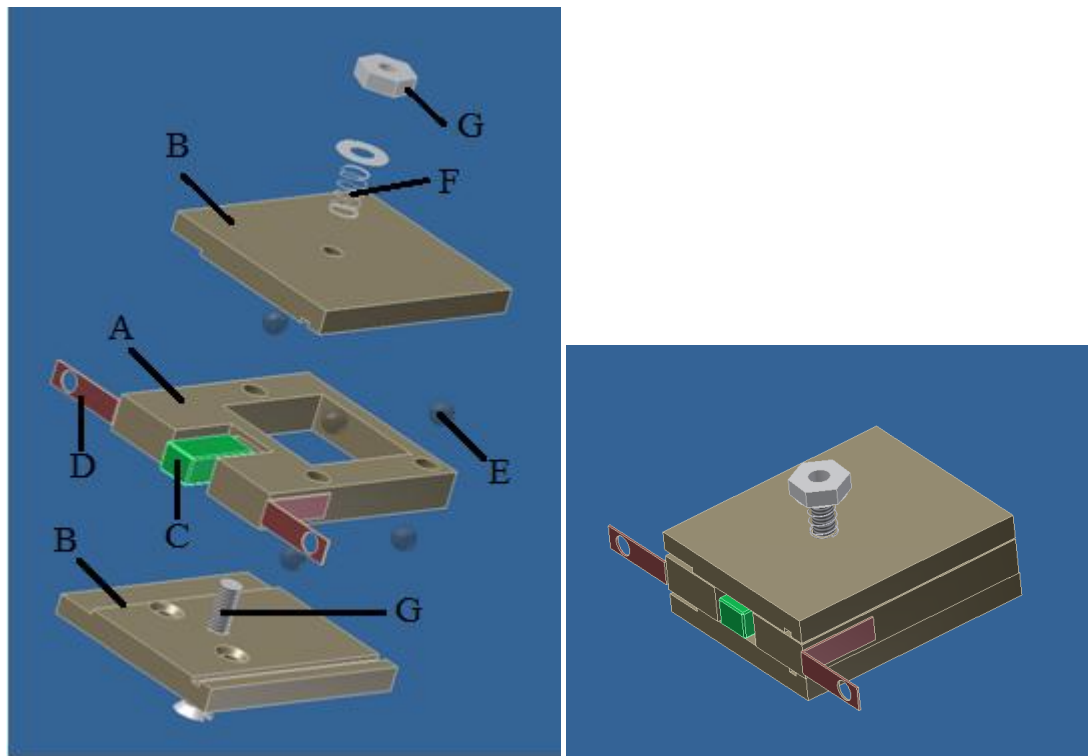


Figure 5. Exploded (left) and assembled (right) images of the inertial slider. Part A – central brass plate, part B – outer brass plates, part C – piezoelectric stack, part D – phosphor bronze legs, part E – sapphire spheres, part F – compression spring, part G – nut & bolt.

The scanning Attocube is mounted on the underside of a homebuilt inertial slider inspired by *Silveira et al*[39]. The design is based around three brass plates sandwiched together. The central plate (part A) is 30mm in length and 25mm wide with a thickness of 4.5mm, there is a recess at its base for a piezoelectric stack (part

C) which is the driving element of the inertial slider. An L-shape phosphor bronze leg (parts D) of 1mm thickness and the same width as the central plate is screwed to each side of the central plate at its base, these legs protrude 25mm from the brass and are used to mount the inertial slider. There are three recesses on each side of the central brass plate to accommodate sapphires spheres (part E) of 3mm diameter, the holes are a push fit and leave about 1.25mm of the sapphire balls protruding.

The outer brass plates are the same length and width as the central plate but have a thickness of only 3mm. A groove is cut down the length of one side of each plate and the other side is milled to the same depth and polished. The sapphire balls of the central plate run along the groove and the polished part of the outer plates. An M2.5 bolt (part G) passes through the centre of the two outer plates and a rectangular hole cut into the central plate, a small compression spring (part F) is wrapped around the bolt where it leaves the opposite outer plate and a nut is used to tighten the spring and exert a force pushing the three plates together. The only contact points between the three brass plates are at the sapphire balls and the outer plates have a travel distance of roughly 6mm in the direction of the grooves.

The piezoelectric stack is 10mm in length and has a maximum extension of 9.1 μ m at 150V applied bias under no load. It fits into a 9.5mm recess at the base of the central plate so that a small amount of the piezo stack protrudes from the central plate. When the mounting screws at the end of the phosphor bronze legs are tightened the piezo stack is sandwiched between the inertial slider and its mount. A saw tooth waveform generated by the SPM software is amplified (Piezomechanik SVR150-3) and applied to the piezoelectric stack. During the slow voltage increase stage of the saw tooth waveform the whole inertial slider moves forward as one, however, during the fast decrease stage of the saw tooth voltage the inner plate withdraws quickly and the outer plates remain in almost the same position – sliding over the sapphire balls. The scanning piezo attached to the outer plates effectively moves forward by some small amount. The inertial slider can be made to travel in the opposite direction by reversing the direction of the applied saw tooth waveform.

The inertial slider was calibrated by measuring the change in capacitance between two copper plates of 15x15mm. One plate was attached to the scanning Attocube

mounted on the underside of the inertial slider, and the second held stationary, with a constant separation of 1mm. An Andeen Hagerling ultra precision capacitance bridge was used to obtain measurement of the capacitance, operated in continuous mode remotely by the computer acquiring data.

The capacitance between the copper plates is given by

$$C = \frac{\epsilon_0 A}{d} = \frac{\epsilon_0 w l}{d} \quad (\text{Eq. 3})$$

$$\Delta l = \frac{d}{\epsilon_0 A} \Delta C \quad (\text{Eq. 4})$$

where w is the width of the copper plate, l is the length of overlapping plates and d is the separation distance between the plates. ΔC is the change in capacitance per voltage pulse sent to the piezo stack, and Δl is the distance moved by the inertial slider as a result of a voltage pulse.

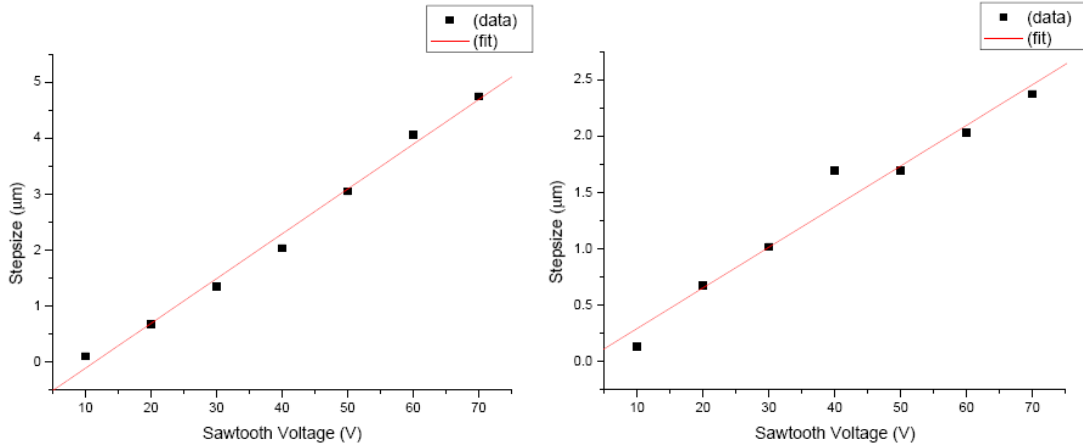


Figure 6. Step sizes (distance travelled) in the approaching (left graph) and withdrawing (right graph) directions of the inertial slider.

Figure 6 shows the average step size; the distance travelled by the piezo stepper, against applied saw tooth voltage to the piezo stack. Data points are the average step size over 1000 saw tooth waveforms applied at 10Hz. The inertial slider is held at a slight incline due to gravity and therefore step sizes are larger in the forward (approaching) direction than in the backwards (withdrawing) direction. The smallest reproducible step size in the approaching direction is about 100nm at 10V, this is

much smaller than the scanning Attocube range in the same direction (40 μ m). Below this voltage the inertial slider fails to move more frequently.

The inertial slider is controlled via the GXSM software (discussed in more detail in section 3.6.2.). A large number of voltage pulses can be sent manually to the inertial slider to rapidly decrease the tip/sample separation distance if it is large, when the tip is reasonably close to the sample the automatic approach function of the software is launched which withdraws the scanning piezo, sends a voltage pulse to the inertial slider and finally re-approaches the scan piezo to attempt bringing the tip into contact. This process is repeated until the AFM is brought into feedback, a process that typically takes no longer than a few minutes and safeguards against tip crashes.

3.4.3. Coarse positioning devices

The coarse Attocube stack allows us to bring any region of the sample into focus of the optical objective. The inertial slider can then bring the AFM tip near to contact with the sample surface so that the scanning Attocube can begin scanning. However, more positioning devices are required so that the AFM tip can be brought to the same region of the sample that is in the optical objective focus. As already mentioned we choose to leave the optical objective fixed, so two coarse positioners are required on the AFM part of the microscope that allow for degrees of freedom in directions perpendicular to the sample normal. To achieve this, the inertial slider and scanning Attocube are mounted on a homebuilt lockable translation stage, shown in Fig. 5.

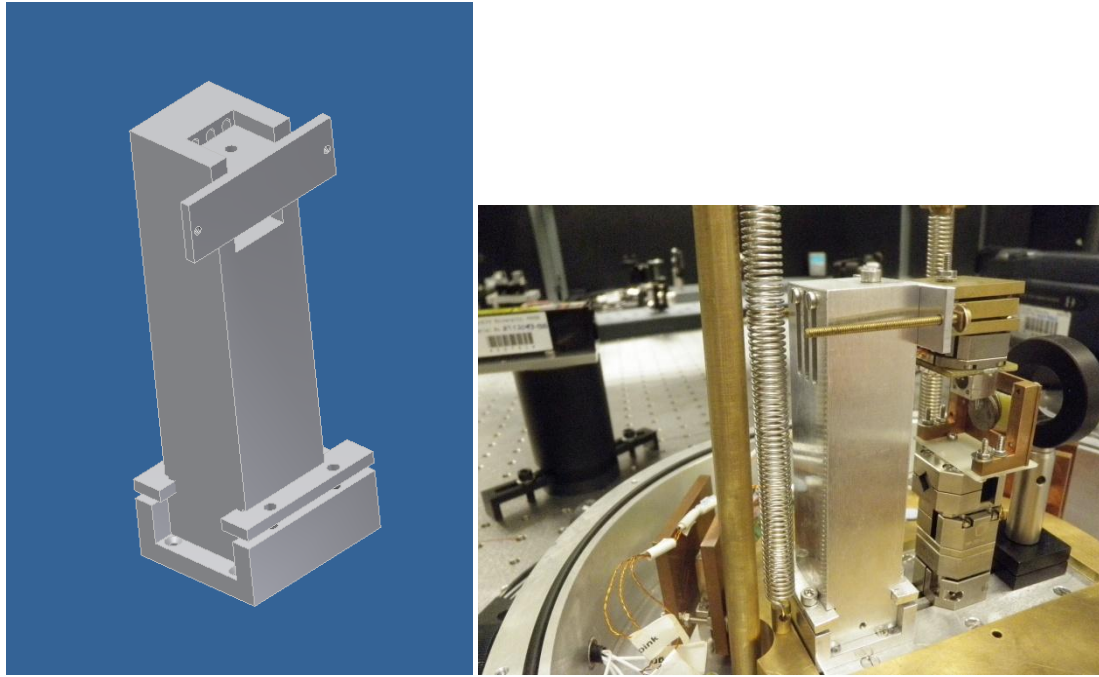


Figure 7. The lockable translation stage, with the lateral positioner at the base, and the vertical positioner mounted above.

Several important considerations are to be made when designing such a device. The travel distance and sensitivity must be chosen so that the AFM tip can be brought over a reasonable area of the sample (within the field of view of the objective, $\sim 100\mu\text{m}$), and the tip must be close to the centre of the sample when the translation stages are at the middle of their full range. Rigidity is also of utmost importance, so both translation stages must be able to be secured in place once their position has been set.

The translation stages consist of two elements; a lateral positioner at the base and a vertical positioner mounted on top of it to which the AFM head is mounted. The lateral positioner at the base consists of an aluminium tray in which the upper vertical positioner rests and can slide back and forth with a travel distance of $\pm 2.5\text{mm}$. An M2.5 bolt passes through the wall of the base tray and into a threaded hole near the bottom of the vertical positioner. A 4mm diameter compression spring is coiled around the bolt so that the bolt head is held firmly against the base tray wall. The bolt has a pitch of 0.3mm giving a movement of about $30\mu\text{m}$ for $1/10^{\text{th}}$ of a revolution, which is reasonable to induce with a suitable hex key. When correctly positioned four bolts around the base tray can be tightened to firmly fix the lateral positioner.

The vertical translation stage consists of an aluminium block to which the inertial slider/AFM scanner is mounted. An M3 bolt passes through a hole in the centre of the block and is threaded into the aluminium bar that allows for movement in the lateral direction. In a similar way to the lateral translation stage, a compression spring is wrapped around the M3 bolt so that an upwards force is exerted on the block holding the AFM scan head. Movement in the vertical direction is controlled by turning this bolt. The M3 bolt has a thread pitch of 0.5mm, giving a slightly larger movement of about 50µm for 1/10th of a revolution. When positioned correctly the vertical translation stage can be fixed by three screws mounted on its rear side.

3.5. Quartz tuning forks

3.5.1. Overview

Most AFM systems use a silicon cantilever as a force sensor. A dither piezo is typically used to excite the cantilever at its resonance frequency and a laser reflected off the back of the cantilever onto a photo-sensitive detector (PSD) is used to detect the resonance frequency and amplitude of oscillations.

Quartz tuning forks identical to those found in most time keeping devices have several advantages over the silicon cantilever. The piezoelectric property of QTFs allows for excitation by an electrical signal and also means that changes in oscillation frequency and amplitude can be measured in the same way, without the need for an optical detection scheme. This is particularly advantageous when the sample of interest is sensitive to light.

Quartz tuning forks have a spring constant that is significantly larger than that of a silicon cantilever, typically by a factor of 10³. The QTF's spring constant is high compared to the interaction forces experienced in AFM. This avoids the snap-to-contact experienced by cantilevers and allows oscillations at a lower amplitude, thus achieving higher resolution.

Finally, compared to quartz, silicon cantilevers suffer a severe drift in eigenfrequency with thermal fluctuations. Quartz can be cut along certain crystal orientations so that variation of oscillation frequency is almost zero for a given temperature.

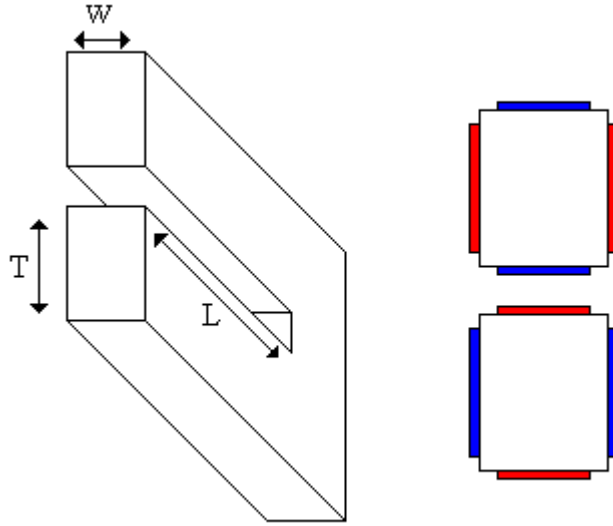


Figure 8. Cartoon representation of the quartz tuning forks and their electrode configuration. The tuning fork tines have a length (L) of 3.9mm, thickness (T) of 600 μ m, and width (W) of 350 μ m.

Initially the QTFs are hermetically sealed in a vacuum cylinder. The cylinder can easily be removed by carefully cutting around the base of the chamber. Once removed, the tuning fork is mounted in a stainless steel block. The block is 10mm³ and is split into two sections at a 15° angle, the tuning fork fits into a recess between the two sections and four screws on top of the block are used to tighten and fix the tuning fork in position. The angle of the tuning fork is chosen so that when mounted the tip apex extends beyond the block and makes contact with the sample surface prior to any other part of the microscope head.

3.5.2. Mechanical model

The equation of motion for a tuning fork is described by a coupled harmonic oscillator, with equations for each tine of the fork with piezoelectric coupling constant α and driven by a voltage U_0 [18],

$$\begin{aligned}
m_1 \ddot{x}_1 + \gamma_1 \dot{x}_1 + k_1 x_1 + \gamma_C \dot{x}_2 + k_C x_2 &= -\alpha U_0 \\
m_2 \ddot{x}_2 + \gamma_2 \dot{x}_2 + k_2 x_2 + \gamma_C \dot{x}_1 + k_C x_1 &= \alpha U_0 + F_{tip}
\end{aligned}
\tag{Eq. 5}$$

where m_i , γ_i and k_i are the effective masses, damping constants and spring constants respectively of the tuning fork tines. γ_C and k_C are coupling constants between the two prongs of the tuning fork. The tip is mounted on the m_2 . The deflection of the tuning fork prongs is given by x_i , F_{tip} is the tip/sample interaction force experienced by one of the prongs. Connecting a tip to one prong of the tuning fork disturbs the symmetry of the system and if the additional mass is large enough the introduced asymmetry will lead to mode mixing between the symmetric and antisymmetric modes of the tuning fork. The eigenmodes of the QTF are given by

$$\Omega_{1,2}^2 = \omega_0^2 \pm \omega_C^2 \sqrt{1 + \kappa} \tag{Eq. 6}$$

where:

$$\begin{aligned}
\omega_0^2 &= \frac{1}{2} \left(\frac{k_1}{m_1} + \frac{k_2}{m_2} \right) \\
\omega_C^2 &= \frac{k_C}{\sqrt{m_1 m_2}} \\
\kappa &= \frac{\sqrt{m_1 m_2}}{2k_C} \left(\frac{k_1}{m_1} - \frac{k_2}{m_2} \right)
\end{aligned}
\tag{Eq. 7}$$

in the anti-symmetric mode the prongs of the tuning fork oscillate 180° out of phase, it is this mode that the tuning fork electrodes are arranged to excite. In the symmetric mode the tuning fork prongs oscillate in phase. Given that $\kappa \ll 1$ there is no significant mixing of the modes. In the absence of a tip the difference in mass of the tines of the tuning fork is negligible, so $m_1 = m$, $m_2 = m + \Delta m$, where Δm is the additional mass of the tip. This additional mass is almost entirely consisting of the droplet of adhesive used to fix the tip to the tuning fork. Treating this droplet as a half sphere, its mass is given by $2\pi r^3 \rho / 3$, with radius (r) = 150 μm and ρ is the density of the adhesive (Epotek H21D) = 2450 kgm^{-3} , giving $\Delta m \sim 20 \mu\text{g}$. The difference in spring constant between the two prongs of the QTF is again negligible, and is not

changed by addition of a tip, so $k_1 = k_2 = k$. The value of k_C can be found from finite element analysis and is of the order of 10^2 [40, 41]. Rewriting eq. 3:

$$\kappa = \frac{\sqrt{m(m + \Delta m)}}{2k_C} \left(\frac{k\Delta m}{m(m + \Delta m)} \right) \quad (\text{Eq. 8})$$

from eq. 8 the value of κ is found to be $\sim 5 \times 10^{-6}$, the tuning fork operates in the regime of small mode mixing. From this it is reasonable to assume also that $\gamma_1 = \gamma_2 = \gamma$ and $\Delta m + m_1 = m_2 = m$. Substituting these values into equation 5 we can obtain the sum and difference forces between the two tines of the tuning fork

$$\begin{aligned} m\ddot{\theta} + (\gamma + \gamma_C)\dot{\theta} + (k + k_C)\theta &= \frac{F_{tip}}{2} \\ m\ddot{\phi} + (\gamma - \gamma_C)\dot{\phi} + (k + k_C)\phi &= 2\alpha U_0 + F_{tip} \end{aligned} \quad (\text{Eq. 9})$$

where θ is the difference in amplitude (centre of mass coordinate) of the two prongs $\theta = (x_1 + x_2)/2$, and ϕ is the difference in position of the two tuning fork tines $\phi = x_2 - x_1$. The large static spring constant of the tuning fork gives rise to restoring forces that are typically 10^5 times greater than the tip interaction force, therefore our final approximation is that $x_1 = x_2 = x$ and therefore $\theta = 0$. We obtain the final equation of the tuning fork by substitution of these values into eq. 5:

$$\ddot{x} + \frac{\omega_0}{Q}\dot{x} + \omega_0^2 x = \frac{\alpha U_0}{m} + \frac{F_{tip}}{m} \quad (\text{Eq. 10})$$

where $(k - k_C)/m = \omega_0^2$ and $(\gamma - \gamma_C)/m = \omega_0/Q$. [18].

3.5.3. Electrical equivalent model

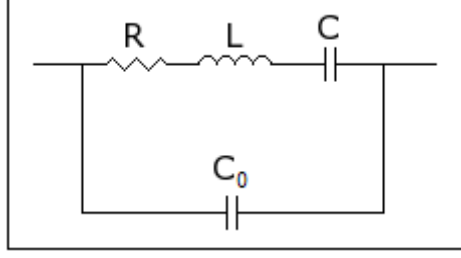


Figure 9: Equivalent electronic circuit for quartz tuning fork.

The response of a QTF is that of an RCL circuit, as shown in Fig. 9. There is an additional capacitive term C_0 due to the parasitic capacitance of the connecting leads. Modelling the QTF in this way allows properties such as the quality factor and resonance frequency to be determined. When a voltage is applied to one set of the QTF electrodes the resulting movement due to Quartz's piezoelectric behaviour induces a current at the other set of electrodes, the induced current is given by:

$$A = \frac{V_0}{R + \frac{1}{i\omega C} + i\omega L} + iV_0\omega C_0 \quad (\text{Eq. 11})$$

where A is the induced current, V_0 is the drive voltage, R is the resistance, C is the capacitance, L is the inductance and C_0 is the parallel capacitance. The quality factor and resonant frequency of the tuning fork are given by

$$Q = \frac{1}{R} \sqrt{\frac{L}{C}} \quad (\text{Eq. 12})$$

$$f_0 = \frac{1}{2\pi} \frac{1}{\sqrt{LC}}$$

(Eq. 13)

Figure 8 shows the frequency response of a tuning fork whilst hermetically sealed (a), removed from its vacuum cylinder (ambient conditions) (b) and within the

microscope vacuum chamber (c). The quality factor can be found by curve fitting equation 11 to the frequency response data. A lock-in amplifier was used in all three cases to simultaneously drive the tuning fork and measure the current response, the driving voltage was 0.1V. The data acquired from curve fitting is shown in table 2.

Table 2. Tuning fork characteristics obtained from curve fitting to data shown in fig 8.
a) hermetically sealed QTF, b) vacuum cylinder removed, c) in microscope vacuum chamber.

| Condition | Δf (Hz) | R (k Ω) | C (x10 ⁻¹⁵ F) | L (kH) | Q (x10 ³) |
|-----------|-----------------|-----------------|--------------------------|--------|-----------------------|
| a | - - | 100 | 0.9 | 26.2 | 54 |
| b | -4.5 | 300 | 1.25 | 18.8 | 13 |
| c | +2.5 | 85 | 1 | 23.6 | 57 |

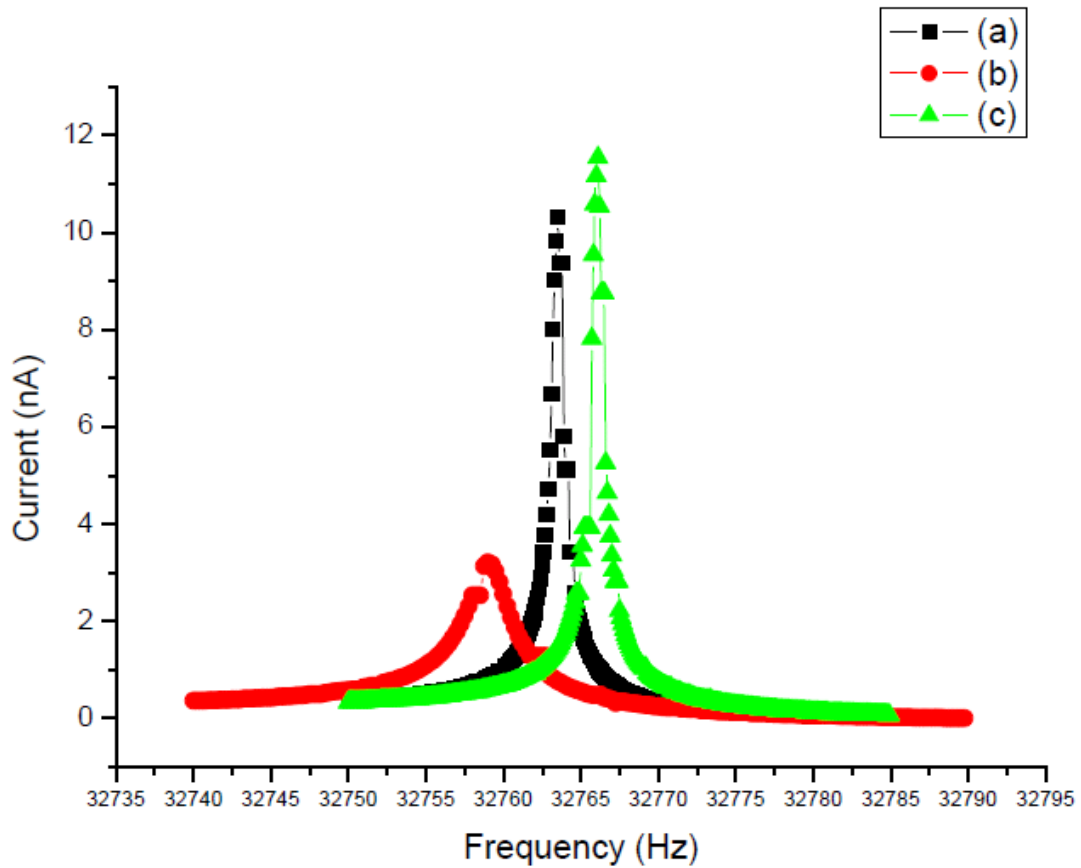


Figure 10. Induced current against driving frequency for QTFs (a) sealed hermetically, (b) vacuum cylinder removed, and (c) in the microscope vacuum chamber. Quality factor and resonance frequency are reduced in ambient conditions, but restored in the vacuum chamber at 10⁻⁵ mbar.

3.5.4. Tip production and arrangement

Producing sharp tips is fundamental in any mode of SPM. The diameter of the tip apex is the key factor in achieving high resolution imaging in AFM. For kelvin probe microscopy it is also necessary for the tip to be produced from a conducting material.

Wire tips are most commonly used for QTF tips. Because the additional mass of the tip causes a reduction in quality factor of the tuning fork it is important that the wire is of as small a diameter as possible, typically $<50\mu\text{m}$. Due to the low stiffness of thin wire it is difficult to produce sharp tips by cutting at an angle; a process commonly used to produce high quality scanning tunneling microscopy (STM) tips. Electrochemical etching is therefore a superior method of producing sharp tips reliably for QTF sensors. *Melmed et al*[42] offer a good overview of the various electrochemical etching techniques that can be employed to produce sharp tips of varying geometries, *Nam et al*[43] focus on the etching techniques that produce the highest quality tips for a range of materials.

Tungsten and platinum/iridium are the two most common materials used for electrochemical etching of sharp tips. Each has its advantages and disadvantages. For tungsten the etching process is dominant at the metal/electrolyte interface, so that a sharp tip can be produced by simply immersing the wire into the etching solution and applying a potential difference between them. As the diameter of the wire is reduced the meniscus of the electrolyte withdraws until a sharp tip is formed at the metal/electrolyte boundary. At this point the connection between the wire and the etching solution is broken and no further etching can occur. For Pt/Ir the etching process occurs over the entire surface of the wire, which has two drawbacks. First, the point at which the tip is formed will probably be located somewhere within the etching solution and over-etching can occur; blunting the tip unless the potential difference between tip and solution is quickly reduced. Secondly, this etching process can lead to a long, extremely thin tip with a low stiffness, a condition that isn't favourable for AFM imaging.

Despite producing higher quality tips more reliably, tungsten tips become coated with an oxide layer with a thickness of roughly 10nm [19], a property that is detrimental to its use as a probe in kelvin probe microscopy. For this reason it is Pt/Ir 90/10 wire that we use to produce tips for the QTFs. The diameter of the wire is 25 μ m.

The first stage of the tip preparation is removal of the tuning fork from its vacuum cylinder. This can be performed by making incisions around the base of the cylinder parallel to the tuning fork tines. Once removed, the legs of the tuning fork are removed and replaced with thin insulated cable, long enough for connection to the electrodes on the tuning fork mount. As already discussed the tuning fork is then mounted in the stainless steel block, at an angle of 15 °.

4M CaCl₂ solution in water is used as the electrolyte for etching of the Pt/Ir wire. A small droplet of the solution is suspended in a tungsten ring which is used as one electrode, excess solution is removed with a clean tissue until the thickness of the droplet is decreased to be comparable to the wire diameter. This ensures that the etching process is confined to a very short length of the wire and therefore that the rigidity of the tip isn't compromised.

A short length of the wire is electrically connected to the other electrode and is mounted on a micrometer. The micrometer is adjusted so that a length of the wire protrudes from the underside of the electrolyte droplet. For best results a 4V DC voltage was applied to the tungsten electrode and the tip electrode was grounded, the voltage was terminated when the protruding wire dropped off from the underside of the electrolyte droplet, see Fig. 9 for a cartoon representation of the etching process. The tip was subsequently rinsed first in deionised water and then acetone. A scanning electron microscope (SEM) image of a tip produced via this method is shown in Fig. 10, with a typical tip diameter of less than 50nm.

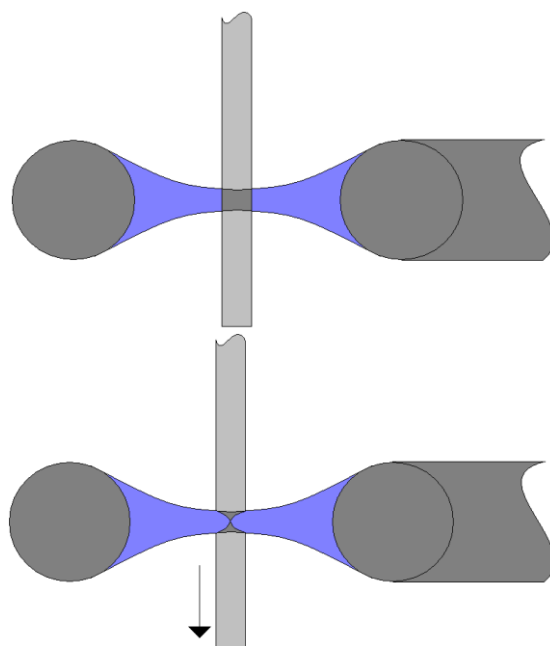


Figure 11. Cartoon representation of the tip etching process. A cross section of the ring shaped electrode is shown with the etching solution suspended inside. The wire tip passes through the etching solution. The upper image is prior to etching, the lower image is representative of the Pt/Ir tip just before completion of the etching process.

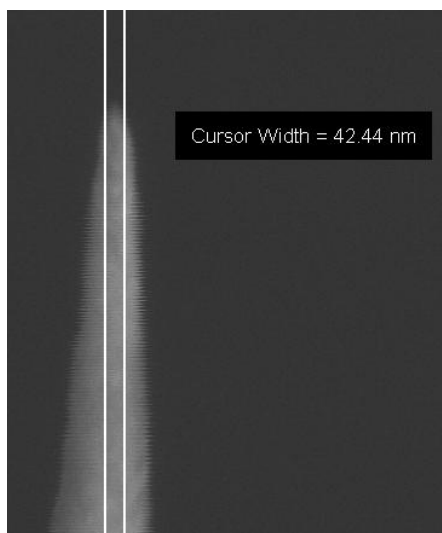


Figure 12. SEM image of a Pt/Ir 90/10 tip produced by electrochemical etching in CaCl_2 solution. The tips produced by this method typically have a diameter of $<50\text{nm}$.

An important consideration to be made when mounting the tip to the tuning fork is the protruding length of the tip. The spring constant of the tip should be larger than that of the tuning fork tines to ensure maximum damping of the tuning fork, Fig. 13 shows

the geometry of the tuning fork and tip. The static spring constant of a beam fixed at one end is given by[14]

$$k_{QTF} = \frac{\varepsilon_{QTF} W}{4} \left(\frac{T}{L} \right)^3 \quad (\text{Eq. 14})$$

where ε_{QTF} is Young's modulus ($7.87 \times 10^{10} \text{Nm}^{-2}$ for quartz), W , T and L are the width, thickness and length respectively, of the tuning fork tines, given above in Fig. 8. Equation 14 gives $k_{QTF} = 23.3 \times 10^3 \text{Nm}^{-1}$ for our tuning forks. For the case of a cylindrical probe fixed at one end, the static spring constant is given by

$$k_{tip} = \frac{3\pi\varepsilon_{tip} r^4}{l^3} \quad (\text{Eq. 15})$$

where $\varepsilon_{tip} = 1.68 \times 10^{11} \text{Nm}^{-2}$ for platinum, r and l are the radius and protruding length of the tip respectively. For the spring constant of the tip to be greater than that of the tuning fork the protruding length of the tip must be less than $120 \mu\text{m}$. The etched length of wire is cut to be about 1mm in length and a microscope is used to position it onto a droplet of conducting epoxy at the end of one tine of the tuning fork. A micromanipulator is used to alter the position of the tip so that the protruding length satisfies the conditions given in equations 14 and 15. The tip is then electrically connected to one set of the tuning fork electrodes for the electrostatic measurements. The epoxy is set by placing into an oven at 80°C for 90 minutes, after which any excess length of wire used for positioning of the tip is removed. The additional mass as a result of the tip and epoxy is $\sim 25 \mu\text{g}$.

Characteristics such as the resonance frequency and quality factor of tuning forks can be obtained by measuring the induced current in the tuning fork as the excitation frequency is varied. This measurement is shown in Fig. 14, from which the resonance frequency was found to have dropped by $\sim 500 \text{Hz}$, and the quality factor has dropped to ~ 8000 as a result of addition of a Pt/Ir tip using the method outlined above. These values were obtained by fitting the data using eq. 11 above. This trace is typical of a tuning fork fitted with a wire tip.

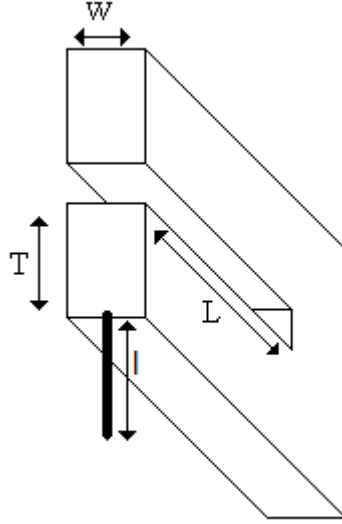


Figure 13. Cartoon representation of the tuning fork and tip geometry.

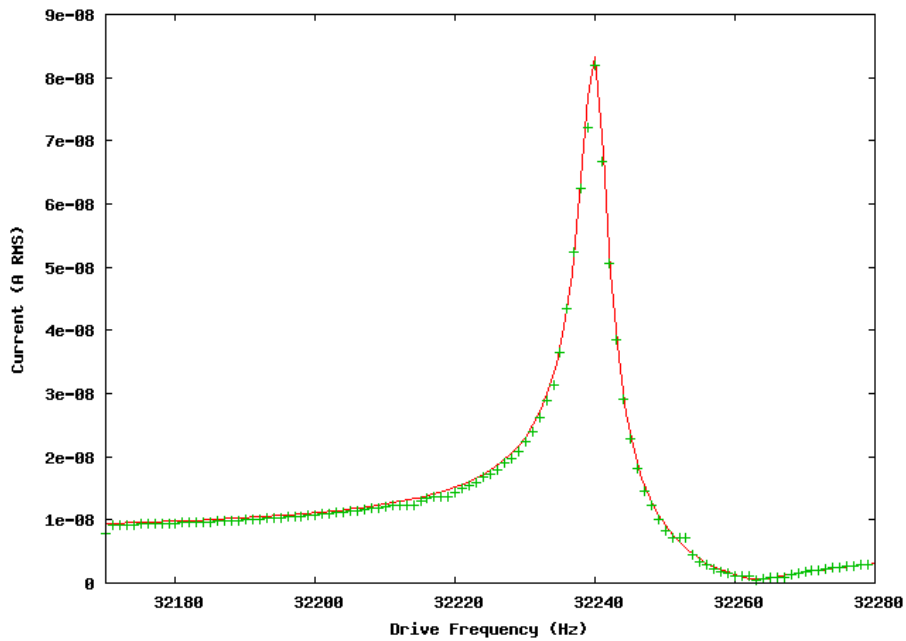


Figure 14. QTF current as the excitation frequency is varied. This tuning fork is mounted with a Pt/Ir of 25 μ m diameter. The tuning fork excitation voltage was 0.01V and these measurements were performed under a vacuum of 10^{-5} mbar. The resonance frequency has dropped by ~500 Hz and the sensor has a quality factor of ~8000.

A second method for preparing tipped tuning forks is to use traditional AFM cantilever tips [8-10]. The sharpness of these tips is far more reliable than those we have produced from electrochemical etching.

The cantilever is mounted on a comparatively large silicon wafer; typically 3mm in length and 1mm in width and depth. Adding this entire structure to the tuning fork depreciates the quality factor of the oscillator considerably, so it is advantageous to remove as much of this extra mass as possible prior to mounting. To achieve this a scalpel is used to carefully cut the wafer section of the cantilever. The brittle silicon wafer can be removed in relatively large sections, minimising the likelihood of damaging the tip or contaminating it with tiny fragments of the wafer. The remaining structure is rinsed in acetone before being attached to the tuning fork with epoxy.

Once cut, the silicon wafer is typically reduced to 10% of its initial volume; despite this it still has a greater mass than wire tips. In order to perform electrostatic measurements a thin film of chrome/gold can be evaporated onto the cantilever prior to mounting. This can then be electrically connected to one of the tuning fork electrodes with silver epoxy.

Figure 15 shows the induced current in the tuning fork as the excitation frequency is varied. This data was obtained and analysed in the same way as the Pt/Ir tip in Fig. 14 above. The addition of a cantilever tip causes a larger shift in resonance frequency of the QTF, typically by 1-2KHz. The quality factor of these sensors is also less than the wire type, 5-7000 typically.

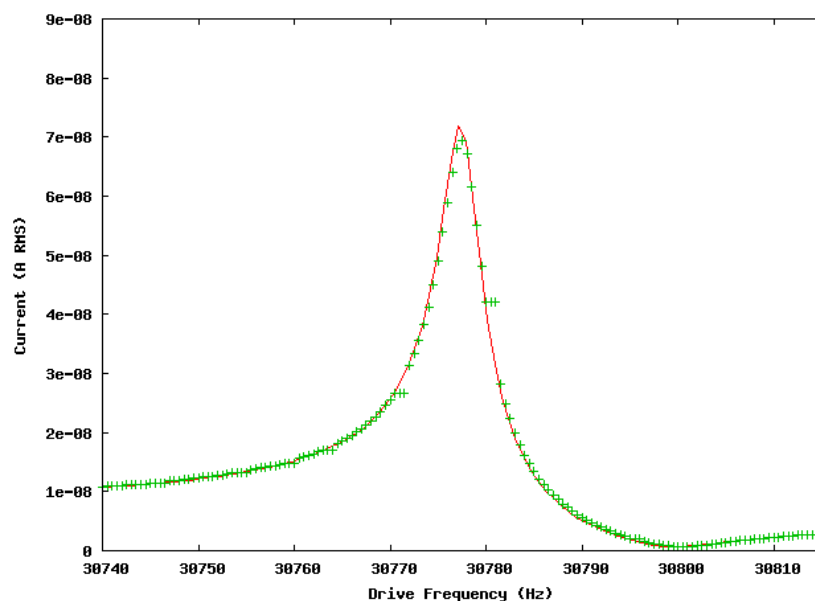


Figure 15. Induced current of a QTF as the excitation frequency is varied. This tuning fork is mounted with a reduced AFM cantilever tip. The tuning fork excitation voltage was 0.01V and these measurements were performed under a vacuum of 10^{-5} mbar. The resonance frequency has dropped by ~2KHz and the sensor has a quality factor of ~7000.

3.6. AFM control

3.6.1. Overview of the AFM system

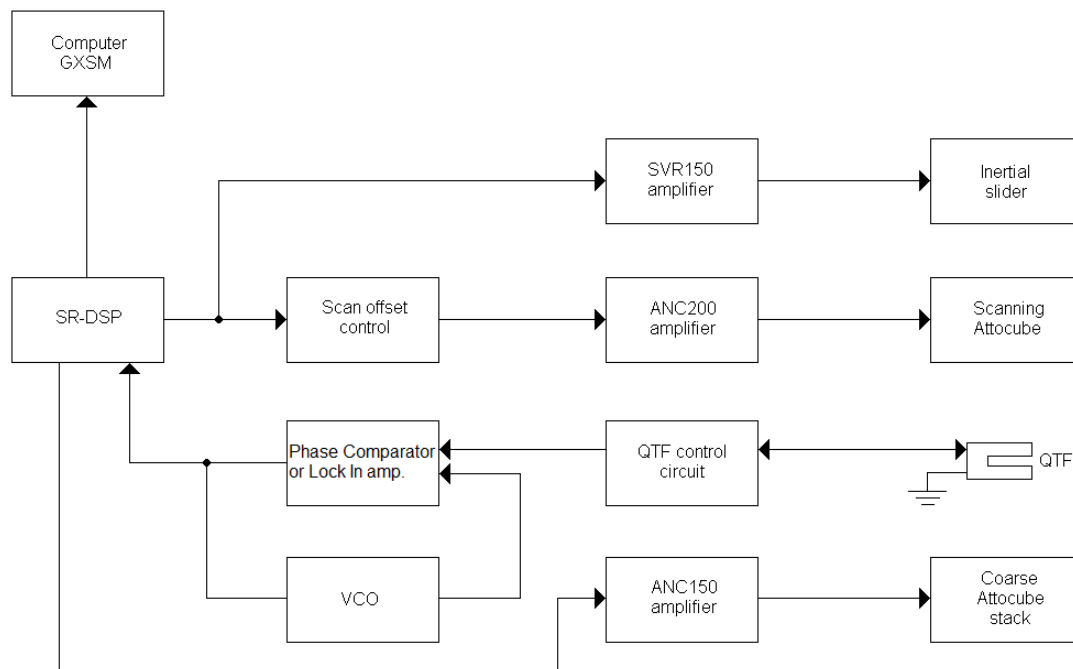


Figure 16. Block diagram of the AFM system and electronics.

A block diagram of the AFM system is shown in Fig. 16. The system is comprised of several different elements, these are the SPM software and DSP board, the phase locked loop (PLL), the QTF control circuit and the piezo/piezo-amplifiers discussed previously in 1.4.1-2. This section is concerned with explanation of these elements of the microscope and operation of the microscope in the AFM mode.

3.6.2. The GXSM software and DSP

The GXSM project[44] provides a modern and flexible SPM control with data analysis software. The GXSM software is released under the GNU general public

license and is available freely via the internet. The software is independent of any specialised hardware and is therefore ideal for operation of home-made microscopes and since the source code is available as open source, extension of the software by users is fairly simple. GXSM is designed to be a general purpose 1-3 dimensional acquisition and visualisation system. Variation of scan parameters such as scan speed, bias voltage and feedback parameters can be performed whilst scanning.

In addition to the software the GXSM project offers a high quality and inexpensive digital signal processor (DSP) for feedback control and scanning. The 16-bit Signal Ranger (SR) DSP is shown with recommended connections in Fig. 12 (taken from the GXSM manual). The SR-DSP features 8 sets of analogue to digital and digital to analogue converters (ADC & DAC). Six of the DAC outputs are used for scanning and offsets in all three dimensions, one for supplying a bias voltage for either STM or Kelvin probe applications, and the last is used to output ramped voltage waveforms generated by the DSP for control of the inertial slider piezo. A range of waveforms are available, controlled from the GXSM software which also allows for custom waveforms to be generated.

One DAC input is used for the feedback mechanism, typically a voltage proportional to the frequency shift experienced by the tuning fork. This leaves seven “free” inputs that can be used for additional data acquisition.

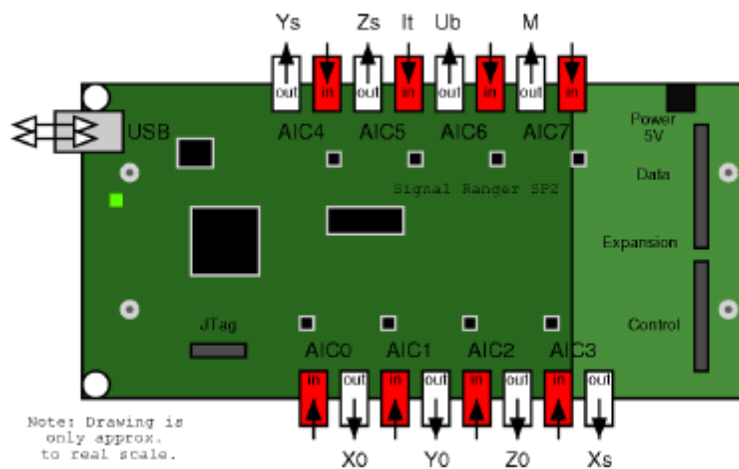


Figure 17. Signal Ranger DSP board with recommended connections. XYZ_s and XYZ_0 are the analogue scanning and offset voltages respectively. I_t is the analogue input for

the feedback loop, typically a voltage proportional to either tunnelling current (STM mode) or frequency shift (AFM) mode. U is the bias voltage for STM or Kelvin probe applications, and M is the motor output for DSP generated voltage ramps. The DSP interfaces with the GXSM software via a USB connection with the computer.

An expansion board is also commercially available for the SR-DSP providing it with two 16-bit input parallel ports, one 16-bit latched input parallel port, 2 16-bit and one 9-bit output parallel ports. The output from these pins can be controlled via the GXSM software and is used to trigger the ANC150 (coarse piezo amplifier).

3.6.3. Tuning fork control circuit

In frequency modulation (FM) AFM the tuning fork is driven at constant oscillation amplitude at the resonant frequency of the tuning fork. The resonant frequency of the tuning fork is given by

$$f_0 = \frac{1}{2\pi} \sqrt{\frac{k + \Delta k}{m}} \quad (\text{Eq. 16})$$

where k is the static spring constant of the tuning fork, m is the mass of one tine of the tuning fork, and Δk is the additional spring constant due to interaction of the tip with the sample surface, it is the derivative of the force with respect to distance, $\Delta k = dF/dz$. The tuning fork control circuit is responsible for maintaining these conditions.

An interface circuit for the QTF is used based upon a design by *Jersch et al*[45]. The circuit is small, cheap and highly sensitive to amplitude and frequency measurements. A schematic of the circuit used is shown in Fig. 18. The circuit also includes compensation for the parasitic capacitance of connecting leads and has high temperature stability.

The tuning fork is part of a self excited Barkhausen loop with an automatic gain control (AGC) that maintains constant oscillation amplitude of the tuning fork. Changes in the AGC voltage represent the dissipation changes of the QTF, this is one

of the measurable quantities/outputs of the circuit. This loop is part of the bridge oscillator circuit in Fig. 18 that maintains oscillation at the resonant frequency of the tuning fork. The other output from the circuit is the amplified sinusoidal signal of the tuning fork its self, with amplitude proportional to the oscillation amplitude of the QTF and frequency equal to that of the QTF. It is this signal that is used in the AFM feedback loop.

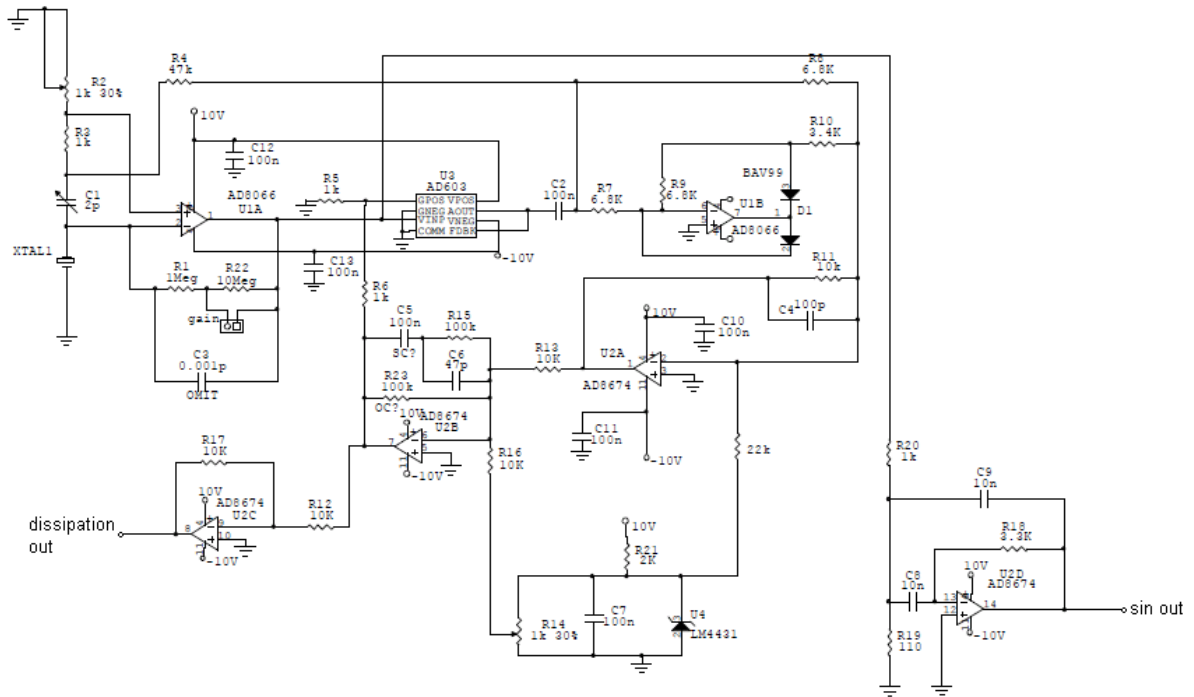


Figure 18. Schematic of the bridge oscillator circuit controlling the QTF. Compensation of the parasitic capacitance is achieved through the variable components R2 and C1, The oscillation amplitude is controlled by varying the AGC demand via variable resistor R14. The two outputs of the circuit are the amplified sin signal of the AGC voltage changes (dissipation signal).

Figures 19 and 20 show the Tuning fork control circuit and the typical output oscillation magnitude as a function of the control potentiometer settings. The three potentiometers are labelled A, B and C. Pot A controls the gain of the circuit (resistor R14 in Fig. 18.), pots B and C compensate for the parasitic capacitance of the tuning fork cables (R2 and C1 in Fig. 18 respectively). For the most stable behaviour Pot C should be adjusted so that the tuning fork oscillates with the minimum amplitude possible and pot B should be set between 45-90°. The tuning fork oscillation

amplitude can then be controlled by varying pot A, which varies the gain of the circuit.

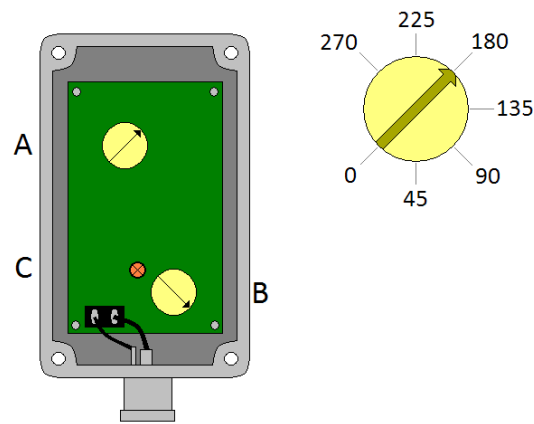


Figure 19. Cartoon image of the tuning fork control circuit with the BNC connector at the bottom of the device. The three control potentiometers are labelled A, B and C. Pot A controls the gain of the circuit (resistor R14 in Fig. 13.), pots B and C compensate for the parasitic capacitance of the tuning fork cables (R2 and C1 in Fig. 13 respectively).

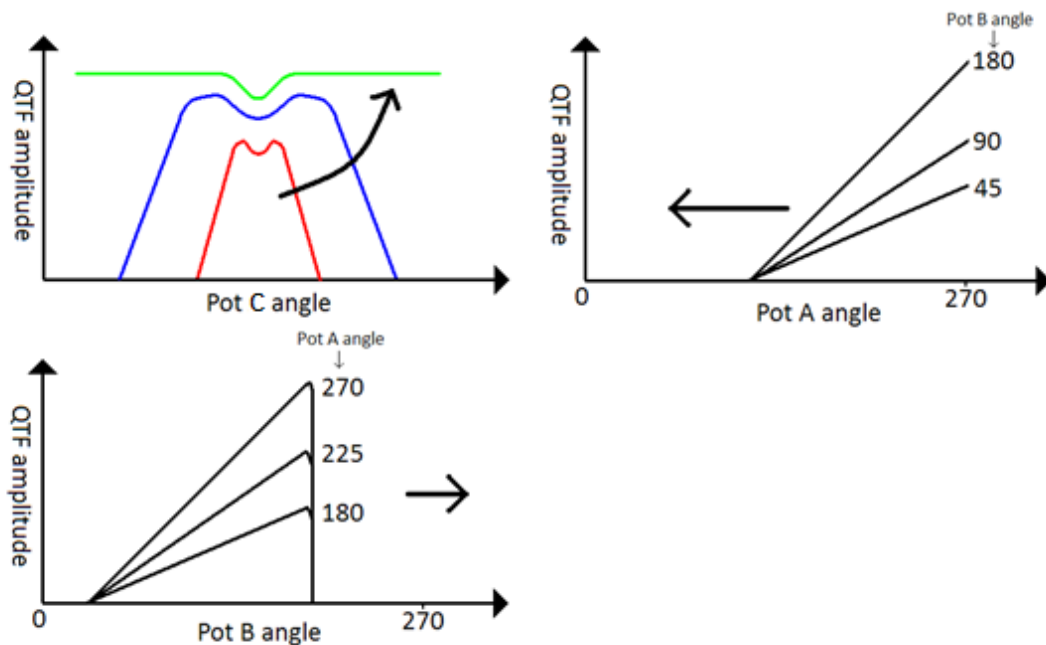


Figure 20. Cartoon graphs showing the typical behaviour of a tuning fork as a result of changing the pot positions. The angles used in these graphs correspond to the pot angle shown in the inset of Fig. 1. The upper left graph shows the effect of varying pot C (which can rotate continuously through 360°). The upper right image shows the effect of

Varying pot A for different fixed settings of pot B. The lower left image shows the effect of varying pot B for different fixed settings of pot A. The arrows represent the change in characteristics as a result of using a tuning fork with increased quality factor.

Calibration of the QTF oscillation amplitude can be performed in several ways [46, 47]. *Liu et al*'s method doesn't involve the use of interferometry but does require that the drive voltage of the tuning fork to be known accurately. In our QTF control circuit the drive voltage cannot be determined because the measurement process adds a relatively large capacitance across the terminals of the tuning fork that inhibit oscillation. For our calibration process we use a different method that is quick and simple but ultimately leads to a less accurate calibration, particularly for very small oscillation amplitudes.

First the QTF control circuit is set so that the tuning fork is oscillating and the output of the tuning fork control circuit; a sinusoid with amplitude proportional to the motion of the QTF, is being monitored. Next the tuning fork is brought into feedback by approaching a sample surface; the piezo position in the feedback direction is monitored by the GXSM software. Thermal drift in this direction is <15pm/second. The tip is withdrawn and the oscillation amplitude is reduced by some amount, feedback is reengaged and the new feedback position is found. The difference in feedback position is then equal to the change in oscillation amplitude for the given change in amplified oscillation voltage. By repeating this process numerous times a calibration value can be determined, assuming that the thermal noise of the QTF is small in comparison to the voltage induced oscillation.

Figure 21 shows the results of this calibration method. The change in piezo position varies linearly with the change in the QTF control circuit output voltage. As expected the oscillation amplitude with zero output voltage from the QTF control circuit is close to zero (1nm). As a result of these two findings, two considerations are made in determining the QTF oscillation amplitude. First, that the *change* in the QTF control circuit output voltage in Fig. 14 can be considered to be the QTF control circuit output voltage for the purposes of determining the oscillation amplitude. Second, that the change in piezo position in Fig. 14 can be considered to be equal to the tuning fork oscillation amplitude for the purposes of determining the oscillation amplitude. For

example, if a quartz tuning fork oscillates so that the QTF control circuit output is 2V, the oscillation amplitude is the same as the difference in piezo position for a QTF whose QTF control circuit output has been changed by 2V. The result of this is a ratio between the QTF control circuit output and the oscillation amplitude of the tuning fork. For typical operating conditions of the microscope – a QTF with a tip attached and a vacuum of 10^{-5} mbar, the oscillation amplitude is $\approx 30\text{nmV}^{-1}$, where the voltage refers to the QTF control circuit output.

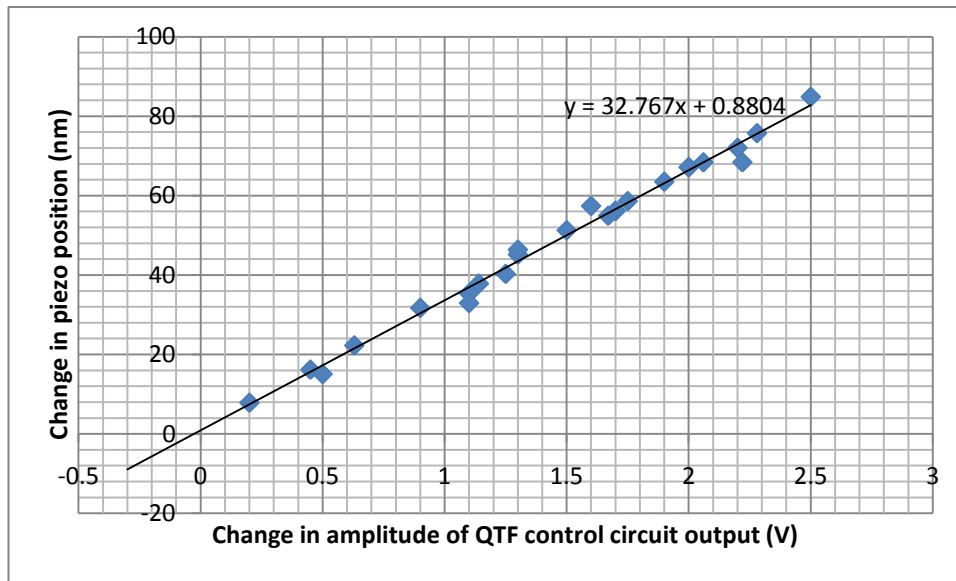


Figure 21 Calibration graph to find the tuning fork oscillation amplitude for a given QTF control circuit output voltage. The x-axis can be considered to be the QTF control circuit output voltage, and the y-axis can be considered to be the tuning fork oscillation amplitude. The QTF oscillation amplitude is $\approx 30\text{nmV}^{-1}$, where the voltage refers to the QTF control circuit output.

3.6.4. The phase locked loop

A phase locked loop (PLL) adjusts the frequency and phase of a voltage controlled oscillator (VCO) so that they match that of a reference oscillator, which in this case is the QTF. The output from the PLL is a DC voltage proportional to the frequency shift experienced by the tuning fork.

Two different phase locked loop (PLL) arrangements are possible for the quartz tuning fork (QTF) based AFM system. Schematic diagrams of these are shown in

Fig. 22. The signal to noise ratio and the response times of the two PLLs are used to determine which is most suitable for the AFM system.

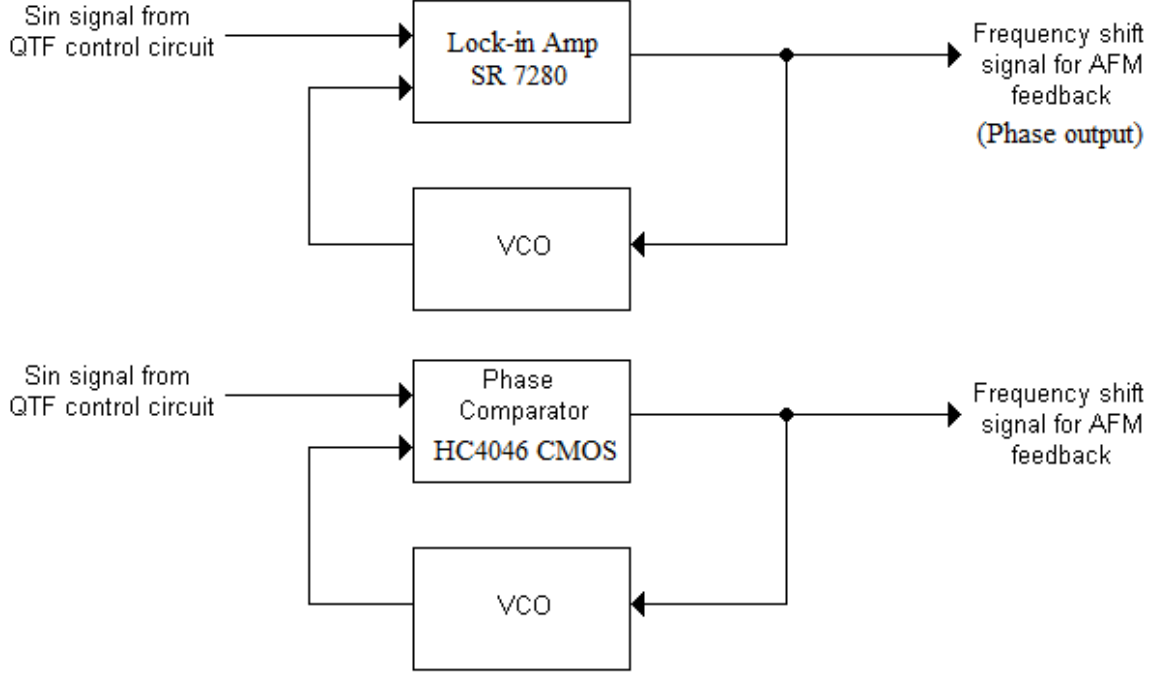


Figure 22. Alternative arrangements for the phase locked loop. In the upper arrangement a lock-in amplifier is used to determine the QTF frequency shift. In the lower arrangement a digital phase comparator is used to determine the QTF frequency shift.

The QTF control circuit drives the tuning fork at its resonant frequency and outputs a sinusoidal voltage at this frequency with amplitude proportional to that of the tuning fork. First to be considered is the characteristics of the lock-in based PLL [48].

The output of the tuning fork drive circuit is a sinusoid with frequency ω_{TF} , amplitude A_{TF} (proportional to the QTF oscillation amplitude) and phase φ_{TF} . The other input to the Lock-in amplifier is the reference signal from the VCO, with frequency ω_r , amplitude A_r and phase φ_r :

$$x_{TF}(t) = A_{TF} \sin(\omega_{TF}t + \varphi_{TF}(t)) \quad (\text{Eq. 17})$$

$$x_r(t) = A_r \cos(\omega_r t + \varphi_r(t)) \quad (\text{Eq. 18})$$

the lock-in amplifier consists of a multiplier and a low pass filter, the output of the multiplier is given by $x_o(t)$:

$$x_o(t) = x_{TF}(t)x_r(t) \quad (\text{Eq. 19})$$

$$x_o(t) = K_m A_{TF} A_r \sin(\omega_{TF}t + \varphi_{TF}(t)) \cos(\omega_r t + \varphi_r(t)) \quad (\text{Eq. 20})$$

$$x_o(t) = \frac{K_m A_{TF} A_r}{2} \sin[\varphi_{TF}(t) - \varphi_r(t)] + \frac{K_m A_{TF} A_r}{2} \sin[2\omega t + \varphi_{TF}(t) + \varphi_r(t)] \quad (\text{Eq. 21})$$

the frequency of the first term of eq. 21 is a function of only the phase difference between $x_{TF}(t)$ and $x_r(t)$. The frequency of the second term is twice that of the QTF; this part of the signal is removed by the low pass filter, leaving:

$$x_{LI}(t) = \frac{K_m A_{TF} A_r}{2} \sin[\varphi_{TF}(t) - \varphi_r(t)] \quad (\text{Eq. 22})$$

where $x_{LI}(t)$ is the output of the lock-in amplifier; it is the input to the VCO and also the feedback signal in the AFM system. The VCO produces a sinusoidal reference signal as given by eq. 18. Given that $x_{LI}(t)$ is zero, $x_r(t)$ will be at the VCO centre frequency ω_c . However, in the case that there is a phase difference between $x_{TF}(t)$ and $x_r(t)$ then $x_{LI}(t)$ is non-zero, and this error signal varies the VCO output frequency in an attempt to match the new phase of the tuning fork.

The output frequency of the VCO is given in eq. 23 below:

$$\omega_r(t) = \omega_c + K_0 x_{LI}(t) \quad (\text{Eq. 23})$$

where ω_c is the VCO centre frequency and K_0 is the sensitivity of the VCO; a ratio of the change in output frequency for a given input voltage, having units of HzV^{-1} . The phase of the VCO output signal, $\varphi_r(t)$, is obtained by integrating its frequency over a period of time:

$$\varphi_r(t) = \int_0^t \omega_r(t) dt \quad (\text{Eq. 24})$$

$$\varphi_r(t) = 2\pi K_0 \int_t^t x_{LI}(t) dt \quad (\text{Eq. 25})$$

$$\varphi_r(t) = 2\pi K_0 x_{LI}(t) t \quad (\text{Eq. 26})$$

given that the error signal $x_{LI}(t)$ is non-zero, it can be seen from eq. 26 that the VCO output phase will adjust until $x_{LI}(t)$ is reduced to zero. It is through this process that the feedback loop is locked. Substitution of eq. 26 into eq. 22 yields the PLL equation:

$$x_{LI}(t) = \frac{K_m A_{TF} A_r}{2} \sin[\varphi_{TF}(t) - 2\pi K_0 X_{LI}(t) t] \quad (\text{Eq. 27})$$

$$x_{LI}(t) = \frac{K_m A_{TF} A_r}{2} [\varphi_{TF}(t) - 2\pi K_0 X_{LI}(t) t] \quad (\text{Eq. 28})$$

Eq. 28 is based on the assumption that $\sin \theta \approx \theta$ for small values of θ . $X_{LI}(t)$ is the amplitude of $x_{LI}(t)$ at t .

The second arrangement for the feedback loop relies on a phase comparator (PC) chip; an HC4046 CMOS. One input to this PC is the QTF sinusoid signal, which is converted to a square waveform. The reference signal is a square waveform from the VCO. The phase comparator is triggered at rising step edges of either the QTF or VCO signal, forcing the PLL into lock with 0 phase difference between the VCO output and the QTF positive waveform edges.

Figure 23 shows some typical PLL waveforms. Consider first that the QTF signal leads the VCO signal; the frequency of the VCO must be increased to bring the rising edge of the VCO signal into phase alignment with the QTF signal. The PC output is set high between the rising step edges of the QTF and VCO signals, this charges the VCO input causing the output frequency to increase. If subsequently the QTF signal lags behind the VCO signal the PC output is set low between the rising step edges, discharging the VCO input signal and reducing the VCO output frequency to bring

the phase difference between the two signals to zero. The VCO input signal is a direct measure of the frequency shift experienced by the QTF and is the feedback signal used in the AFM system.

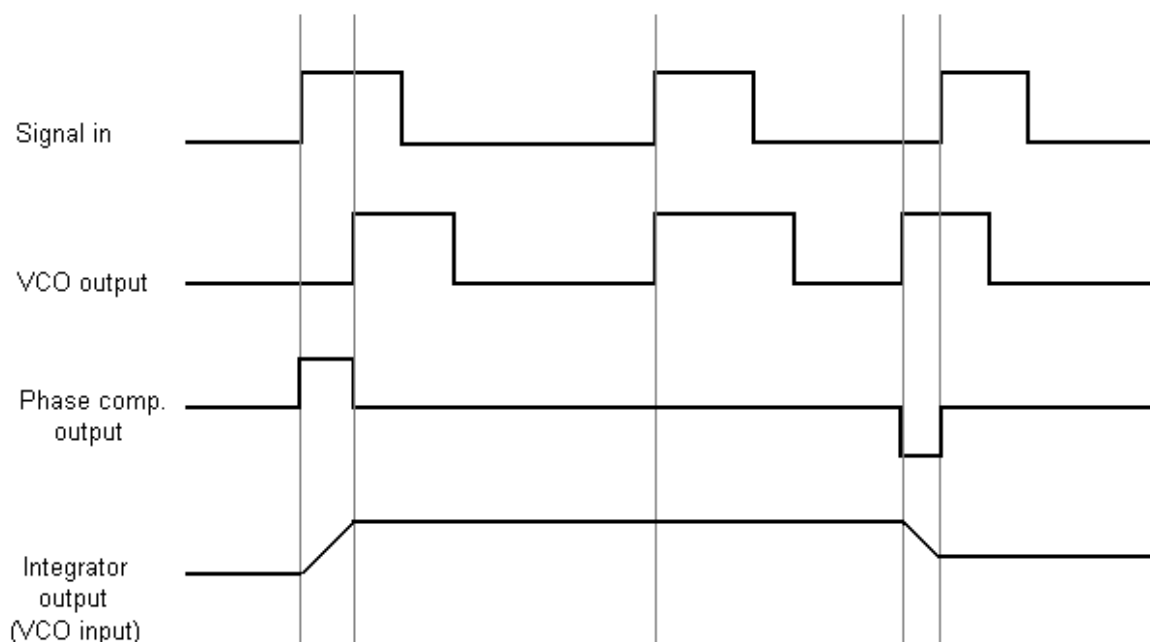


Figure 23. Typical input/output operations of the HC4046 CMOS phase comparator. The input signals are compared at leading edges and the phase comparator output is non-zero between leading edges. The phase comparator output is integrated and used as both the VCO input and the AFM feedback signal.

Another important factor in determining the ability of each PLL is the noise in the frequency shift signal. For this FFTs were performed on the frequency shift signal from both PLLs. Both FFTs were performed in identical conditions; a vacuum of roughly 10^{-4} mbar, with the same tuning fork having a quality factor of about 1.5×10^4 . One set of data was obtained with a tuning fork oscillation amplitude of roughly 80nm, the other with an amplitude of roughly 5nm. For these measurements the tuning fork was not in contact with the surface. The FFTs were constructed from the average of 10 sets of data, each with an acquisition rate of 5000Hz. Figure 24 shows a comparison of the noise spectrums obtained in this way. For large tuning fork oscillation amplitudes there is little difference between the two PLL arrangements, however, at lower tuning fork amplitudes there is considerably less noise whilst operating with the lock-in PLL. For this reason the lock-in based PLL is used in preference of the phase comparator alternative.

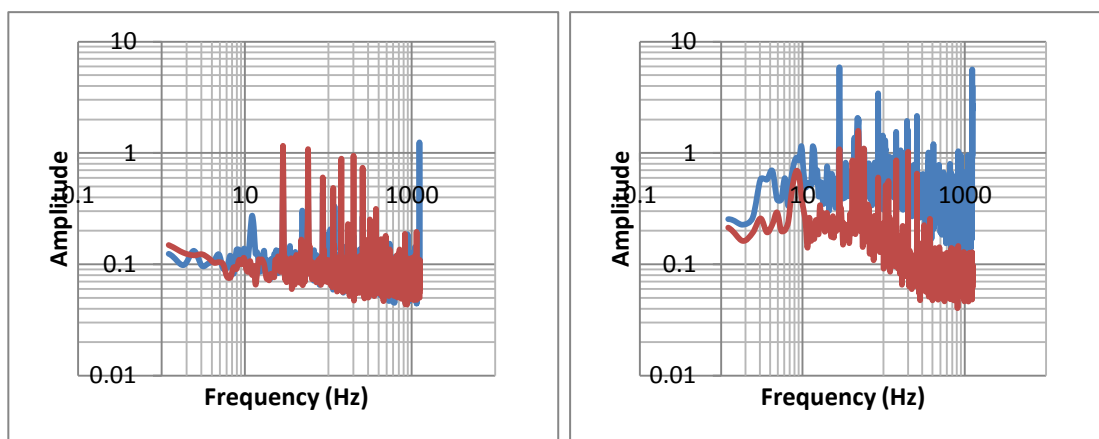


Figure 24. Comparisons of the noise spectrum of the frequency shift signal from both of the PLL arrangements. Data obtained with the lock-in configuration is shown in red, data obtained with the phase comparator configuration is shown in blue. The image on the left is obtained with a large tuning fork amplitude of roughly 80nm; the image on the right is with a tuning fork amplitude of roughly 5nm. With a small oscillation amplitude the noise is noticeably less with the lock-in PLL arrangement.

3.6.5. Imaging

This section contains images obtained with the AFM part of our homebuilt microscope, compared with images of the same samples obtained on a commercially available Digital Instruments (DI) AFM.

Figure 25A+B are images of P3HT; a polythiophene. P3HT forms nanowire structures when spun cast in toluene. Figures 25a+b are 10 micron images obtained on our homebuilt microscope. The scan speed for these images was 0.5Hz, with a Pt/Ir wire tip and oscillation amplitude of roughly 50nm. Figure 25c was obtained on the DI AFM, showing a similar topography to that obtained with the homebuilt system.

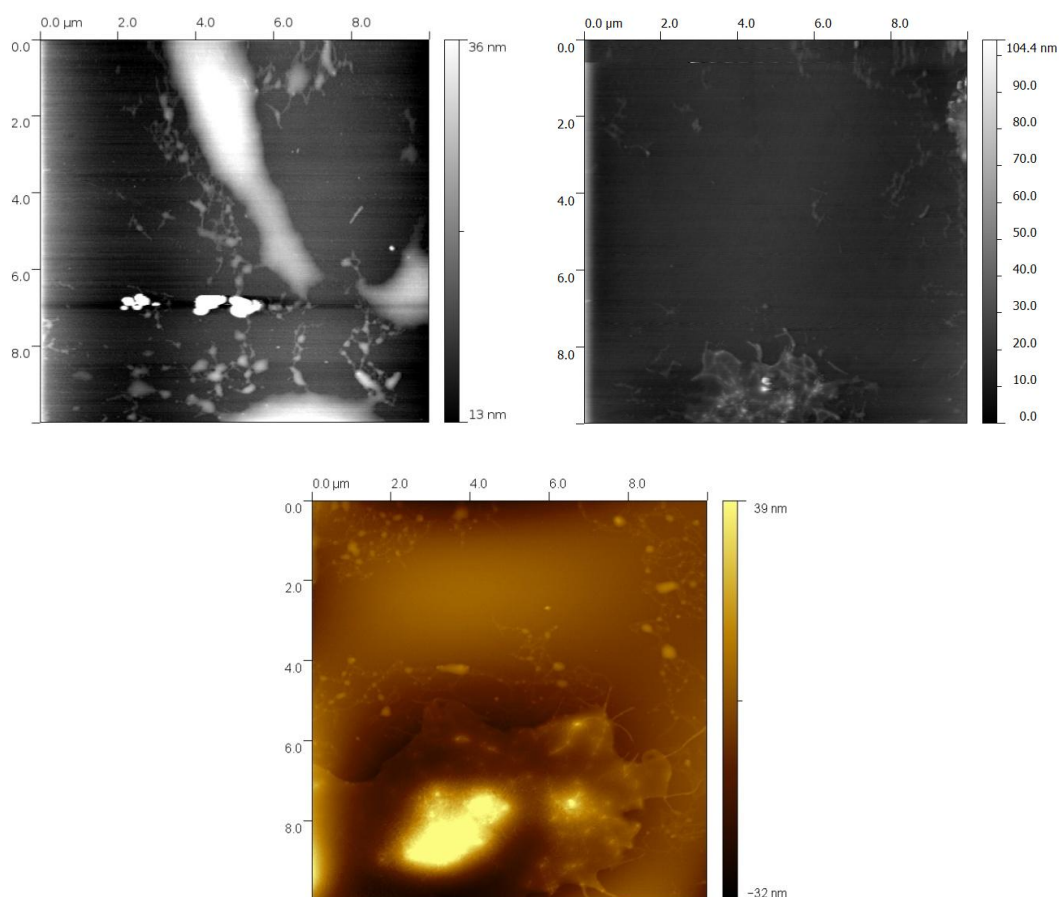


Figure 25. A+B) upper images, obtained on our homebuilt system, and C) obtained on the DI AFM. Both microscopes show similar topography in these 10μm scans.

If left for several days in a vacuum oven the P3HT structure changes significantly from that observed in Fig. 1. A thin film of P3HT nanowires are shown in Fig. 26. The upper image was obtained on the DI AFM, a cross section showing the height of the wires is to the right of this image. The lower set of images in Fig. 26 is the corresponding data obtained on the home built AFM system, also with a Pt/Ir wire tip. The height of nanowires observed by both systems is found to be 3-5nm.

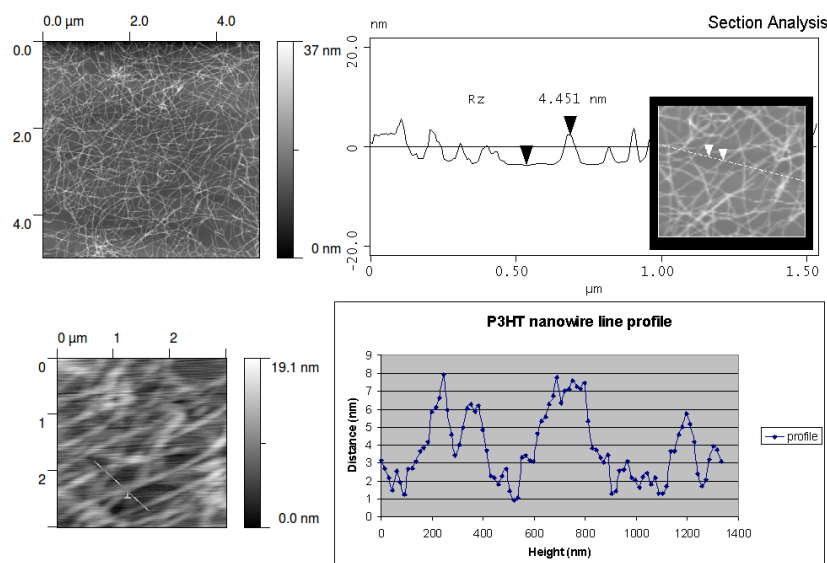


Figure 26. Upper image is of P3HT nanowires obtained on the DI AFM, the line profile of these wires is shown to the right of the scan. The lower image is obtained on our homebuilt AFM, the corresponding cross section also shows the nanowires to have a height of 3-5nm.

An aperture sample has been used to test the calibration of the piezos on the homebuilt AFM. The sample consists of a silicon wafer substrate with a thin platinum layer evaporated onto its surface. A final evaporation of gold in a grid pattern was then evaporated onto the platinum layer. The gold layer is 50nm thick, with 5μm square apertures. The upper image and line profile of Fig. 27 were obtained on the DI AFM, the lower image and line profile were obtained on the homebuilt system with an acquisition rate of 1 line per second. A cantilever tip was used to obtain this image. Both microscopes obtain the same aperture depth of roughly 50nm, and area 5μm by 5μm.

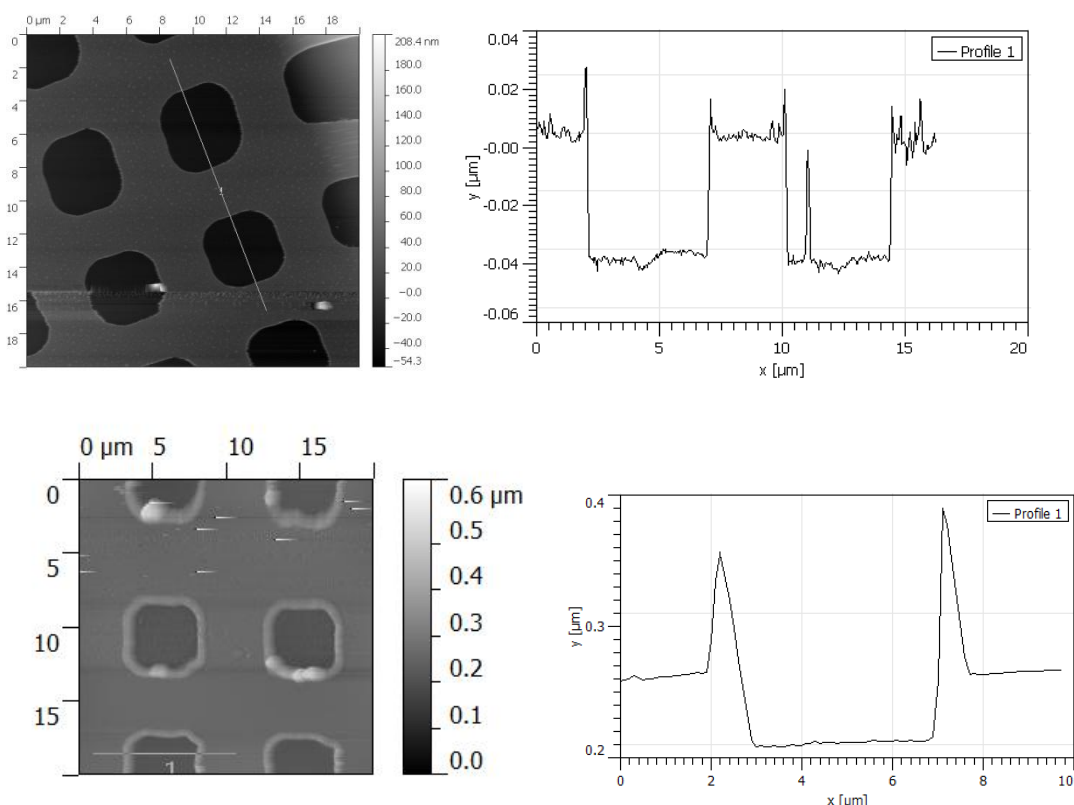


Figure 27. 20 μm area scans of gold apertures on thin platinum film on a silicon substrate. The upper images are obtained on the DI AFM, the lower set of images were obtained on our homebuilt AFM. Both microscopes observe very similar aperture dimensions, as shown in the cross sections given to the right of the images.

The quantum dot samples in Fig. 28 and 29 are both spun cast in the same way, but on different substrates. The quantum dots are commercially available CdSe/ZnS dots. 1mg of these dots in powder format are added to 50 μl of toluene and left in an ultrasonic bath for 15 minutes. The resulting mixture is relatively concentrated and has a bright orange colour. 5 μl of this concentrated solution is added to a further 50 μl of toluene and again the solution is placed in an ultrasonic bath for a further 15 minutes. 5 μl of this final solution is spun cast onto the substrate at 2000rpm for 30 seconds.

The two substrates used in the scans of Fig. 28 and 29 are silicon and glass respectively. For the silicon substrate, commercially available wafers are used. For glass substrates glass cover slips are used (Fisher Scientific, 24x24mm, 0.5mm thickness). Once the silicon wafer is cut to the correct size, both substrates are cleaned in the same way prior to addition of the QD/toluene solution. First the

substrates are rinsed in acetone for 20 seconds and blown dry with a nitrogen gun, this process is then repeated before placing the substrates on a hot plate at 100°C for 15 minutes. The substrates are then removed and the rinsing process is repeated with IPA instead of acetone. The substrates are left on the hotplate at the same temperature for a further 30 minutes. Once cooled the QD/toluene solution is spun cast onto the substrate and the samples are left in a vacuum oven for 24 hours.

Figure 28 shows images of QDs on a silicon substrate, prepared by the method outlined above. The image and line profile on the left were obtained with the DI AFM, the image and line profile on the right were obtained on the homebuilt system. We have found that dots prepared on the silicon substrates have a tendency to form larger structures, which are either aggregates of QDs or formed from residual materials from the cleaning process or quantum dot solution. The larger scale striped patterns observed in both images are a characteristic of the silicon substrates we have used, and are present on silicon samples without QDs spun cast onto them. Whilst the height of these dots is similar in both images, typically about 5nm for what is thought to be single dots, the lateral size of the dots is considerably larger when measured on the homebuilt system. This is thought to be due to a degradation of the tip in the image obtained on our homebuilt AFM, a larger tip radius would account for the larger width but similar height of the dots between the two microscopes.

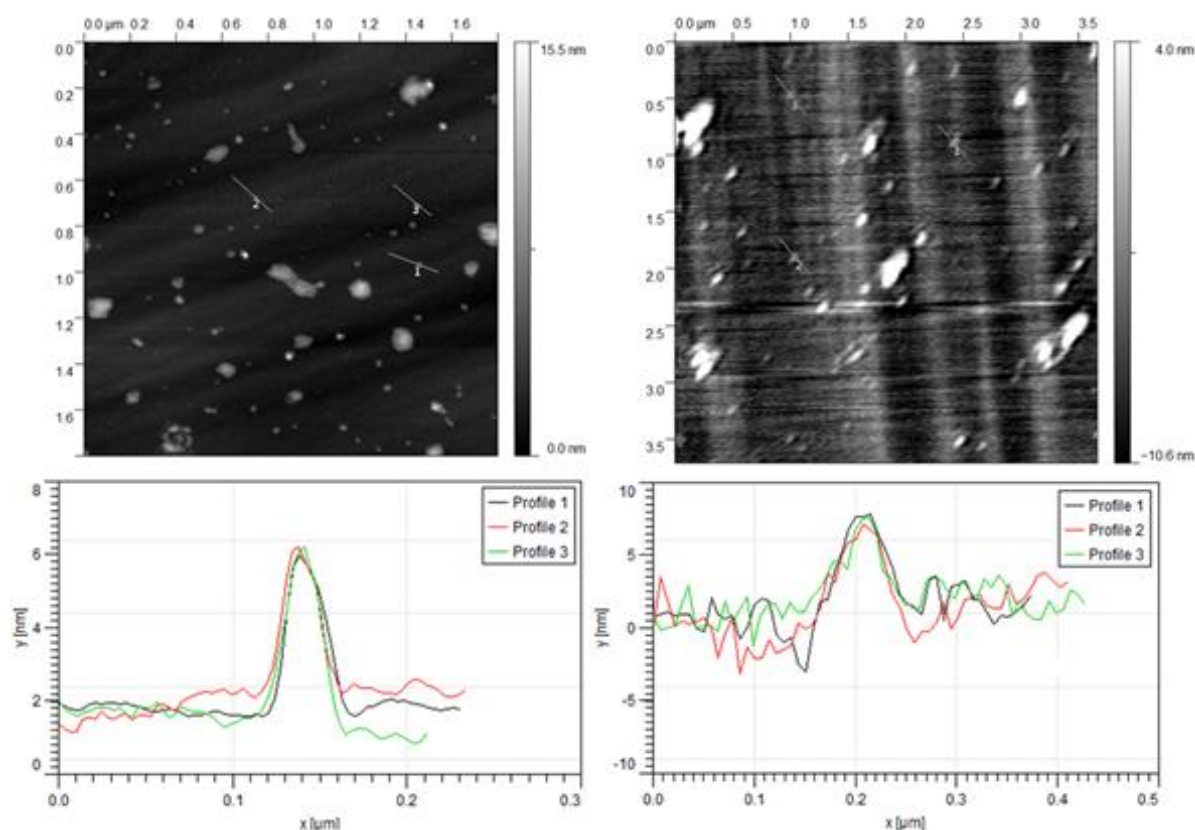


Figure 28. Images of CdSe/ZnS quantum dots obtained by the DI AFM (left) and the homebuilt AFM (right). Both microscopes observe a similar QD height, as can be seen in the line profiles below the images. The width of the dots is observed to be larger on our homebuilt system, probably due to a degraded tip with larger radius than that of the DI AFM scan.

The images in Fig. 29 were obtained from QD samples prepared on glass substrates. The bare glass substrates have also been imaged and have been found to have a roughness of only a few angstroms. When the QD/toluene solution is spun cast onto the glass cover slip it has been found that as well as the dots there are similarly sized perforations present on the sample surface. These perforations occur if toluene alone is spun cast onto the cover slips, and are also observed for a range of other organic solvents, such as hexane, p-xylene, o-xylene and trimethylbenzene. The origin of these perforations is unknown. They are of uniform size though, with a depth of roughly 1nm.

The advantage of these glass substrate samples is that they are optically transmissive, ideal for our application combining optical and scanning probe microscopy techniques.

As is the case for quantum dots on silicon substrates, the height of the dots is 4-5nm in data obtained by both the homebuilt AFM and the DI AFM. The width of dots as measured by the homebuilt AFM is again larger than that obtained with the DI AFM, again this is presumed to be due to a larger tip radius for the homebuilt system.

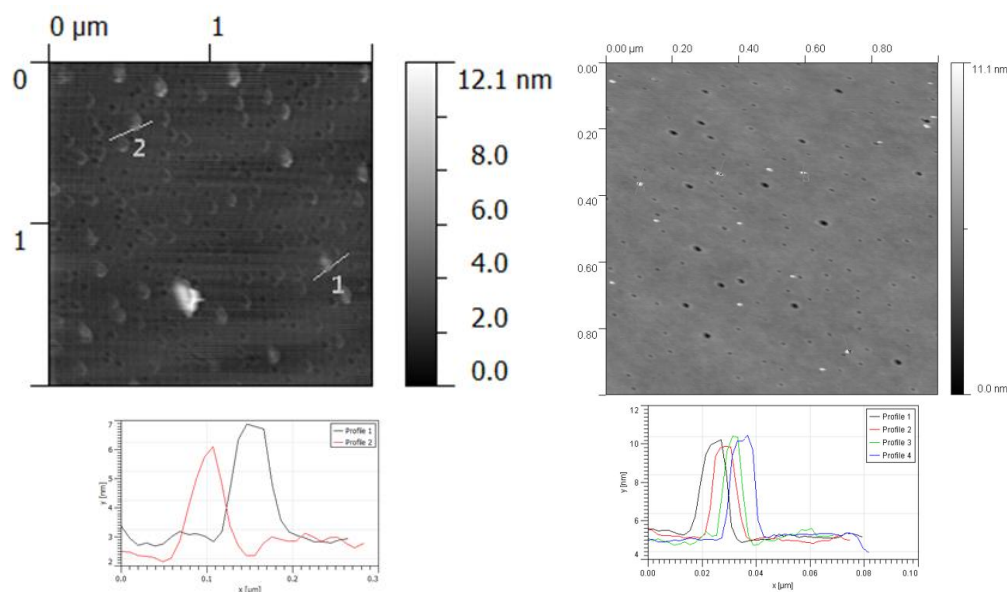


Figure 29. Images of CdSe/ZnS quantum dots obtained by the homebuilt AFM (left) and the DI AFM (right). Both microscopes observe a similar QD height, as can be seen in the line profiles below the images. The width of the dots is observed to be larger on our homebuilt system, probably due to a degraded tip with larger radius than that of the DI AFM scan. Perforations can also be seen in both images, a result of the organic solvent used in spin casting the QDS.

3.6.6. Aligning the optical and scanning probe parts of the microscope

This section outlines the process of aligning the optical and scanning probe microscopes on the same region of a sample. The sample substrate is a glass cover slip (Fisher Scientific) that are 24mm by 24mm in area and have a thickness of about 0.5mm.

The cover slip is mounted on the sample holder so that the sample is pointing towards the SPM section of the microscope. First the sample is brought into focus of the optical microscope by manual adjustment of the coarse Attocube stack. Next the home built stepper piezo is used to bring the tuning fork close to the sample surface, so that the tip/sample separation distance is less than 1mm. An LED is located behind the tuning fork; when the tip of the tuning fork is close to the region being observed by the optical microscope the shadow of the AFM tip can be seen in the optical image.

By observing the shadow of the cantilever, the coarse positioning devices can be used to bring the apex of the AFM tip to the correct region of the sample. Once the optical and AFM sections of the microscope are aligned the coarse positioning devices can be fixed in place with screws. The lid of the vacuum chamber can be replaced, and once a sufficient vacuum is achieved the home built stepper piezo is used to bring the AFM tip into contact with the surface for AFM scanning.

3.7. Optical Microscopy

Time-Correlated Single Photon Counting (TCSPC) is based on the detection of single photons of a periodical light signal, the measurement of the detection times of the individual photons and the reconstruction of the waveform from the individual time measurements. The method makes use of the fact that for low level, high repetition rate signals the light intensity is usually so low that the probability to detect one photon in one signal period is much less than one. Therefore, the detection of several photons can be neglected.

In our experiment we use a BDL-473-C laser that can provide high repetition rate and short pulse width (40 to 90ps) ideal for TCSPC applications.

The detector signal consists of a train of randomly distributed pulses due to the detection of the individual photons. There are many signal periods without photons, other signal periods contain one photon pulse. Periods with more than one photons are very rare. When a photon is detected, the time of the corresponding detector pulse

is measured. The events are collected in a memory by adding a '1' in a memory location with an address proportional to the detection time. After many photons, in the memory the histogram of the detection times, i.e. the waveform of the optical pulse builds up.

Although this principle looks complicated at first glance, it is very efficient and accurate for the following reasons; the accuracy of the time measurement is not limited by the width of the detector pulse. Thus, the time resolution is much better than with the same detector used in front of an oscilloscope or another analogue signal acquisition device. Furthermore, all detected photons contribute to the result of the measurement.

Depending on the desired accuracy, the light intensity must not be higher than to detect 0.1 to 0.01 photons per signal period. Modern laser light sources deliver pulses with repetition rates of 50 to 100MHz. For these light sources, the count rate constraint is satisfied even at count rates of several 10^6 photons per second. Such count rates already cause overload in many detectors. Consequently the intensity limitation of the single photon counting (SPC) method does not cause problems in conjunction with high repetition rate laser light sources.

The single-photon pulses from the photon detector are fed to the input photo multiplier tube (PMT). Due to the random gain mechanism in the detector these pulses have a considerable amplitude jitter. The constant fraction discriminator (CFD) has to deliver an output pulse that is correlated as exactly as possible with the temporal location of the detector pulse. This is achieved by triggering on the zero cross point of the sum of the input pulse and the delayed and inverted input pulse.

Since the temporal position of the crossover point is independent of the pulse amplitude, this timing method minimises the time jitter due to the amplitude jitter of the detector pulses. Furthermore, the CFD contains a window discriminator that rejects input pulses smaller than the discriminator threshold. The threshold or the amplitude window are adjusted to reject noise from the environment, noise from preamplifiers or small background pulses of the detector [49].

Figure 30 shows intensity versus time data for the same CdSe/ZnS quantum dot obtained via the method outlined above. The two traces were recorded with an interval of several minutes. The upper graph shows a period where the quantum dot resides primarily in the dark state, for the lower graph the quantum dot is primarily in the bright state.

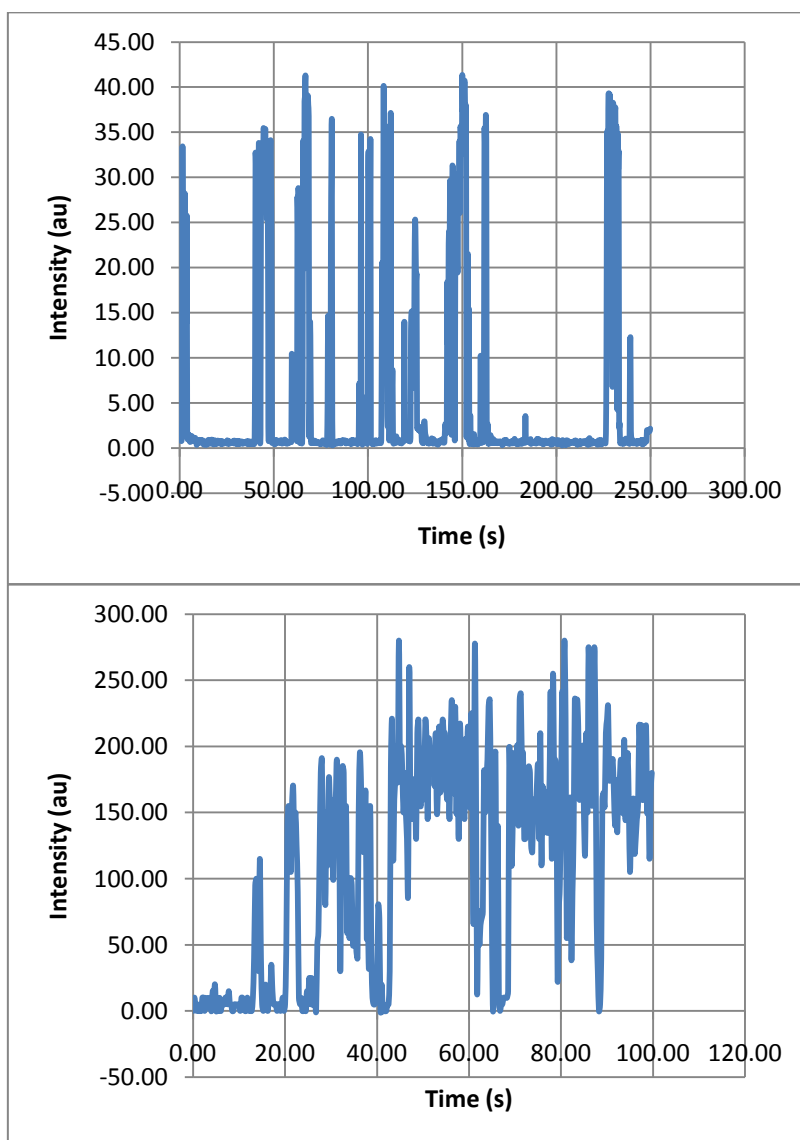


Figure 30. Optical output intensity of a quantum dot exhibiting photoluminescence intermittency over a 120 second period. The upper graph is for a period for which the quantum dot was primarily in the dark state. Data in the lower graph was obtained from the same quantum dot only several minutes later; during this time the quantum dot is mainly in the bright state.

3.8. Conclusion

In conclusion this chapter has discussed the design and operation of a microscope combining scanning probe and optical microscopy. The scanning probe part of the microscope utilises quartz tuning fork based sensors with tips produced by either electro chemical etching or reducing commercially available silicon cantilevers. Scanning electron microscopy has revealed that our electrochemically etched Pt/Ir tips have a tip diameter of less than 50nm, comparable or surpassing that recorded in literature. Both methods of tip production yield sensors with a quality factor of roughly 10^4 in high vacuum. The latter method, involving the reduction of silicon cantilevers is favourable to the electrochemical etching method for two reasons. First, the tips produced in this way are more reliable; the etching process can produce very sharp tips, but about 50% of the tips produced in this way have significantly larger tip diameters. Secondly, cantilever based sensors can be produced in only about 20 minutes, compared to roughly an hour for the electrochemically etched alternatives.

Homebuilt positioning devices have been developed to bring the optical and SPM parts of the microscope into alignment on the same region of the sample. The inertial slider; a larger version of a design by *Silveira et al*[39], allows for a travel distance of about 6mm, with a minimum movement of about 100nm with the scanning piezo and QTF sensor mounted on its underside. This combined with the spring loaded lateral positioning devices discussed in chapter 1.4.3. allow for easy alignment of both microscopy systems, a process requiring only about 15 minutes. Once this alignment is performed the lateral positioning devices can be locked in place for scanning.

Imaging in the AFM mode has been achieved on a variety of samples; HOPG, gold/platinum aperture grids, organic compounds and CdSe/ZnS quantum dots. Images obtained with the homebuilt system show a topography that is similar to that observed by a commercial AFM system scanning the same samples. However, the resolution of our homebuilt system is lower than that which would be required for measurements of the electronic properties of quantum dots. The system is deployed on a vibration isolation system within the vacuum chamber. This comprises of a spring based suspension stage with a resonant frequency of 2Hz, and a magnetic

damping system based on the findings of *Park et al*[38]. The microscope chamber is mounted on an air table. Despite this the system still exhibits a noise in the tip/sample distance of roughly 1nm, significantly more if there is movement in the vicinity of the system.

3.9. References

1. Binnig, G. and H. Rohrer, *Scanning tunneling microscopy*. Ceskoslovensky Casopis pro Fyziku, Sekce A|Ceskoslovensky Casopis pro Fyziku, Sekce A, 1986. **36**(3): p. 209-19.
2. Binnig, G.K., *Atomic-force microscopy*. Physica Scripta Volume T|Physica Scripta Volume T, 1987. **T19A**: p. 53-4.
3. Albrecht, T.R., et al., *Frequency modulation detection using high- Q cantilevers for enhanced force microscope sensitivity*. Journal of Applied Physics|Journal of Applied Physics, 1991. **69**(2): p. 668-73.
4. Nonnenmacher, M., M.P. Oboyle, and H.K. Wickramasinghe, *Kelvin Probe Force Microscopy*. Applied Physics Letters, 1991. **58**(25): p. 2921-2923.
5. Seo, Y., P. Cadden-Zimansky, and V. Chandrasekhar, *Low-temperature high-resolution magnetic force microscopy using a quartz tuning fork*. Applied Physics Letters, 2005. **87**(10): p. 103103.
6. Martin, Y. and H.K. Wickramasinghe, *Magnetic Imaging by Force Microscopy with 1000-Å Resolution*. Applied Physics Letters, 1987. **50**(20): p. 1455-1457.
7. Kulawik, M., et al., *A double lamellae dropoff etching procedure for tungsten tips attached to tuning fork atomic force microscopy/scanning tunneling microscopy sensors*. Review of Scientific Instruments, 2003. **74**(2): p. 1027-1030.
8. Akiyama, T., U. Staufer, and N.F. de Rooij, *Self-sensing and self-actuating probe based on quartz tuning fork combined with microfabricated cantilever for dynamic mode atomic force microscopy*. Applied Surface Science, 2003. **210**(1-2): p. 18-21.
9. Akiyama, T., et al., *Symmetrically arranged quartz tuning fork with soft cantilever for intermittent contact mode atomic force microscopy*. Review of Scientific Instruments, 2003. **74**(1): p. 112-117.
10. Seo, Y., P. Cadden-Zimansky, and V. Chandrasekhar, *Low-temperature scanning force microscopy using a tuning fork transducer*. Journal of the Korean Physical Society, 2007. **50**(2): p. 378-383.

11. Gunther, P., U. Fischer, and K. Dransfeld, *Scanning near-Field Acoustic Microscopy*. Applied Physics B-Photophysics and Laser Chemistry, 1989. **48**(1): p. 89-92.
12. Karrai, K. and R.D. Grober, *Piezo-electric tuning fork tip-sample distance control for near field optical microscopes*. Ultramicroscopy, 1995. **61**(1-4): p. 197-205.
13. Karrai, K. and I. Tiemann, *Interfacial shear force microscopy*. Physical Review B, 2000. **62**(19): p. 13174-13181.
14. Karrai, K., *Lecture notes on shear and friction force detection with quartz tuning forks*, in *Ecole Thématique du CNRS*. 2000: La Londe les Moures, France.
15. Rychen, J., et al., *A low-temperature dynamic mode scanning force microscope operating in high magnetic fields*. Review of Scientific Instruments, 1999. **70**(6): p. 2765-2768.
16. Rychen, J., et al., *Force-distance studies with piezoelectric tuning forks below 4.2 K*. Applied Surface Science, 2000. **157**(4): p. 290-294.
17. Edwards, H., et al., *Fast, high-resolution atomic force microscopy using a quartz tuning fork as actuator and sensor*. Journal of Applied Physics, 1997. **82**(3): p. 980-984.
18. Ihn, T.V., T. Baumgartner, A. Studerus, P. Ensslin, K., *Operating a phase-locked loop controlling a high-Q tuning fork sensor for scanning force microscopy*. 2001, Arxiv.
19. Vorburger, P., *Construction of a scanning force microscope and force-distance measurements on gold and graphite surfaces*, in *Laboratory of solid state physics*. 1999, Zurich: Zurich. p. 72.
20. Giessibl, F.J., *High-speed force sensor for force microscopy and profilometry utilizing a quartz tuning fork* (vol 73, pg 3956, 1998). Applied Physics Letters, 1999. **74**(26): p. 4070-4070.
21. Giessibl, F.J., *Atomic resolution on Si(111)-(7x7) by noncontact atomic force microscopy with a force sensor based on a quartz tuning fork*. Applied Physics Letters, 2000. **76**(11): p. 1470-1472.
22. Giessibl, E.J., et al., *Imaging of atomic orbitals with the atomic force microscope experiments and simulations*. Annalen der Physik|Annalen der Physik, 2001. **10**(11-12): p. 887-910.

23. Seo, Y., H. Choe, and W. Jhe, *Atomic-resolution noncontact atomic force microscopy in air*. Applied Physics Letters, 2003. **83**(9): p. 1860-1862.
24. Kikukawa, A., S. Hosaka, and R. Imura, *SILICON PN JUNCTION IMAGING AND CHARACTERIZATIONS USING SENSITIVITY ENHANCED KELVIN PROBE FORCE MICROSCOPY*. Applied Physics Letters, 1995. **66**(25): p. 3510-3512.
25. Kitamura, S. and M. Iwatsuki, *High-resolution imaging of contact potential difference with ultrahigh vacuum noncontact atomic force microscope*. Applied Physics Letters, 1998. **72**(24): p. 3154-3156.
26. Putman, C.A.J., et al., *Atomic force microscope featuring an intergrated optical microscope*. Ultramicroscopy, 1992. **42**: p. 1549-1552.
27. Putman, C.A.J., et al., *Atomic force microscope with integrated optical microscope for biological applications*. Review of Scientific Instruments, 1992. **63**(3): p. 1914-1917.
28. Hlady, V., M. Pierce, and A. Pungor, *Novel Method of Measuring Cantilever Deflection during an AFM Force Measurement*. Langmuir, 1996. **12**(22): p. 5244-5246.
29. Stuart, J.K. and V. Hlady, *Reflection Interference Contrast Microscopy Combined with Scanning Force Microscopy Verifies the Nature of Protein-Ligand Interaction Force Measurements*. Biophys. J., 1999. **76**(1): p. 500-508.
30. Nishida, S., Y. Funabashi, and A. Ikai, *Combination of AFM with an objective-type total internal reflection fluorescence microscope (TIRFM) for nanomanipulation of single cells*. Ultramicroscopy, 2002. **91**(1-4): p. 269-274.
31. Gorelik, J., et al., *Scanning surface confocal microscopy for simultaneous topographical and fluorescence imaging: Application to single virus-like particle entry into a cell*. Proceedings of the National Academy of Sciences of the United States of America, 2002. **99**(25): p. 16018-16023.
32. Yamada, T., et al., *High sensitivity detection of protein molecules picked up on a probe of atomic force microscope based on the fluorescence detection by a total internal reflection fluorescence microscope*. Febs Letters, 2004. **569**(1-3): p. 59-64.
33. Mathur, A.B., G.A. Truskey, and W.M. Reichert, *Total internal reflection microscopy and atomic force microscopy (TIRFM-AFM) to study stress*

- transduction mechanisms in endothelial cells*. Critical Reviews in Biomedical Engineering, 2000. **28**(1-2): p. 197-202.
34. Trache, A. and G.A. Meininger, *Atomic force-multi-optical imaging integrated microscope for monitoring molecular dynamics in live cells*. Journal of Biomedical Optics, 2005. **10**(6).
 35. Owen, R.J., et al., *An integrated instrumental setup for the combination of atomic force microscopy with optical spectroscopy*. Biopolymers, 2006. **82**(4): p. 410-414.
 36. Ebenstein, Y., T. Mokari, and U. Banin, *Quantum-dot-functionalized scanning probes for fluorescence-energy-transfer-based microscopy*. Journal of Physical Chemistry B, 2004. **108**(1): p. 93-99.
 37. Larcheri, S., et al., *X-ray excited optical luminescence detection by scanning near-field optical microscope: A new tool for nanoscience*. Review of Scientific Instruments, 2008. **79**(1).
 38. Park, S.I. and C.F. Quate, *Theories of the feedback and vibration isolation systems for the scanning tunneling microscope*. Review of Scientific Instruments, 1987. **58**(11): p. 2004-2009.
 39. Silveira, W.R. and J.A. Marohn, *A vertical inertial coarse approach for variable temperature scanned probe microscopy*. Review of Scientific Instruments, 2003. **74**(1): p. 267-269.
 40. Sarid, D., *Scanning force microscopy*. Oxford University Press. 1994.
 41. Rychen, J., *Combined low-temperature scanning probe microscopy and magneto-transport experiments for the local investigation of mesoscopic systems*, Swiss Federal Institute of Technology: Zurich.
 42. Melmed, A.J., *The art and science and other aspects of making sharp tips*. Journal of Vacuum Science & Technology B, 1991. **9**(2): p. 601-608.
 43. Nam, A.J., et al., *Benign making of sharp tips for STM and FIM - PT, IR, AU, PD, AND RH*. Journal of Vacuum Science & Technology B, 1995. **13**(4): p. 1556-1559.
 44. Zahl, P., et al., *The flexible and modern open source scanning probe microscopy software package GXSM*. Review of Scientific Instruments, 2003. **74**(3): p. 1222-1227.

45. Jersch, J., T. Maletzky, and H. Fuchs, *Interface circuits for quartz crystal sensors in scanning probe microscopy applications*. Review of Scientific Instruments, 2006. **77**.
46. Liu, J.Q., et al., *A simple and accurate method for calibrating the oscillation amplitude of tuning-fork based AFM sensors*. Ultramicroscopy, 2008. **109**(1): p. 81-84.
47. Qin, Y.X. and R. Reifenberger, *Calibrating a tuning fork for use as a scanning probe microscope force sensor*. Review of Scientific Instruments, 2007. **78**(6).
48. Langton, C. (2002). *Unlocking the phase locked loop*. Available: <http://www.complextoreal.com/chapters/pll.pdf>. Last accessed 27th January 2012
49. Mantzikas, C. and Langbein, W.W. *Time-correlated single photon counting module*. University of Cardiff, 2007.

4. Planned experiments

The ultimate objective for the combined scanning probe and optical microscope is to simultaneously measure the optical properties and charge of individual quantum dots. This would require a modification of the AFM setup to also perform electrostatic force microscopy (EFM).

As previously mentioned the AFM tip is sensitive to a range of forces. The electrostatic force is one such force which atomic force microscopes have been modified to detect. When there is a separation of charge between tip and sample a force will act between them that is proportional to the product of the two charges, and inversely proportional to the separation distance squared. This force will modify the oscillation of the AFM tip in a measurable way, allowing for the detection of charge difference between tip and sample. The electrostatic force is considered a long range force; one which can be detected several hundred nanometres from the sample surface. The name given to this form of SPM is electrostatic force microscopy.

In EFM an electrical connection is made to the tip. The tip is brought close to the sample surface and a voltage V is applied between the tip and sample to form a capacitor with a stored energy:

$$E = \frac{1}{2}CV^2 \quad (\text{Eq. 1})$$

where C is the capacitance. The force that acts between tip and sample is given by the derivative of this energy with respect to the separation distance z between the tip and sample:

$$F = \frac{1}{2} \frac{dC}{dz} V^2 \quad (\text{Eq. 2})$$

The resonance frequency of an oscillating tuning fork is given by:

$$\omega = \sqrt{\frac{k}{m}} \quad (\text{Eq. 3})$$

where m is the mass of the oscillator and k is the sum of the static spring constant of the tuning fork and the additional spring constant k_E due to the interaction between tip and sample. In the case of EFM this additional spring constant is given by the derivative of Eq. 2 with respect to the distance z :

$$k_E = \frac{dF}{dz} = \frac{1}{2} \frac{d^2C}{dz^2} V^2 \quad (\text{Eq. 4})$$

In EFM both an AC and DC voltage is applied between the tip and sample:

$$V = V_{DC} + V_{AC} \sin(\omega t) \quad (\text{Eq. 5})$$

And substitution of Eq. 5 into Eq. 4 yields three components of k_E :

$$k_{DC} = -\frac{d^2C}{dz^2} \left((V_{DC} - V_{CPD})^2 + \frac{1}{2} V_{AC}^2 \right) \quad (\text{Eq. 6})$$

$$k_{\omega} = -\frac{d^2C}{dz^2} (2(V_{DC} - V_{CPD}) V_{AC} \sin(\omega t)) \quad (\text{Eq. 7})$$

$$k_{2\omega} = -\frac{d^2C}{dz^2} \left(\frac{1}{2} V_{AC}^2 \cos(\omega t) \right) \quad (\text{Eq. 8})$$

where V_{CPD} is the contact potential difference (CPD). The CPD arises due to the difference in Fermi levels of the tip and sample materials; when these materials are brought into close proximity there is a redistribution of charge to align the Fermi levels of the tip and sample materials.

It can be seen from these equations that the resonance frequency of the tuning fork will be changed in three ways; first by a static value proportional to the DC voltage between the tip and sample. Second the oscillation frequency will vary at the frequency of the externally applied AC voltage ω , and thirdly it will vary at a frequency twice that of the applied AC voltage; 2ω .

The component k_{ω} has a magnitude proportional to the potential difference between the tip and the sample, at the frequency of the applied AC voltage. A lock in amplifier is typically employed to accurately measure this signal and use it to determine the local electronic properties of the sample. A variation of this technique

is Kelvin probe microscopy (KPM), where the external DC voltage is manipulated with a feedback loop in order to reduce the k_{ω} component to zero. The DC voltage that must be applied to fulfil this condition is a direct measure of the CPD between the tip and sample.

Initially EFM and Kelvin probe microscopy were performed by a 2-pass technique, this remains the most common method for these techniques; first the topography of the sample is measured, then the tip is withdrawn and is moved over the sample at a fixed height using the topographical data, during this second pass electronic measurements are performed. Subsequently techniques have been realised to allow for simultaneous AFM and KPM measurements to be made [1, 2].

Krauss et al [3] use EFM to measure the charge on single quantum dots with ambient light and laser excitation. They also summarise a technique for determination of the charge on a quantum dot by measurement of the frequency shift due to electrostatic forces. CdSe/CdS quantum dots were used for these experiments. Krauss found that 50% of dots stored in organic solvent and illuminated by ambient light developed a single positive charge after several weeks. Less than 1% of these dots demonstrated a blinking behaviour in their charge. The same dots under laser excitation (442nm, 20W/cm²) developed an additional positive charge during excitation periods of several minutes.

The most detailed study of QDs by EFM has been performed by Cherniavskaya *et al* [4-6]. They observed charging effects of CdSe/CdS QDs on both n-doped and p-doped silicon with different oxide layer thickness'. They also observe a positive charging effect on the quantum dots whilst under illumination and attribute this to electrons tunnelling from the dot to the silicon through the oxide layer. They suggest that due to band bending there is an accumulation of electrons (holes) at the silicon/oxide interface for p-type (n-type) silicon. As a result dots on P-type silicon were shown to exhibit less charging and to have quicker recombination times than on the n-type substrate. They found that the effects of oxide thickness were negligible. Cherniavskaya et al provide EFM data clearly showing the charge of QDs changing between not two, but a set of discrete states with time. The charge intermittency was shown on both n-type and p-type silicon over a period of 800 minutes.

It was exactly for these types of experiment that our microscope was developed; so that charge intermittency data could be obtained at exactly the same time as the optical data for the same quantum dot. Whilst the optical data largely alternates between two discrete levels, the EFM experiments of Cherniavskaya et al suggest that a single quantum dot can develop a charge of 4-5 electrons. How do these multiple charges affect the optical intermittency of the dot?

A second experiment that we hope to perform is to apply a potential difference between the tip and a conductive substrate on which the QDs are spun cast, and to measure the fluorescence of these dots with varying electric field strengths.

Preliminary EFM experiments have been performed using the microscope. In these experiments one of two methods were used to produce conductive tips suitable for EFM. Either a cantilever tip was used that had a layer of gold evaporated onto the tip side, or Pt/Ir wire tips were used after electrochemical etching. Conductive epoxy was used to attach these tips to one set of tuning fork electrodes, through this electrode a potential difference could be applied between tip and sample. With this arrangement the microscope is capable of performing the second set of intended experiments outlined above.

For charge measurements on single quantum dots the system would have to be calibrated for EFM. This calibration would allow the charge on a sample to be determined from the frequency shift detected by the tuning fork sensor.

4.1. References

1. Kikukawa, A., S. Hosaka, and R. Imura, *SILICON PN JUNCTION IMAGING AND CHARACTERIZATIONS USING SENSITIVITY ENHANCED KELVIN PROBE FORCE MICROSCOPY*. Applied Physics Letters, 1995. **66**(25): p. 3510-3512.
2. Kitamura, S. and M. Iwatsuki, *High-resolution imaging of contact potential difference with ultrahigh vacuum noncontact atomic force microscope*. Applied Physics Letters, 1998. **72**(24): p. 3154-3156.
3. Krauss, T.D., S. O'Brien, and L.E. Brus, *Charge and photoionization properties of single semiconductor nanocrystals*. Journal of Physical Chemistry B, 2001. **105**(9): p. 1725-1733.
4. Cherniavskaya, O., L.W. Chen, and L. Brus, *Imaging the photoionization of individual CdSe/CdS core-shell nanocrystals on n- and p-type silicon substrates with thin oxides*. Journal of Physical Chemistry B, 2004. **108**(16): p. 4946-4961.
5. Cherniavskaya, O., et al., *Photoionization of individual CdSe/CdS core/shell nanocrystals on silicon with 2-nm oxide depends on surface band bending*. Nano Letters, 2003. **3**(4): p. 497-501.
6. Cherniavskaya, O., et al., *Quantitative noncontact electrostatic force Imaging of nanocrystal polarizability*. Journal of Physical Chemistry B, 2003. **107**(7): p. 1525-1531.

5. Conclusion

The aim of this project was to develop a microscope capable of simultaneous scanning probe and optical microscopy techniques under high vacuum. This homebuilt system required the design and construction of numerous parts with the scanning probe part relying on only a small number of commercially available components, most notably the Attocube scanning piezo and coarse piezoelectric stack, and the Signal Ranger DSP. Developing the scanning probe part of this microscope has been the most challenging aspect of the project.

The quartz tuning fork based sensors are ideal for homebuilt systems, where a laser based phase sensitive detector would be difficult to construct and employ. During this project two different techniques have been developed for mounting sharp tips on these sensors. The first – electrochemical etching of Pt/Ir wire tips is an innovation of that described by Vorburger et al [1]. For the second method silicon cantilevers have been used. These cantilever tips have been employed by other groups in one of two ways. In the first, the entire cantilever and wafer has been mounted on the tuning fork leading to a significant detriment of the tuning fork quality factor. The second method is to either produce cantilevers, or remove the cantilever section from the silicon wafers they are mounted on when purchased commercially. These cantilevers are then mounted on the tuning fork, a method which is challenging due to their size and fragility, and the time this process requires.

In our method commercially available silicon cantilevers are used, but the excess silicon wafer is removed by careful cutting with a scalpel. Whilst our method for mounting cantilever tips does not achieve the quality factor of that achieved in the latter method outlined above, it is considerably quicker. The entire process, starting with a hermetically sealed tuning fork and ending with a tip mounted tuning fork takes only approximately 20 minutes. The quality factor of these sensors is about 1×10^4 under high vacuum, an order of magnitude greater than that we have been able to obtain by mounting the entire cantilever and wafer on the tuning fork.

Several homebuilt positioning stages have been developed so that the optical and scanning probe sections of the microscope can be positioned on the same region of the sample. One of these is based on a design by Silveira *et al* [2]. In this design the inertia generated by a small (9mm length) and relatively cheap piezo stack is utilized to slide two outer plates back or forth over a central mounted plate in a slip/stick fashion. Our version of this design is larger than the original of Silveira *et al*, capable of moving up to 6mm. To this is mounted our scanning piezo, tuning fork mount and sensor. This homebuilt positioning device allows us to approach or withdraw the tuning fork tip by increments as small as 100nm.

A second set of positioning stages has been developed to control the horizontal and vertical positioning of the AFM tip relative to the sample. These positioners are controlled by turning fine threaded screws, and are spring loaded so that on unscrewing the screws the positioners return to their original position. These coarse positioning devices are used only to locate the tuning fork tip over the region of the sample the optical part of the microscope is focused on. This process takes only a few minutes, and once achieved the positioning devices can be locked in place using two sets of mounting screws. This simple system could easily be adjusted to provide a larger travel distance than the 10mm ours allows for (both vertically and horizontally).

The resolution of the scanning probe microscope is ultimately limited not by the phase locked loop or associated electronics, but by vibrational noise. The system is mounted on a set of springs designed to have the lowest resonant frequency possible for the space inside the vacuum chamber. Also, a magnetic damping system is employed to further reduce the kinetic energy of the microscope. Despite both of these vibration isolation systems and the vacuum chamber being fixed to an air bench, the system still has an extreme sensitivity to vibrations. This noise limits the resolution to about 1nm, small enough so that quantum dots or nanowires are visible, but enough to limit the ability of the microscope to make electronic measurements on these systems.

The scanning probe part of the microscope can be adapted to perform either electrostatic force microscopy or Kelvin probe microscopy. For these measurements

a potential difference is required between tip and sample. Electrochemically etched Pt/Ir tips can be electrically connected to one set of tuning fork electrodes by using conductive epoxy. Cantilever tips can be made conductive by evaporation of a thin layer of platinum and gold (typically about 10nm in thickness). A challenge that must be overcome in achieving Kelvin probe or electrostatic force microscopy is in the sample preparation. For optical microscopy techniques the sample must be transparent, for Kelvin probe/EFM techniques the sample must be conductive. Achieving both of these criteria has proven difficult.

By evaporating thin layers of chromium (several nm) onto a glass cover slip, a conductive optically transparent substrate is achieved. However, the chromium forms a granular structure on the surface of the glass. These granules are spherical and have a diameter of a few nanometres, almost identical to that of quantum dots. Literature suggests that this granular surface can be flattened by annealing, though our own experiments have not been successful in changing the granular nature of the surface. This is a problem that is unique to experiments where combined EFM/Kelvin probe and optical measurements are to be performed. This issue may be addressed in the future by using doped (conductive) nanodiamond substrates.

In summary the foundations for a homebuilt scanning probe and optical microscope have been laid, but there are several issues that must be addressed in order for this system to reach its potential as a tool for performing research. With these problems resolved the microscope should be capable of its intended purpose; first to measure the charge of optically excited quantum dots undergoing photoluminescence intermittency whilst simultaneously monitoring the dots optical output, and secondly to determine the effect of a quantum dots electrical environment on its luminescence. Recently commercial systems have become available with the ability to perform these combined microscopy techniques, but our system has been constructed for a small fraction of the commercial alternatives cost.

1. Vorburger, P., *Construction of a scanning force microscope and force-distance measurements on gold and graphite surfaces*, in *Laboratory of solid state physics*. 1999, Zurich: Zurich. p. 72.
2. Silveira, W.R. and J.A. Marohn, *A vertical inertial coarse approach for variable temperature scanned probe microscopy*. *Review of Scientific Instruments*, 2003. **74**(1): p. 267-269.